



**Politecnico di Milano**

---

SCHOOL OF CIVIL, ENVIRONMENTAL AND LAND  
MANAGEMENT ENGINEERING

Master of Science in Civil Engineering for Risk Mitigation

# Analysis of the erosional processes following the September 2022 flood in the Misa basin

Supervisor:

Prof. Laura Longoni

Candidate:

Riccardo Mattavelli

ID: 997061

Co-Supervisor:

Dott.ssa Monica Corti

---

Academic Year 2022-2023

## **Abstract**

This study aims to investigate the complex phenomenon of erosion as a consequence of a flood event. The chosen case study is that of the Misa River basin in the Marche region, at whose outlet rises the city of Senigallia (AN) following the exceptional flood event of September 2022. The erosion phenomenon represents a critical geomorphic process, which produces the modification at the morphological level of the basin. In addition to having a strong environmental impact, this process also has strong implications on the level of human settlements, as many civil works are allocated near river courses and bank, such as roads, buildings, or bridges. The alterations can produce damage to structures. This thesis investigates the main causes of erosion, starting from an analysis of the characteristics of the riverbed by analyzing the solid transport due to the water current, which transfers sediments up to the closure section. It then moves on to an examination of the September 2022 flood event, which revealed a profound link to climate change since the storm examined was classified as V-shaped that usually characterizes tropical storms. In order to understand the reasons of this phenomenon, the rise of sea temperatures and the peculiar morphological setting of a costal basin enclosed by the Apennine Mountain range are considered. The analysis of these data enabled the study of the entire basin using the physically-based SWAT model. The software, which is supported by a QGIS interface, allows any basin to be hydrogeologically analyzed. Through it, it is possible to produce maps showing daily, monthly and annual trends of the main characteristics of the river network, such as mean and peak flow and eroded volumes, starting with total flow and declining into bank and bed erosion. For bank erosion, bank width shortening in meters was also evaluated. In conclusion, this thesis helps to demonstrate how SWAT can prove to be a very useful and versatile tool for the purpose of estimating and analyzing the relationship between inflows and outflows in any basin following a flood event. The greatest potential could also be revealed in the area of forecasting future scenarios, either through the use of hypothetical rainfall data or as a result of changes at the geologic level of the basin.

## **Riassunto**

Questo studio si propone di indagare la complessità del fenomeno dell'erosione come conseguenza di un evento alluvionale. Il caso studio scelto è quello del bacino del fiume Misa nella regione Marche, alla cui foce sorge la città di Senigallia (AN), a seguito dell'eccezionale evento alluvionale del settembre 2022. Il fenomeno erosivo è classificato come processo geomorfico, ovvero che produce la modifica a livello morfologico del bacino. Oltre ad avere un forte impatto ambientale, questo processo ha anche forti implicazioni a livello degli insediamenti umani, in quanto molte opere civili sorgono in prossimità dei corsi e delle sponde fluviali, come strade, edifici o ponti. Tali alterazioni possono produrre danni alle strutture. Questa tesi indaga inoltre le principali cause dell'erosione, partendo dall'analisi delle caratteristiche dell'alveo, analizzando il trasporto solido dovuto alla corrente d'acqua, che trasporta i sedimenti fino alla sezione di chiusura. Si passa poi all'esame dell'evento alluvionale del settembre 2022, che ha rivelato un profondo legame con i cambiamenti climatici in quanto la tempesta esaminata è stata classificata come V-shaped che solitamente caratterizza le fasce tropicali. Per comprendere le ragioni di questo fenomeno si considerano l'innalzamento della temperatura del mare e il particolare contesto morfologico, che è un bacino costale racchiuso posteriormente dalla catena montuosa appenninica. L'analisi di tutti questi dati ha permesso di studiare l'intero bacino utilizzando il modello fisico SWAT. Il software, supportato da un'interfaccia QGIS, consente di analizzare idrogeologicamente qualunque bacino. Con questo è possibile produrre mappe che mostrano le tendenze giornaliere, mensili e annuali delle principali caratteristiche della rete fluviale, quali portata media e di picco e i volumi erosi, a partire dalla portata totale fino all'erosione delle sponde e del letto. Per l'erosione delle sponde è stato valutato anche l'accorciamento della larghezza delle sponde in metri. In conclusione, questa tesi contribuisce a dimostrare come SWAT possa rivelarsi uno strumento molto utile e versatile per stimare e analizzare la relazione tra afflussi e deflussi in qualsiasi bacino a seguito di un evento di piena. Il potenziale maggiore potrebbe rivelarsi anche nell'ambito della previsione di scenari futuri, sia attraverso l'utilizzo di dati pluviometrici ipotetici, sia come risultato di cambiamenti a livello geologico del bacino.

## Table of contents

1. Introduction .....	6
2. State of the art.....	8
2.1 Sediment transport .....	8
2.1.1 Bed load.....	8
2.1.2 Suspended load.....	13
2.2 Riverbed morphological modeling .....	16
2.3 Erosion processes.....	19
2.3.1 Bank erosion.....	22
2.3.2 Shallow landslide .....	24
2.3.3 Debris Flows .....	26
2.4 Erosion evaluation .....	28
2.4.1 Field monitoring.....	28
2.4.2 Semiempirical models: USLE, RUSLE, MUSLE and Gavrilovic.....	33
2.4.3 Physically-based model: SWAT .....	41
2.4.4 Stability Analysis: SLIP and Takahashi models.....	45
3. Case study: Misa Basin .....	49
3.1 Hazard and risk mitigation in Marche region .....	52
4. Analysis of the flood event of September 2022.....	56
4.1. The flood.....	56
4.2 Rainfall analysis and comparisons.....	64
4.3 Discharge analysis and comparisons .....	70
5. SWAT analysis.....	78
5.1 Simulation setup .....	78
5.2 Preliminary analysis: land use maps sensitivity .....	89
5.3 Results.....	94
5.3.1 Hydraulic results (2022, 2014, 2017).....	95
5.3.2 Geologic results (2022, 2014, 2017).....	98
6. Discussions .....	107
6.1 Water discharge.....	107
6.2 Sediment erosion and transport.....	119
6.3 Climate change .....	127
7. Conclusions .....	135



8. Bibliography .....	137
9. Appendix.....	149

# 1. Introduction

The transport of sediments due to the action of water is defined as solid transport and occurs wherever there is water and loose material available. For these reasons, mountain basins are the perfect place for this to happen as, very often, they have abundant surface deposits and are characterized by thunderstorm rains. Furthermore, they are also characterized by steep slopes, which facilitate the movement of debris. The sediments are then transported from the internal areas of the basin to the outlet. This process can potentially cause problems for human settlements which are usually concentrated at the bottom of the valley, where the outlet is located. By settling, the sediments can lead to the raising of the riverbed in correspondence with dams or artificial basins, or wherever the slope starts to reduce (1). Other problems related to sedimentation involve the biological sphere, in particular with the eutrophication of basins and the consequent reduction in the levels of available oxygen in water. The process could lead to the suffering of the river fauna (2). The focus of this analysis will not touch on these topics but will concentrate on the transport of material following storms and floods. During intense storm events, the production of sediments increases exponentially, due to the increase in the flow rate of the water courses and due to the increase in the instability of the slopes, which pour sediment into the water courses through landslides and flows (3). The theoretical section of the analysis is organized into the parts that constitute the various erosional components. It begins with fluvial erosion, by considering bed load and suspended load, and then shifts the focus to slopes and riverbanks. Here the interactions between precipitation, runoff water and soil will be described. Finally, both direct and indirect methods will be discussed. They can be used to yield an estimation of the volumes of eroded material. The storm event of 15<sup>th</sup> and 16<sup>th</sup> September 2022 that hit the Marche region will be the area of analysis of this phenomenon. In particular, this thesis focuses on the Misa River basin, which extends south-west of the province of Ancona. The event had a wide resonance, as there were 13 fatalities and 50 injured people with economic losses of around 2 billion of euros. During this event, the erosive component played a key role as the exceptional rainfall caused huge amounts of sediment to be transported from inland areas to the outlet. The objective of the analysis is therefore to give an estimate of the volumes and the related components, particularly bank and bed erosion. In addition to analyzing the situation from a hydrogeological point of view, it is also essential to study the causes that led to the

formation of a storm system called V-shaped storm, characteristic of tropical areas, now increasingly present also on the Italian territory. This work therefore analyzes the data on the climate and sea temperature in order to establish the trend of sea temperatures from 1950 to the present days. An upward trend is indeed associated with increased development of these storms. The basin analysis will focus on modeling through defined physically based models. This means that the complexity of the inflow-outflow transformation process is represented through the resolution of physical equations, which describe the relationships between the input variables and the hydraulic and hydrological processes. The model used is SWAT (Soil & Water Assessment Tool), which allows the modeling of hydrogeological phenomena at the level of the stream network. The model requires an accurate description of the geological and hydraulic characteristics of the basin, which are provided in raster format through a GIS interface. Different results can be plotted as output, in particular the components of runoff and sedimentation values, which are evaluated at the river channel level (4). The hydraulic part will be validated through flow values calculated from water height measurements obtained in situ, while the geologic part will serve as a starting point to provide an estimate of volumes moved and to allow comparisons with both volumes from past events and annual average values.

## **2. State of the art**

### **2.1 Sediment transport**

In order to understand how debris is transported to the outlet, it is necessary to analyze its interaction with the water flowing in the drainage network. The process of sediment transport along a river course is divided into two main components: bed load and suspended load. To understand the triggering of the phenomenon it is necessary to define a threshold value (5) for which the flow acquires the ability to transport the sediment. The definition of critical condition is therefore necessary. Once this is determined, it is then possible to estimate the amount of material transported and deposited over time (6).

#### **2.1.1 Bed load**

In order to determine the motion for which the transport is triggered, it proceeds with the isolation of a single particle, and they will be analyzed the forces applied to it (7). For simplicity, it is assumed that every particle is perfectly spherical. There are two possible movements: sliding and rolling. By considering the case of rolling, the moment necessary for the particle to start moving must be guaranteed. The analyzed particle rests on a background of equally spherical particles (Figure 1). The moment to be analyzed is therefore the one occurring around the contact point P. The forces applied to the particle are those due to the flow, which includes the drag one (Eq. 2), parallel to the flow itself, and the lift force (Eq. 3) due to the Archimedean thrust, which is directed towards the high. These forces must overcome the action due to the particle's own weight (Eq. 4) which is directed downwards.

$$D * b + L * a = G * a \text{ (Eq. 1)}$$

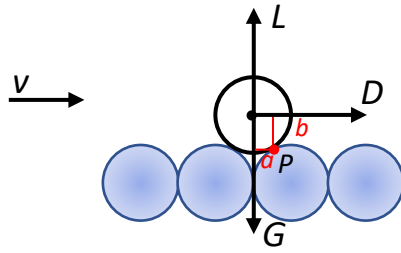


Figure 1: Spherical model for bed load.

$$D = 0.5\rho v^2 C_D \frac{\pi d_s^2}{4} \text{ (Eq. 2)}$$

$$L = 0.5\rho v^2 C_L \frac{\pi d_s^2}{4} \text{ (Eq. 3)}$$

$$G = \frac{\pi d_s^3}{6} (\rho_s - \rho) g \text{ (Eq. 4)}$$



$$\frac{v^2}{g(s-1)d_s} = \frac{4}{3} \left( C_D \frac{b}{a} + C_L \right) \text{ (Eq. 5)}$$

Where:

$D = \text{Drag force}$

$L = \text{Lift force}$

$G = \text{Weight force}$

$C_D = \text{Drag coefficient}$

$C_L = \text{Lift coefficient}$

The limit equilibrium (Eq. 5) is therefore imposed by establishing the equilibrium of the moments around P (Eq.1). In determining the forces, some problems are encountered, starting from the flow velocity itself, which does not have a constant value over the section, but has a certain distribution. Furthermore, it is necessary to determine the drag and lift coefficients, which depend on the Reynolds number. It can therefore be deduced that this formulation is difficult to implement (8).

The idea is, therefore, to apply an upscaling approach to the problem by trying to link the previous relation to the frictional velocity  $V^*$  (Eq. 6), which is connected to the friction  $\tau$  through the following formulation:

$$V^* = \sqrt{\frac{\tau}{\rho}}, \text{ (Eq. 6) with } \tau = \rho g R_H S_f$$

It governs the speed profile (Figure 2) and can be managed as a representative factor of the whole profile. The velocity along the profile and the shear velocity are related by the law of resistance (Eq. 7):

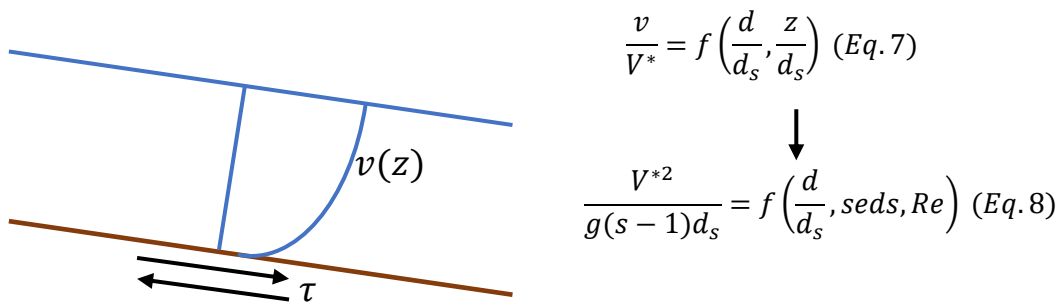


Figure 2: Velocity profile of water.

The relationship obtained, being a generic equation (Eq. 8), must refer to the experimental analysis.

Then, it is defined the number of Shields (Eq. 9), whose physical meaning refers to the relationship between the actions that trigger the movement and those that slow down the sediments. It is therefore a matter of a dimensionless effort on the resisting force.

$$\tau^* = \frac{V^{*2}}{\rho(s-1)d_s} \text{ (Eq. 9)}$$

The critical value of this parameter can be obtained from the Shields abacus. It imposes the condition of incipient motion. Values of 0.1 are higher than the critical threshold value (for high Reynolds numbers). Values between 0.03 and 0.06 are in a critical range, and normally an average value of 0.045 is chosen. There is no transport for values of 0.01. The critical value is compared with the previously obtained value of  $\tau^*$ . If this is above the critical threshold value, the conditions are favorable for sediment transport (9).

After verifying this, it is possible to evaluate the transport capacity,  $q_s$ , which is defined as the solid discharge per unit of width. There are many formulas to evaluate the latter and they are all an empirical nature, in fact they have calibrated parameters so that they are effective ranges of validity. One of the most famous is that of Meyer-Peter-Müller (Eq. 10):

$$q_s = \frac{\Phi}{\sqrt{g(s-1)d_s^2}}, \text{ where } \Phi = 8(\tau^* - \tau_c^*)^{\frac{3}{2}} \text{ (Eq. 10)}$$

The Meyer-Peter-Müller formula is valid in a range of value included in  $1.25 < s < 4.2$ , where  $s$  is the relative density. (10).

For the Misa River, as described further on, bed load has little relevance because the grain sizes fractions present near the delta of the river are fine, in particular there are in almost identical proportions of silt and clay up to a depth of 1.80 meters; so, the component of suspended load is more relevant. The only area where coarser sizes are present is next to the delta, where the river is in direct contact with the Adriatic Sea. In fact, due to storm surges, the composition typically includes approximately 70% sand and 30% gravel. However, these values are limited to the last meters of the river, thus negligible in terms of total sediment transport (11). The initial part of the course flows through the Apennine section, where slope gradients reach values of  $45^\circ$ . Grain sizes in this section vary and are characterized in particular by recent alluvial deposits, as shown by the map in Figure 17, taken from the geological map of Italy (CARG project), provided by the ISPRA Ambiente website. The Meyer-Peter-Müller formula is well-suited for riverbeds varying but moderate grain sizes, typically between 0.4-29 mm and slopes of less than 2% (approximately  $1.15^\circ$ ). However, the considered riverbeds have much steeper slopes,

rendering the formula unsuitable. The evolution of the formula (Eq. 11) was carried out by Smart and Jaeggi (1983) (12), which more accurately estimates the bed load in the case of mountainous riverbeds with slopes reaching 21%. The dimensionless formula is as follows:

$$\Phi = 4 \left( \frac{d_{90}}{d_{30}} \right)^{0.2} i^{0.6} \theta^{0.5} (\theta - \theta_{cr}) \left( \frac{v}{V^*} \right) \quad (Eq. 11)$$

Where:

$i$  = slope

$\theta$  = dimensionless tangential stress

$v$  = velocity of the flow

$V^*$  = frictional velocity



### 2.1.2 Suspended load

The process occurs in the water column due to convection and advective diffusion. Sediments are kept in motion by the vertical buoyancy components (buoyancy forces) of the flow. Suspended particles can be categorized according to their grain size into cohesive (with diameter less than 0.062 mm) and non-cohesive (with diameter greater than 0.062 mm). The non-cohesive particles are usually derived from bed load and are transported at the flow's capacity, while the cohesive ones originate from wash load and are transported beneath the flow's capacity (13,14). In case of suspended load, the threshold is given by the ratio between the shear velocity  $V^*$  and the settling velocity. This relationship translates the physical phenomenon in which it is possible to have the competition between the flow that tends to raise the particles and that of sedimentation that causes them to sink. As in the case of the bed load, the shear velocity is used, which represents a value that is easier to determine. In this case, however, the estimation of the threshold value is more complex than that of the critical Shields value. The main reason is that distinguishing the truly suspended particles from those that saltate on the bottom is difficult to interpret. This leads to a considerable uncertainty in the determination of the threshold  $\frac{V^*}{w_o}$  value which ranges between 0.2 and 2. The transport capacity regarding the suspended load is evaluated through the following integral (Eq. 12), in which the transport of sediment below the threshold level ( $a$ ) is considered as bed load transport (15):

$$q_s = \int_a^d c_s v dz \quad (Eq. 12)$$

Where velocity  $v$  is derived from (Eq. 13) the flow velocity profile:

$$\frac{v}{V^*} = \frac{1}{K} \ln\left(\frac{z}{z_0}\right) \quad (Eq. 13)$$

Parameter  $c_s$  represents the sediment concentration, and it can be derived by integrating the vertical distribution of sediment concentration profile (Eq. 14), in the particular case of uniform and steady flow:

$$(1 - c)cw_{s,m} + \epsilon_s \frac{dc}{dz} = 0 \text{ (Eq. 14)}$$

The particles fall velocity is directly proportional to the diameter of the sediment. Three different formulations can be applied in three different ranges (Eqs. 15,16,17). The three equations are referred to the particular case of clear water:

$$w_s = \frac{1}{18} \frac{(s - 1)gd_s^2}{\nu}; d_s < 100\mu\text{m} \text{ (Eq. 15)}$$

$$w_s = 10 \frac{\nu}{d_s} \left\{ \left[ 1 + \frac{0.01(s - 1)gd_s^3}{\nu^2} \right]^{0.5} - 1 \right\}; 100\mu\text{m} < d_s \dots$$

$$< 1000\mu\text{m} \text{ (Zanke, (16)) (Eq. 16)}$$

$$w_s = 1.1[(s - 1)gd_s]^{0.5}; d_s > 1000\mu\text{m} \text{ (Eq. 17)}$$

The velocity of sediment in presence of clear water is greater than the one in presence of water with sediment. Indeed, the presence of surrounding particles leads to a reduction of the fall particle. The reduction of velocity in the case of normal flow conditions and in the range of 50-500  $\mu\text{m}$  is expressed by the (Eq. 18) Richardson-Zaki equation (17):

$$w_{s,m} = (1 - c)^4 w_s \text{ (Eq. 18)}$$

Furthermore, by considering a parabolic-constant  $\epsilon_s$  distribution, a  $w_{s,m}$  for particles in range of 50-500  $\mu\text{m}$  and small concentration  $c < 0.001$ , the expression will be:

$$\frac{c}{c_a} = \left[ \frac{a(d-z)}{z(d-a)} \right]^S ; \text{for } \frac{z}{d} < 0.5 \text{ (Eq. 19)}$$

$$\frac{c}{c_a} = \left[ \frac{a}{(d-a)} \right]^S e^{-4S(\frac{z}{d}-0.5)} ; \text{for } \frac{z}{d} \geq 0.5 \text{ (Eq. 20)}$$

In which:

$z_0 = \text{zero - velocity level}$

$K = \text{equivalent roughness height}$

$c_a = \text{reference concentration}$

$a = \text{reference level at which suspended load starts}$

$d = \text{depth}$

$z = \text{vertical coordinate}$

$w_{s,m} = f(ds) = \text{particle fall velocity in fluid - sediment mixture}$

$\epsilon_s = \text{sediment diffusion coefficient}$

$S = \text{suspension parameter}$

## 2.2 Riverbed morphological modeling

When modeling the behavior of a river, it is necessary to understand and analyze how the shape of the riverbed varies over time. In fact, the transport phenomena consequently lead to the introduction of the  $qs$  parameter, which describes the sediment transport rate. Rivers and streams that naturally flow in mountain basins, are characterized by erodible beds, therefore the estimation of their evolution is of fundamental importance in order to understand their future dynamics. In fact, whenever is occurring a removal of material from a section of riverbed, there is a corresponding deposition further downstream and vice versa. Furthermore, the deposition of large amounts of material in the riverbed causes its subsequent elevation. This produces the backwater effect by increasing the water surface elevation along the upstream section, thus generating retention areas that affect both morphology and flood routing. In fact, the presence of obstacles leads to a reduction in wave energy and the redirection of part of the current to the upstream (18). Taking two distinct riverbed sections (Figure 3), 4 different conditions can occur, in relation to how the sediment transport capacity  $qs$  is present in the two sections.

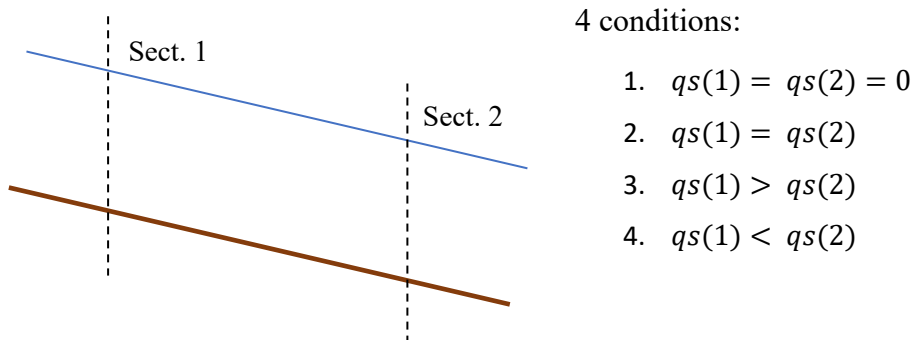


Figure 3: Riverbed sections in case of sediment discharge.

1. In the first condition the  $q_s$  parameter is null so nothing is in motion and the situation can be defined as static.
2. In the second condition there is always a condition of equilibrium but of a dynamic type. Sediment particles are continuously in motion and sediments are continuously replaced downstream due to upstream transport.
3. In the third condition there is no equilibrium situation, therefore the height of the bed will vary accordingly. In particular there is the arrival of a quantity of sediments from upstream which exceeds the downstream transport capacity. The sediments will accumulate in section 2 giving rise to a deposit situation with consequent thickening of the bed.
4. The fourth condition requires that the downstream transport capacity is higher than the upstream one. This situation induces erosion, which is why the bed will start to decrease in thickness.

Considering the third and fourth conditions, the variation in section 2 depends directly on the value of  $q_s$  and on the time to be considered  $\Delta T$  (19,20). Furthermore, when a certain volume of sediment is deposited, it will occupy a volume greater than that given by the sum of the individual grains. This happens because it is also necessary to take into account the porosity  $P_0$  of the medium (Eq. 21). This dimensionless parameter is defined as the ratio between the volume of the voids  $V_v$  and the total one  $V_t$ , which is the percentage of air over the entire volume:

$$P_0 = \frac{V_v}{V_t} \quad (Eq. 21)$$

Considering all this, the volume change equation  $\Delta W$  (Eq. 22) at section 2 turned out to be:

$$\Delta W(2) = \frac{(Q_s(1) - Q_s(2))\Delta T}{(1 - P_0)} \quad (Eq. 22)$$

Starting from this equation it is possible to pass to the differential form (Eq.23), through the derivation of the volume difference over time and the transport capacity over space:

$$\frac{\partial W}{\partial t} = -\frac{\partial Q_s}{\partial s} ds \frac{1}{1 - P_0} \quad (Eq. 23)$$

In order to eliminate the infinitesimal increment  $ds$  of the right-hand side, it passes from volume to section area  $A_s$ , obtaining the last equation (Exner equation (Eq. 24) (21,22)):

$$\frac{\partial A_s}{\partial t} = -\frac{\partial Q_s}{\partial s} \frac{1}{1 - P_0} \quad (Eq. 24)$$

After having obtained the last equation, it is possible to collect all the information in order to describe the process of morphological evolution through a system of partial differential equations.

$$\left\{ \begin{array}{l} \frac{\partial Q}{\partial s} + \frac{\partial A}{\partial t} = 0 \quad (Eq. 25) \\ \frac{\partial V}{\partial t} + V \frac{\partial V}{\partial s} + g \frac{\partial d}{\partial s} = g(S_0 - S_f) \quad (Eq. 26) \\ Q_s = f(\tau^*, \tau_c^*) \quad (Eq. 27) \\ \frac{\partial A_s}{\partial t} = -\frac{\partial Q_s}{\partial s} \frac{1}{1 - P_0} \quad (Eq. 28) \end{array} \right.$$

For this reason, the Saint Venant equations (Eqs. 25,26) (23) are needed, which describe the motion of water, in the particular case of unsteady flow in one dimension. The third equation (Eq. 27) gives the transport rate, which is based on the flow properties, described by the Shields number (9). The fourth equation is the Exner (21,22) equation (Eq. 28) derived earlier. The unknowns of this system are the water depth, the speed of the flow and the bed elevation.

## 2.3 Erosion processes

Shifting the focus of the analysis from the river bottom to the neighboring areas, such as banks and slopes, it is necessary to investigate the action of precipitation and runoff water on the soil. It consists of the surface materials that cover most of the landmass. This is generally composed of an inorganic fraction, which includes minerals and rocks, and an organic fraction. The different combinations of these two macro-components define the texture of soil. It is thus a highly heterogeneous compound, which is characterized by different grain sizes. The presence of grains of different sizes results in the presence of void zones, which define porosity. The aspects presented define the physical characteristics of the soil. Soils are not static materials, as their characteristics can change substantially as a result of exogenous events such as exposure to leaching processes operated by water or weathering that is produced by the combined action of climate, living organisms and plants. Soils can therefore undergo fracturing or chemical alterations that can induce major changes in their chemical and physical properties (24). The inorganic fraction of soil can be divided into 4 macro groups, which are characterized by different size of the grains  $d$  (25):

- Gravel, with  $d > 2\text{mm}$
- Sand, with  $2\text{mm} < d < 0.2\text{mm}$  for coarse sand and with  $0.2\text{mm} < d < 0.02\text{mm}$  for fine sand
- Silt, with  $0.02\text{mm} < d < 0.002\text{mm}$
- Clay, with  $d < 0.002\text{mm}$

The different combinations of gravel and sand define the aggregate fraction. Taken individually, the aggregates, turn out to be inconsistent because the cohesion of sand and gravel is zero. They can also be bounded by the presence of clay particles and by organic components, which in turn result from the decomposition of organic living matter. The alternation of materials within the matrix directly affects the circulation of air and water, which connects to the circulation of nutrients, which affects plant growth. In the case of soils strongly characterized by the presence of grain sizes tending toward sandy, their structure is poor, but drainage capacities are very good. As fine grain sizes increase, the structural strength of the matrix increases, but it loses drainage abilities. Nevertheless, clay-rich soils have very good retention properties, as they are characterized by high

absolute porosity. It differs from effective porosity, which normally characterizes higher grain sizes, in that the pores have no interconnections. Water therefore tends to be retained within the matrix without draining out (26). This characteristic property of clays and fine materials is called retention capacity. Knowledge of soil characteristics thus makes it possible to estimate in the first instance how the water will behave in contact with the soil itself. Soils with high fractions of coarse materials will be mechanically less resistant but have better drainage capacities, while in the case of soils rich in clay and fine materials, they will perform better but have poor drainage properties, which induce higher surface runoff (27). After having analyzed the transport processes from a hydraulic point of view and having described their modeling, it is natural to move to the macroscopic scale, thus going to analyze how sediments are produced and what they can cause when they are combined with extreme atmospheric phenomena. There are three steps that characterize erosion, and they are consequential. The first is splash erosion, which is produced by the impact of water droplets on the soil and, according to Morgan's studies (28), constitutes the process of particle detachment. Laboratory experiments conducted on different soils by Ryzak, M. (29) have shown how detaching soil particles can reach heights of up to 1.5 m and during storm events, particles can reach distances even of more than 5 meters, due to the wind actions. Another factor to consider for splash erosion is the impact of the droplets on the ground (29,30,31), which produces small craters and subsequent compaction of the soil itself. This leads to an increase in the bulk density and roughness. A consequence of this fact is the lower infiltration capacity, which is directly related to porosity, which is reduced due to impacts. This leads to failure to infiltrate precipitation and subsequent runoff. This leads to the second step, which is sheet erosion, which consists of the presence of a layer of water carrying the mobilized sediment down the slope (32,33). As a final step, the water and sediment can concentrate in more or less wide channels that are named rills in the case of small channels or gullies in the case of wide channels. The latter are normally generated through the joining of several rills (34). Accordingly, to the study of Liu et. al, the magnitude of soil loss increases up to 1.6 times when it turns into rill erosion (35). When rainfall is extremely violent and persistent, erosive phenomena are extremely amplified. They produce a very high erosion of both the banks and the bottom of the river in the area, primarily due to the action of the water on the sediments and to the destabilizing action produced by the raising of the



groundwater level and the presence of leaching waters. The three main mechanisms that could happen are:

- bank and bed erosion
- triggering of landslides
- debris flow



*Figure 4: a), b) Examples of bank erosion along Misa stream.*

Figures 4 a) and b) show the effects of the flood after the event of 15<sup>th</sup> September along the course of Misa River. In the pair of images, it is possible to observe the direct effect of the flood on the riverbed and on the banks. A very high removal of material from the entire riverbed, which was carried by the flood wave to the outlet, is immediately noticeable, and the effects on the vegetation are also observed. Trees and shrubs that were uprooted are deposited on the banks, which contributed to the increased transport of solids, which increased the destructive force of the flood.

### 2.3.1 Bank erosion

Bank erosion is a natural process that is always present in watercourses. It has little relevance and impact in the case of stable rivers not subjected to extreme weather conditions. Events such as storms that induce floods can trigger sudden changes in the equilibrium of the watercourse, in particular regarding water discharge. The flow rate of the river is directly related to the transport capacity, as it is related to the Shields number which in turn is directly proportional to the square of the shear velocity. This means that as the flow increases, the speed of the flow will also tend to increase (with the same section of the riverbed) and consequently also  $q_s$ . There are many mechanisms of bank erosion, but they can be divided into two macro-categories (36,37):

- bank scour
- mass failure.

Bank scour (Figures 5 a), b)) is the direct removal of bank material due to the physical action of water flow and the sediment it carries. This rate increases as the flow velocity increases. An unequivocal sign of this phenomenon is the presence of undermining and under excavation of the banks (38).

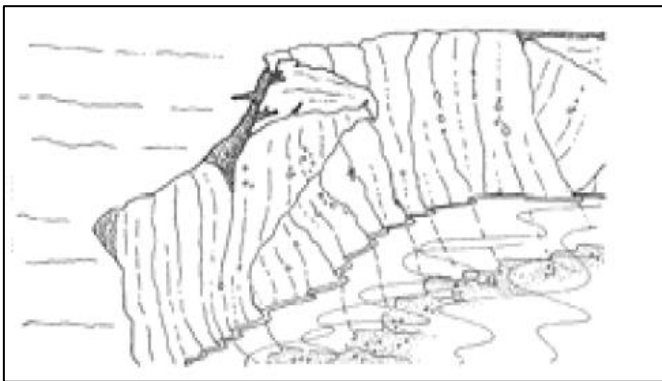


Figure 5: a) Bank scour (36); b) Bank scour along Misa stream.

The mass failure (Figures 9 a), b)), on the other hand, is the result of the sliding or overturning of portions of the bank inside the river due to its destabilizing action. Often the signs of the phenomenon are the presence of vertical or almost vertical banks and the presence of slumped bank materials. The fundamental discriminating factor when it comes to erosion is the land use of the embankments. The presence of vegetation and the cleanliness of the banks lead to greater stability and therefore a lower propensity to collapse. Another important factor to take into consideration is the presence of civil works such as roads, bridges or buildings, which can weigh on the embankments and lead to an increase in destabilizing actions (37).



*Figure 6: a) Mass failure (36); b) Mass failure along Misa stream.*



### 2.3.2 Shallow landslide

By shifting the attention from the banks to the slopes next to the main watercourse, the presence of shallow landslides can be often observed. They are geomorphic natural processes, and they add an important contribution in the transfer of sediments from the slopes to the watercourse and therefore to the valley floor. At the level of classification (Cruden and Varnes, 1996 (39)), they are part of the slides, in the particular case of reduced depth. They also represent a hazard to people and infrastructure within their area of influence. They occur on the slopes of mountain basins covered by layers of regolith and more or less compact sediments (40). The main trigger for this type of event is heavy rainfall (41), which can be very intense with short duration or long duration but with less intensity. The initiation of shallow landslide due to rainfall depends on the interactions between the physical properties of the slope materials with groundwater level. In fact, the saturation of deposit materials leads to an increase in their weight and therefore to an increase in the destabilizing forces acting on the slope (37).



*Figure 7: Shallow landslide in the municipality of Arcevia.*

Figure 7 shows an example of a shallow landslide that occurred in the municipality of Arcevia, which is located about 30 km from Senigallia. It denotes an extremely limited depth, which reaches a maximum of 40 cm which is outlined in the crown area. The inclination of the slope is extremely high, and the vegetation is sparse. The road also

provides a further element of disturbance on the slope due to the weight of the structure and the vibrations produced by the vehicles passing by. As a last feature, it also denotes outcropping rock, whose contact surface with the thin layer of soil constitutes a weak surface, as in that section the cohesion of the soil is reduced and the infiltration of the leaching water is compromised, favouring the rapid saturation of the layer of soil. The combination of these factors decisively favours the triggering of superficial landslides when the right triggering causes arise, in particular extreme rains and floods. When the value of the destabilizing forces exceeds that of the stabilizing forces the slope experiences failure. Normally the maximum depth to which the failure surface is set is 2 meters, it is planar and usually reflects the subdivision between the bedrock and the deposit layer. Furthermore, the slip surface can occur where the sediments are characterized by different geological or mechanical characteristics (3,43).

### 2.3.3 Debris Flows

The last phenomenon that induces erosion is debris flow. In general, flows are a type of landslide mechanism (Crudes and Varnes, 1996 (39)) which consists in the movement downstream, along slopes or riverbeds, of unconsolidated earthy or detrital materials saturated by water. The type of material and its concentration in the flow then determine the specific type of flow. They can be initiated by 3 mechanisms (44):

- transformations of deposit material caused by landslides,
- surface erosion induced by runoff waters,
- dam breaching.

This last phenomenon occurs due to particularly intense rains in which the saturation of the soil (Figure 8 a)) increases causing a worsening of the mechanical characteristics of the soil, as previously described for shallow landslides, causing failures on the slope. Part of the detached material accumulated in channels tends to form dams. With the accumulation of rain, the obstruction can lead to the creation of a temporary reservoir, which due to its own weight can lead to the collapse of the now saturated dam, transforming the debris into a flow. It can therefore be seen that it is fundamental that for a debris flow to occur, the presence of loose debris materials and a high-water availability are necessary.

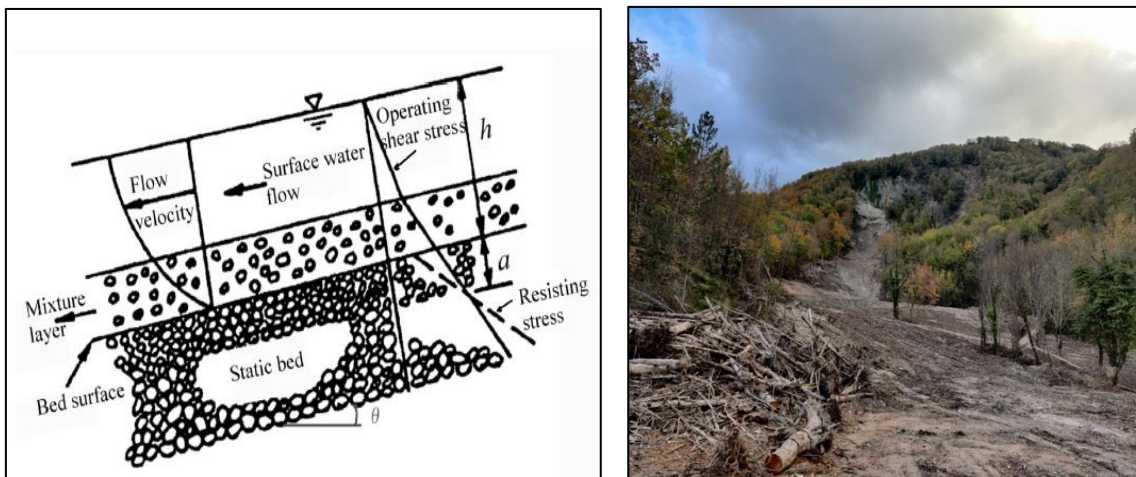


Figure 8: a) Distribution of the stress in a water-saturated soil (72); b) Complex landslide with a flow component in the municipality of Serra Sant'Abbondio (PU).

The flows can also be classified according to their debris content with respect to the liquid component.

- If the volume fraction of the solid is less than 20% it has clear water.
- if it is between 20% and 45% it has a hyper-concentrated flow.
- between 45% and 60% it has an effective debris flow.

Another subdivision for flows is also the percentage of particles finer than those of the sand within the flow (45):

- If the value is higher than 50% there is mudflow
- if lower than 50% there is debris flow.

## **2.4 Erosion evaluation**

### **2.4.1 Field monitoring**

The total amount of eroded material from bed and banks is channeled into the main course which, due to the high-water flow, drags the sediments which are produced from the phenomena described above, towards the bottom of the basin. When the slope of the basin tends to decrease, the energy of the current also tends to decrease. This involves the deposition of sediments starting with those with the greatest weight and ending with the finest sediments (8,10,15). Erosion processes, especially in mountain basins, are extremely complex to evaluate and therefore estimate. In fact, they are the product of the combination of a large number of factors that are often difficult to interpret or characteristics that are not considered due to the initial hypotheses imposed by the different models (46). For these reasons, the evaluation of processes through models only provides an estimate of the order of magnitude of the process. The approaches that are employed can be divided into 3 categories: direct monitoring, semi-empirical models and physically based models (47). These are also divided according to whether the assessment is conducted at the channel or basin scale. In the former case, erosion is due to the direct action of the river on bed and banks is assessed. In the second case, the assessment considers the routing of sediment produced throughout the basin on a seasonal or annual basis. Starting from the first category, the methods for the direct estimation of erosion processes which in turn are distinguished between methods that exploit remote sensing and methods that imply the direct installation of instrumentation on embankments and slopes. The three methods listed can assess banks erosion and they are the following:

- erosion pins,
- total station
- laser scanning.

Field experiences have shown that the errors, both relative and absolute, between the 3 methods are large. Furthermore, there is only a weak correlation between the results obtained with the total station and the laser scanner. For these reasons, the choice of method will depend on the site conditions, the objectives and the availability of resources (48).



Erosion pins are a simple and inexpensive monitoring system that is used to directly estimate soil deposition and erosion (49). Typically, the pins are installed in a grid pattern (Figure 9) where the installation depth is known.

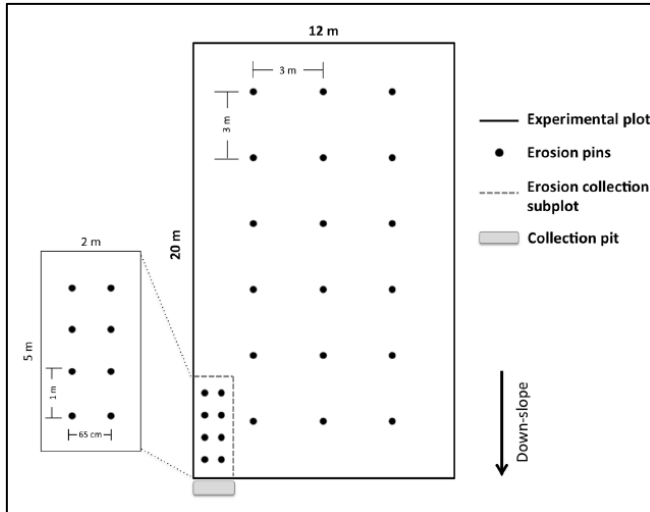


Figure 9: Erosion pins setup (49).

The objective is to evaluate the annual erosion rate, which is estimated (50, 51) starting from the average net variation in the height of the pin, which stands in the order of mm/yr, to then move on to the unit mass per area kg/ha\*yr via soil bulk density. Despite the successes obtained by various studies (e.g., Hancock (52)) and the possibility of obtaining results in an economic and intuitive way, many studies have also shown that the results obtained using erosion pins have little relationship with other methods and models (53). Furthermore, there is a further lack of correlation with the topographic features of the basin itself (52). Rueda et al. (54) have analyzed this situation also demonstrating the lack of relationship with semi-empirical models such as the USLE. For these reasons, the installation of erosion pins (Figure 10 a), b)) can be useful as an indicator of erosion or deposition rather than a tool for determining a numerical value (55). Furthermore, in the case of floods and extreme climatic events, the rapid degradation of the banks can easily lead to the detachment and loss of the pins (48).

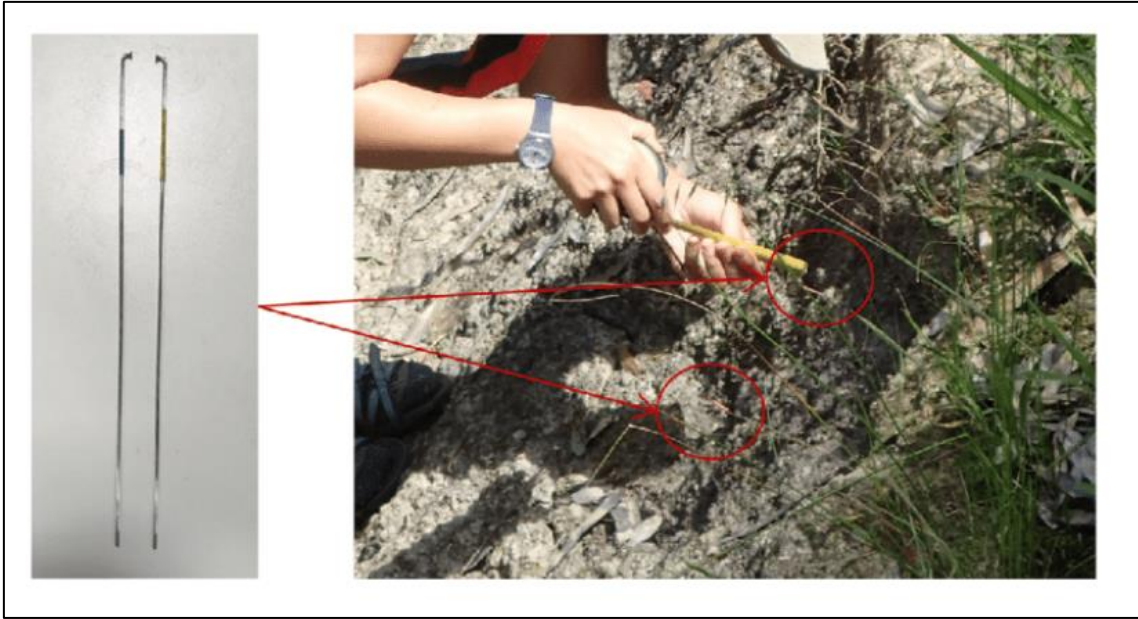


Figure 10: a) Erosion pins (56); b) Erosion pins installation (56).

The total station (Figure 11) is an electronic measuring instrument which allows the evaluation of horizontal angles, vertical angles, and distances. The total station approach is part of the remote sensing group of methods. In order to establish a defined and fixed reference system for the entire duration of the monitoring, it is necessary to establish control points in each analysis site. They are needed to orient the total station within the chosen projection system. They are normally points in areas characterized by the absence of external disturbances and are characterized by the presence of concrete or metal bases. The areas on which the total station will make the measurements are equipped with markers, which are often placed in correspondence with the erosion pins in order to already have a support. Measurements are made from one or more control points. In case it has been decided to move the total station, it is good to use a temporary control point in order to determine errors during the movement. Normally the same measurements are carried out after one year. Once the points are obtained, they are exported as a "comma separated value" file (CSV format) and imported into a GIS environment where they are processed to generate a 3D Tin file, which will simulate the shape of the bank. To evaluate any losses or increases in volume in the established period of time, a tool is used to evaluate the difference in surface area, then going to estimate what is the relative difference in volume per meter of riverbank. The estimated accuracy with a total station equipped with a prism is around 3mm. The criticalities of this method are the possibility of having a low density of points, which leads to approximate results, and the induction of possible bank disturbances due to the installation of the reflectors (48).



Figure 11: Total station with operator (48).

The laser scanner (Figure 12), which can be either terrestrial or aerial, uses Lidar technology in order to create high-resolution point clouds of a three-dimensional object (57,58), through the combination of laser-based measurements with precise orientations. The scans obtained are not georeferenced nor scaled. For this reason, before starting the scan it is useful to mount high reflectance target spheres on the markers. The markers will act as control points and will be measured by the total station and will serve as a reference to have points of overlap between the different scans obtained at different periods. As with the previous methods, the period between two measurements is usually one year. To evaluate and quantify the eroded or deposited material along a bank, several point clouds are produced at regular intervals. These are subsequently superimposed using specific software, such as Cloud Compare or GIS environment (59) and analyzed in order to evaluate the differences between the scans. These differences are converted into numerical volume values starting from a points cloud. The greatest potentials of this system are that it does not necessarily require fixed points or reflectors on the ground (in case it doesn't need a georeferentiation) and that it takes a few minutes to obtain a point cloud with a resolution of up to one centimeter (48).



*Figure 12: Laser scanner with operator (48).*

### 2.4.2 Semiempirical models: USLE, RUSLE, MUSLE and Gavrilovic

The methods listed below allow the definition of the quantity of sediment production at an annual or seasonal level, through the application of mathematical formulas which consider various factors that take into account how the routing of sediments can be developed in a basin. These parameters are related to rainfall, basin geometry, and soil types and conditions. The result is a single value referred to the catchment scale.

Soil erosion and its degradation, as already anticipated, is influenced by innumerable factors due both to natural action and due to human activities. Semiempirical models try to condense all these variables into parameters, which are then part of a final equation. One of the models used mostly in agricultural areas and to a lesser extent also in mountain basins is the USLE (60) (Universal Soil Loss Equation) model which was the pinnacle of soil erosion research collected in the United States. In 1965 it was published in the USDA Agricultural handbook 282 (61) and subsequently updated in its final form (Eq. 29) in 1978 (W.H. Wischmeier & D.D. Smith, 1978 (62)). The formula used in the model is as follows:

$$A = R * K * L * S * C * P \text{ (Eq. 29)}$$

The parameters used in the formula are:

$$A = \text{soil loss} \left[ \frac{t}{ha * y} \right]$$

$$R = \text{erosive factor} \left[ \frac{Mj * mm}{ha * h * y} \right]$$

$$K = \text{soil erodibility factor} \left[ \frac{t * h}{Mj * mm} \right]$$

$L, S = \text{topographic factors}$

$P = \text{conservation techniques factor}$

- Factor R

The R parameter is characterized by a single value that represents the entire basin. It is calculated as the product between the total kinetic energy of a single event E (J/m<sup>2</sup>) and the maximum intensity reached in an interval of 30 minutes I<sub>30</sub> (cm/h) during the same event (Eq. 30). The sum of all events over the course of a year gives the annual R-value.

$$R = E * I_{30} \text{ (Eq. 30)}$$

Given that this procedure is complex as it requires the sampling of all the rainy events of the year, empirical formulas have been developed which link R to a parameter P which represents the depth of rainfall with a duration of 6 hours and a return period of 2 years. The first two formulae are calibrated respectively for the climate of West-USA and East-USA (Eqs. 31,32), meanwhile the third one is suitable for the rest of the countries (Eq. 33) with a climate reasonably close to the USA ones:

$$R = 16.55 * P^{2.2} \text{ (Eq. 31)}$$

$$R = 27 * P^{2.2} \text{ (Eq. 32)}$$

$$R = 27.38 * P^{2.17} \text{ (Eq. 33)}$$

To convert the formulas, which have been calibrated to American units, into the International System (SI), it is needed to multiply the result by a factor equal to 17.02.

- Factor K

It is defined as the soil erodibility factor (Eq. 34). It represents a measure of the tendency of soil particles to detach and to the consequent transport by runoff. The parameter value is influenced by the soil texture and its structure, organic content, and permeability properties. Initially the value was defined following tests conducted in situ. Subsequently, empirical formulas were developed:

$$K = 0.0034 + 0.0405 * e^{\left[ -\frac{1}{2} \left( \frac{\log D_g + 1.659}{0.7101} \right)^2 \right]} \text{ (Eq. 34)}$$

$$D_g = e^{(0.01 \sum f_i * \ln m_i)} \text{ (Eq. 35)}$$

Where:

$D_g = \text{geometric mean of soil particle diameter [mm]}$

$f_i = \text{\% of soil in the } i - \text{th class}$

$m_i = \text{arithmetic mean of soil particles of } i - \text{th class}$

- Factor C

It is the cover vegetation factor and takes into consideration the type and development of plants on the ground. Physically, it represents the degree of protection of the soil from raindrops due to the screen effect created by the leaves. The numerical value is established thanks to tabulated values:

Land Use	Value	Land Use	Value	Land Use	Value
Arable Lands		Arable Lands		Grasslands	
Barley/oats	0.21	Grass	0.16	Grasslands for extens. grazing	0.2
Alfalfa	0.02	Tobacco	0.49	Forests	
Peas	0.32	Rye	0.2	Forests	0.001
Potatoes	0.34	Average	0.3	Open forests	0.01
Fallow	1	Arable dense tree cover	0.2	Schrublands	
Vegetable crops	0.43	Arable med. tree cover	0.25	Dense schrublands	0.01
Grain corn	0.31	Arable sparse tree cover	0.3	Sparse schrublands	0.1
Grapes	0.05	Grasslands		Not erodible	
Root crops	0.36	Managed grasslands	0.01	Built-up areas/roads	0
Clover	0.08	Unmanaged grasslands	0.05	Rock outcrops	0

Table 1: Factor C list of values.

- Factor P

It takes into account the impact of erosion protection systems. If no action has been taken, a value of 1 is imposed. In other cases, consult the table:

Agricultural practice	Description	Value
Up and down slope	Growing crops vertically up and down a slope, rather than horizontally across	1
Cross slope	Growing crops perpendicular to the angle of the slope	0.75
Contour farming	Growing crops along lines of consistent elevation	0.5
Strip cropping (cross slope)	Growing different crops in strips perpendicular to the angle of the slope	0.37
Strip cropping (contour)	Growing different crops in lines of consistent elevation	0.25

Table 2: Factor P list of values.

- Factors L and S

They are both geometric factors and the formulas (Eqs. 36, 37) that characterize them are:

$$L = \left( \frac{\lambda}{22.13} \right)^m \quad (\text{Eq. 36})$$

$$S = 65.41 \sin^2 \theta + 4.56 \sin \theta + 0.065 \quad (\text{Eq. 37})$$

$\lambda$  = free length of slope

$m$  = empirical coeff. equal to 0.5 when slope exceeds 5%

$\theta$  = average slope evaluated in radians.



The RUSLE (Revised Universal Soil Loss Equation) model (Renard et al.,1991 (63)) has been proposed as an evolution of the USLE model. Conceptually, the two models are very similar, and the only differences lie in the definition of the geometric parameters L and S which in the RUSLE model are combined in a single length-slope parameter LS (Eq. 38) and in the possibility of having a digital interface (64).

For basins characterized by slopes in which  $\tan(\theta) > 0.09$  it is possible to use the formula:

$$LS = \left( \frac{\lambda}{22.13} \right)^{m'} (16.8 \sin \theta - 0.05) \quad (Eq. 38)$$

$m'$  is an empirical coefficient and derives from:

$$m' = \frac{f}{1+f} \quad (Eq. 39)$$

where  $f$  is a function of slope and is calculated as:

$$f = \frac{\sin \theta}{0.0896} \frac{1}{[3(\sin \theta)^{0.8} + 0.56]} \quad (Eq. 40)$$

A further change was made by Williams himself in 1975 to the formula of the USLE model. The original equation outputs only the average value of the annual soil loss. The new MUSLE model (Modified Universal Soil Loss Equation) allows the evaluation of this value also for different periods (65,66), such as seasonal or monthly. This result (Eq. 41) was obtained by replacing the R parameter with the new Rd parameter, defined as flow factor. The new equation is therefore:

$$Y_s = R_d * K * LS * C * P \text{ (Eq. 41)}$$

Rd is defined as:

$$R_d = 11.8 * (V * Q_p)^{0.56} \text{ (Eq. 42)}$$

Where:

$V = \text{water volume} [m^3]$

$Q_p = \text{peak flow at basin outlet} \left[ \frac{m^3}{s} \right]$

The models relating to the USLE were developed following studies and observations conducted on basins of different extensions in the American territory (67). Despite the introduction of empirical formulas and calibration coefficients introduced to adapt them to the Alpine and Mediterranean climates that characterize Italy, there are models developed through the analysis of basins similar to the Alpine ones. One of them is the Gavrilovic model (Gavrilovic, 1970 (68)). It is a semi-quantitative model, developed for basins located in the south-eastern part of Yugoslavia (Serbia), whose basic idea is to decouple the production of sediments, described by the W factor, and the retention of the sediments in the basin, described by the Ru factor. Several studies have demonstrated the effectiveness of this method also in Italian and Swiss basins, which have characteristics and climate similar to those in which the model was developed. After their evaluation, they are multiplied in order to determine the mean annual sediment crossing at the outlet of the basin (69). The formula and parameters used are as follows:

$$W = T * h * \pi * Z^2 * F \text{ (Eq. 43)}$$

Where:

$$W = \text{average annual sediment production} \left[ \frac{m^3}{y} \right]$$

$$h = \text{average annual rainfall [mm]}$$

$$F = \text{size of the basin [km}^2\text{]}$$

$$T = \sqrt{\frac{t_0}{10} + 0.1} \text{ [}^\circ\text{C]}; \text{ with } t_0 = \text{average annual air temperature [}^\circ\text{C]}$$

$$Z = Y * X_a * (\varphi + \sqrt{j}) = \text{erosion coefficient}$$

$$Y = \text{soil cover coefficient}$$

$$X_a = \text{soil resistance coefficient}$$

$$\varphi = \text{kind and extension of erosion coefficient}$$

$$j = \text{average slope of the basin}$$

$$R_u = \frac{(O * D)^{0.5}}{0.25 * (L + 10)} \text{ (Eq. 44)}$$

Where:

$O$  = perimeter of the basin [km]

$L$  = length of the basin [km]

$D$  = average altitude gradient [km]

The final result is obtained from the combination of the factor  $W$  and  $R_u$ :

$$G = W * R_u \text{ (Eq. 45)}$$

Where:

$G$  = average annual sediment  $\left[ \frac{m^3}{y} \right]$

### **2.4.3 Physically-based model: SWAT**

Unlike the semi-empirical models analyzed before, the SWAT model allows the geologic-erosive component to be analyzed at the channel scale by defining the amounts of eroded material along the course of the main river and its relative tributaries. In addition to this, the software also allows for the analysis of the hydraulic component, again at the channel scale, allowing for the definition of both the average flow and the peak flow rate over each section of the hydrographic network within a user-defined time interval. The SWAT model, acronym of Soil and Water Assessment Tool, allows to analyze and model a wide range of river basins. It was developed by Dr Jeff Arnold (70) for the USDA (United States Department of Agriculture), specifically for the ARS (Agricultural Research Service) department. The software allows to predict the impact of land use practices on water and sediments as the characteristics of the basin vary. The model is physically based: in fact, it exploits specific information about the characteristics of topography, land use, soil, and rainfall. This choice leads to benefits in terms of usability, as direct flow measurements are not necessary and moreover it is possible to model conditions different from the real ones (e.g., variations in land use, climate, or vegetation). SWAT, while it can model extremely complex processes in terms of amount of data such as bacterial transport that are not considered for the study case. It is computationally efficient as it allows to simulate even very large basins without excessive investments in terms of time. Finally, it is useful for modeling and analyzing long-term impacts, particularly in terms of erosion and deposition. The software allows it to be used by multiple GIS interfaces, in particular by QGIS and ArcGIS. In the first case the program will take the name QSWAT, which is the interface used. It presents 3 successive steps: in the first one the geometry and the Digital Elevation Model (DEM) of the basin are defined. Starting from this, the stream network and the relative input and output areas of the basin are evaluated and determined. After defining all the above parameters, the software produces the sub-basins. The second section refers to the definition of the Hydrogeological Response Unit (HRU), in which the user is asked to enter land use and soil type maps. The HRUs are further subdivisions of the sub-basins, homogeneous in terms of soil and land use. Each HRU is independent from the others and there is no interaction between different HRUs in the same sub-basin. All the results of sediment volumes, pollutants and runoff are evaluated in the single HRU and finally summed for the single sub-basin.

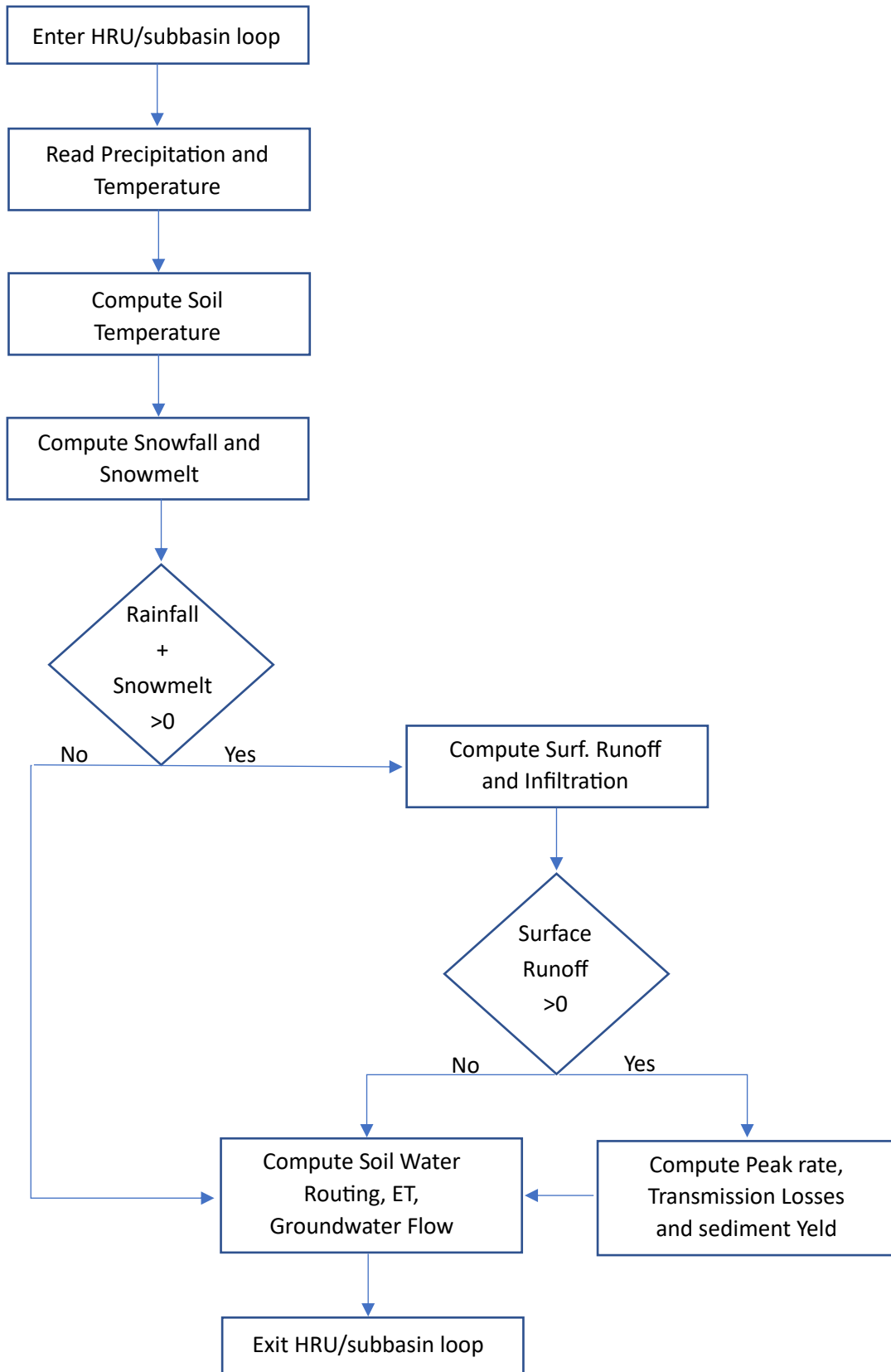


Figure 13: HRU/subbasin command loop (70).

The hydrological cycle (Figure 14) simulated by SWAT is based on the Water Balance Equation:

$$SW_t = SW_0 + \sum_{i=1}^t (R_{day} - Q_{surf} - E_a - w_{seep} - Q_{gw}) \quad (Eq. 46)$$

- $SW_t$  is the final soil water content (mm H<sub>2</sub>O),
- $SW_0$  is the initial soil water content on day i (mm H<sub>2</sub>O),
- $t$  is the time in days,
- $R_{days}$  is the amount of precipitation on day i (mm H<sub>2</sub>O),
- $Q_{surf}$  is the amount of surface runoff on day i (mm H<sub>2</sub>O),
- $E_a$  is the amount of evapotranspiration on day i (mm H<sub>2</sub>O),
- $w_{seep}$  is the amount of water entering the non saturated zone from the soil profile on day i (mm H<sub>2</sub>O),
- $Q_{gw}$  is the amount of return flow on day i (mm H<sub>2</sub>O).

The subdivision of the watershed allows to model the different evapotranspiration for the different covers and soils. This allows for a better physical description of the water balance.

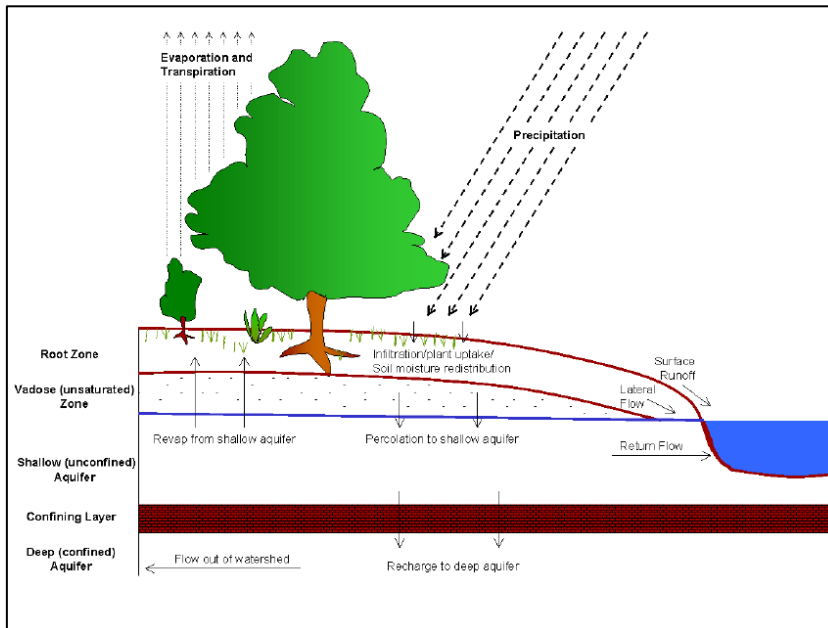


Figure 14: Schematized hydrological cycle (70).

The hydrological cycle is strongly influenced by climate change and changes in land use. Changes induced by these two factors affect water circulation and infiltration by implying imbalances in the cycle itself, consequently changing runoff. Climate change produces sudden changes to the hydrological regime of the basin producing extreme events, particularly flooding and alluvium (4).



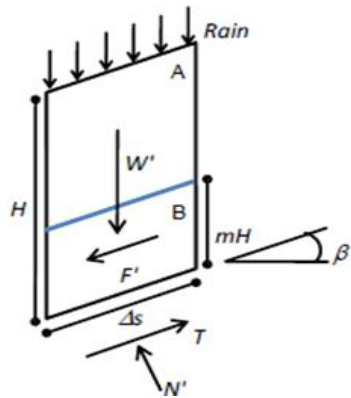
#### **2.4.4 Stability Analysis: SLIP and Takahashi models**

The SLIP (Shallow Landslides Instability Prediction) model is a valid tool that allows the evaluation of the safety factor  $F_s$  of slopes at risk of failure. The safety factor is the representation of the threshold at which the instability occurs. The model allows the study of slopes and much larger areas thanks to the reduced computational cost. SLIP model is physically based and leads to a safety factor  $F_s$ , which is a function of the main variables and characteristics of the slope such as the rainfall discharge, the geometrical aspects of the slope and the geotechnical and hydraulic characteristics of the soil.

The model is also based on some fundamental assumptions:

- The slope is considered to be of infinite length since the slope length  $L$  is much greater than the depth of interest  $h$ .
- A shallow landslide affects a depth that extends for a maximum of 1-2 meters.
- Water infiltrating the soil matrix plays a vital role in slope stability. In fact, as the rain event proceeds, the volumes of saturated areas tend to grow until the level of instability is reached.

The ultimate goal of the method is to obtain an  $F_s$  (Eq. 49) through the limit equilibrium applied to an equivalent slope of infinite length by using the ratio between the sums of the stabilizing force (Eq. 47) and of the destabilizing ones (Eq. 48). The soil is divided, for sake of simplicity, into two distinct parts (Figure 15): one totally saturated while the other partially saturated. The saturated layer has a thickness corresponding to  $mH$  ( $0 < m < 1$ ) (71).



$$T_s = N' + \tan \varphi' + C' \text{ (Eq. 47)}$$

$$T_d = W' \sin \beta + F' \text{ (Eq. 48)}$$



$$F_s = \frac{T_s}{T_d} \text{ (Eq. 49)}$$

Figure 15: Actions considered into SLIP model.

Where:

$F'$  = seepage force

$W'$  = weight of soil

$T$  = shear force

$N'$  = normal eff. force

To evaluate the condition of incipient collapse for a flow, the SLIP model is not suitable. For this reason, the model developed by Tamotsu Takahashi (72) in 1987 could be applied. It is a deterministic method widely used for this type of events.

The method provides two criteria (Eqs. 50, 52) that the slope must be fulfilled at the same time in order to be prone to a debris flow.

1<sup>st</sup> criterion, safety factor FS ( $\tilde{\theta}$ )

$$FS(\tilde{\theta}) = \frac{\tan(\tilde{\theta})}{\tan(\theta)} = \frac{C^*(\sigma - \rho)}{C^*(\sigma - \rho) + 3\rho} * \frac{\tan(\varphi)}{\tan(\theta)} \quad (Eq. 50)$$

Where:

- $C^*$ : grain concentration by volume in the static debris bed that can be computed as

$$C^* = \frac{\text{soil content}[m^3]}{\text{soil content} + \text{soil water volume}[m^3]}$$

- $\sigma$  [kg/m<sup>3</sup>]: density of the river bed material
- $\rho$  [kg/m<sup>3</sup>]: water density
- $\varphi$  [°]: internal friction angle of the bed
- $\theta$  [°]: slope angle

The criterion derives from the inequality:

$$\tan\theta \geq \frac{C^*(\sigma - \rho)}{C^*(\sigma - \rho) + 3\rho} * \tan(\varphi) = \tan(\tilde{\theta}) \quad (Eq. 51)$$

This inequality is based on the comparison between the slope angle  $\theta$  and the angle  $\tilde{\theta}$  which contains a sort of correction of the internal friction angle  $\varphi$ , made referring to the behavior of the riverbed during debris flow phenomena.

This criterion can be considered as valid only under the hypothesis of infinite slope, which usually means when the slope length is much higher than the slope depth.

2<sup>nd</sup> criterium, definition of safety factor FS(q):

$$FS(q) = \frac{2}{q^*} = \frac{2}{\frac{q_0}{\sqrt{gd^3}}} \quad (Eq. 52)$$

Where:

- $q_0$  [ $\text{m}^3/(\text{s} \cdot \text{m})$ ]: surface water discharge per unit width
- $g$  [ $\text{m}/\text{s}^2$ ]: acceleration due to gravity
- $d$  [ $\text{m}$ ]: representative grain diameter of the bed

The criterion allows to understand when the surface water discharge per unit width is enough in order to lead the formation of a debris flow phenomenon (72).

### 3. Case study: Misa Basin

The study aims to analyze the phenomenon of erosion in the drainage basin of the Misa River, following the flood event of 15<sup>th</sup> and 16<sup>th</sup> September 2022. The Misa basin is located in the Marche region in central Italy and has its outlet at the city of Senigallia, in the province of Ancona (Figure 16). The Misa River originates from the southwestern slopes of the mountains in the area of the municipality of Genga (AN) and flows for about 50 km before reaching the Adriatic Sea. The catchment area covers an area of 384 km<sup>2</sup>, ranging from a minimum height close to sea level to a maximum height of 750 m asl in the Apennine zone.

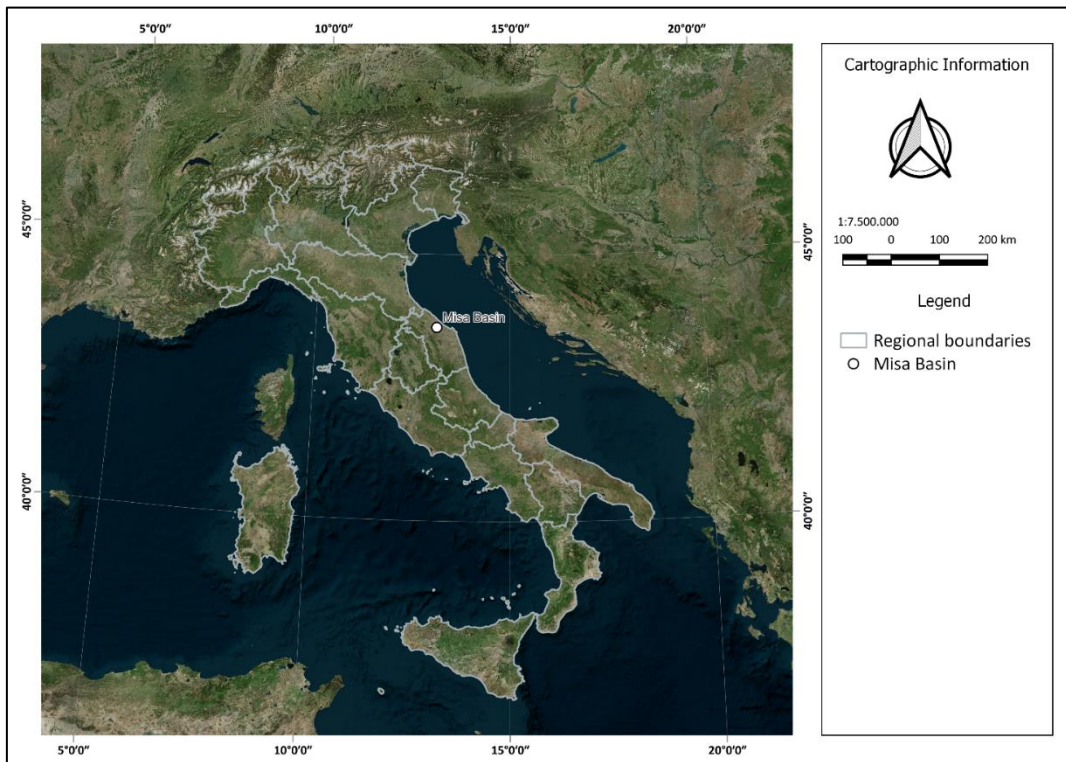


Figure 16: Geographical framework of the Misa Basin.

Shifting focus to the geomorphological features of the Misa basin, it can ideally be divided into a more mountainous area to the south-west, which is part of the Umbria-Marche Apennines, and a flatter piedmont area that extends to the Adriatic Sea. From a geological point of view, the montane belt is characterized by bedrock outcropping in correspondence with the watercourses and the lithology is mainly marly limestone. On the contrary, the foothills area is made up of thick layers of recent alluvial material and eluvial-detrital materials (Figure 17). The large amount of deposit is due to the Misa

drainage network, which transports sediments throughout the channel and along the floodplains. The map (Figure 18) shows the morphology of the area thanks to the Digital Terrain Model (DTM), with a resolution of 10x10 m, and the various municipalities present within the basin, with their area of competence. Most of the basin is characterized by the presence of fields with intensive cultivation, and only close to the outlet there are urbanized areas with significant extents. The area was subjected to intense flooding between September 15<sup>th</sup> and 16<sup>th</sup>, 2022, where erosive action played a major role, causing intense sediment transport to the outlet. The area had already been affected by a similar event in May 2014, when the Misa River, along with its main tributary, the Nevola River, overflowed causing extensive damage but fortunately without any casualties. The September 2022 event not only caused extensive damage on the riverbed and banks of the stream network but led to the loss of several lives.

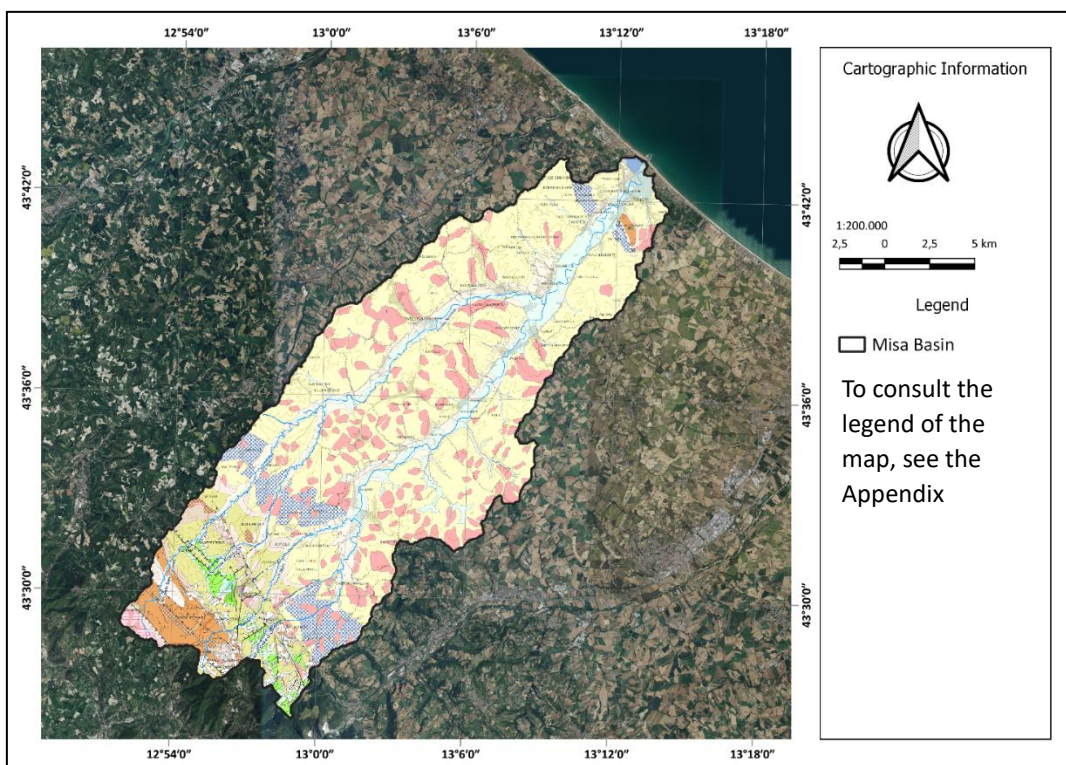


Figure 17: Geology of Misa Basin from the Geological Map of Italy (CARG project).



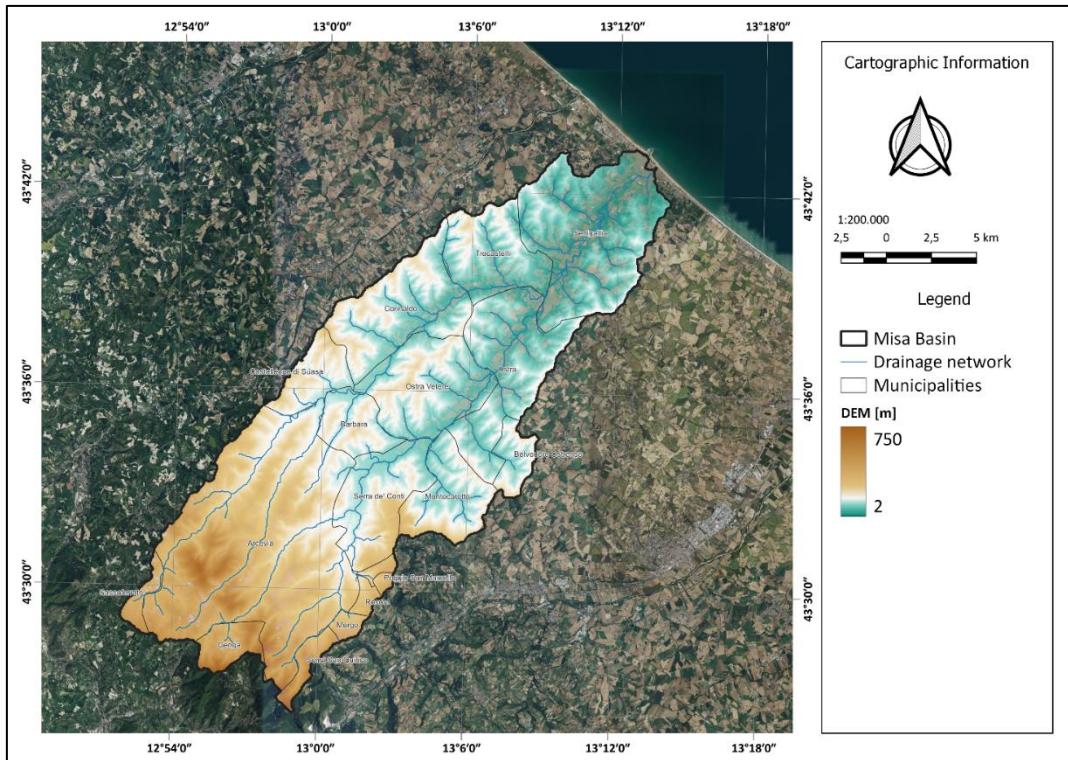


Figure 18: DEM and drainage network of the Misa basin.

### **3.1 Hazard and risk mitigation in Marche region**

Land governance has its relevance when it comes to hydrogeological instability, as hydraulic works in the riverbed can mitigate what are the highest peak flows, through, for example, the lamination of runoff. In the Marche region, the "Piano Stralcio di bacino per l'assetto idrogeologico ", (73), which contains the articles of the implementation rules, has been drawn up in accordance with Article 17 paragraph 6-ter of Law of May 18, 1989, No. 183 and according to the request of Article 1 of Law August 3, 1998, and by Article 1-bis of Law of December 11, 2000, No. 365.

In the purposes of the plan, regional river basins are initially defined (Articles 1 and 2) and within these were identified:

- hydraulic hazard areas in which potentially floodable areas are defined,
- gravitational hazard areas in which slope strips in unstable condition are defined,
- areas with elements in hydrogeological hazard situations (residential buildings, infrastructure and production facilities).

Part 2 of the PAI takes into account the hydraulic planning and defines in Article 6 the purposes:

- identification on historical-geomorphological basis of flood inundation zones with return times up to 200 years,
- the definition of a management strategy aimed at safeguarding natural hydraulic dynamics, with reference to flooding and riverbed evolution, favoring the restoration of the natural features of the stream network,
- definition of a policy of prevention and mitigation of hydraulic risk.

Article 7 accordingly defines prohibitions and permitted actions in floodplains:

Actions prohibited:

- actions that totally or partially reduce the flood capacity,
- installation of waste disposal facilities or landfills,
- temporary deposits resulting from mining activities,
- excavations or lowering of the ground level that could compromise the stability of the embankment.



Actions allowed:

- interventions aimed at the reconstitution of altered natural balances and the elimination, as far as possible, of incompatible factors of anthropogenic interference,
- hydraulic accommodation interventions such as embankments, bank defenses, expansion tanks, etc. In the presence of significant natural or environmental features, interventions must be compatible with the specificity of places,
- wastewater treatment plants if there is an impossibility of installing them elsewhere. The final opinion falls under the opinion of the Basin Authority,
- interventions for the accommodation of the riverbed.

Despite the definition of this plan, it is evident that there is a lack of analysis for flood events for exceptional storm events with return period greater than 200 years, which in recent years are increasingly present not only in the Marche region but throughout Italy. The Misa basin was subject to a flood prior to the September 2022 flood, which occurred between May 2<sup>nd</sup> and 4<sup>th</sup>, 2014. The event caused the overflow of the Misa and Nevola, its main tributary with the consequent flooding of the municipalities of Senigallia, Trecastelli, Ostra, and Corinaldo, all in the province of Ancona. A state of emergency was declared at the time, and the head of Civil Protection, through the issuance of the July 10<sup>th</sup>, 2014, Ordinance No. 179 led to the initiation of post-emergency actions, in fulfilment of the rules defined by state and regional regulations, particularly according to the provisions of the PAI. The in-depth study involved both the reconstruction of the event, with reference to the overflow dynamics, and the definition of the flooded areas. Therefore, the mayor established a working group aimed at identifying the necessary measures to increase the level of hydraulic safety. With the resolution of March 25<sup>th</sup>, 2016, n.67 (74) following the principle defined by the PAI (73) in 'art. 6 paragraph 1 that defines" *a policy of prevention and mitigation of hydraulic risk through the formulation of actions and standards*", it was decided to reduce as much as possible the peak flows that would reach Senigallia. This would be achieved by the lamination of runoff in inland areas and expanding the the watercourse section within the city. Based on the calculations conducted, the aim was to reduce the estimated 200-year peak flow rate from 590 m<sup>3</sup>/s to

a controlled flow rate of 240 m<sup>3</sup>/s. This intervention, together with maintenance and cleaning of the riverbeds, would have allowed transit on the bridges, albeit without safety breaks. Despite this, the tender for the start of the work was not completed until April 21<sup>st</sup>, 2022, more than 6 years later (75). The construction time for a lamination tank in the Bettollelle area was estimated to be 510 days. The intervention time delay did not even allow the work to begin, thus leading to the catastrophic results of September 2022, far worse than those of 2014.

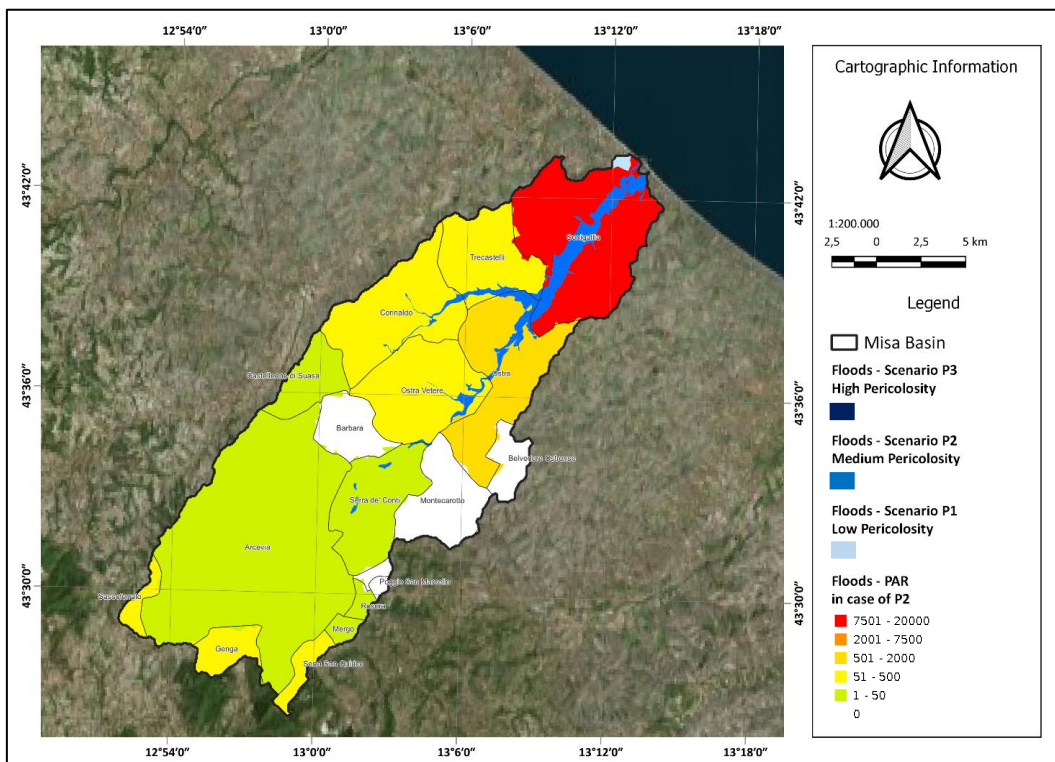


Figure 19: PAI scenarios of hazard for flooding and Population at Risk (PAR) in case of P2.

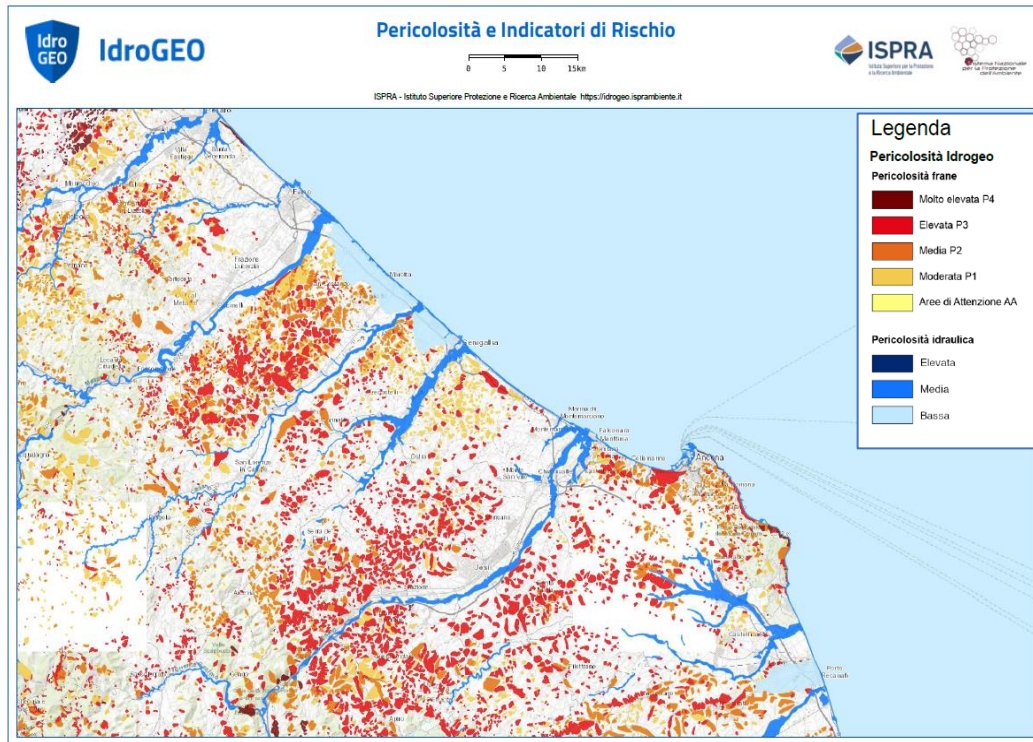


Figure 20: Geologic and hydraulic hazard map of Ancona Province by IdroGEO portal.

The maps in Figures 19 and 20 are obtained from the IdroGEO portal on the ISPRA (Istituto Superiore Per la Ricerca Ambientale) website and shows the Misa basin and the entire province of Ancona in the Marche region. The map in Figure 19 shows the hydraulic hazard levels and resulting population at risk for the Misa basin as defined by the PAI. The map in Figure 20 shows the hydraulic hazard level for the entire province of Ancona, and the geological hazard level. It can be seen that the Misa basin, and in general the Province of Ancona, is subject to a medium level of hydraulic hazard, with return times between 100 and 200 years, and the population at risk is mostly concentrated near the delta in the Senigallia area, as it is the most densely populated. These data make it clear that the area is not characterized by critical hazard levels (low return times). This fact must put even more focus on extreme events, which can induce high damage even in areas with moderate hazard levels. This fact demands a greater commitment in land-use planning towards hydrogeological risk. This is concretely translated into the construction of works to reduce the possible flood flows and the planning of an effective warning system to ensure the safety of citizens. This is especially crucial for those living in the villages further downstream, where flows tend to channel.

## 4. Analysis of the flood event of September 2022

### 4.1. The flood

During the days between 15<sup>th</sup> and 16<sup>th</sup> September 2022, the Marche region was hit by an extremely violent rainfall event, in particular the basins of Misa, Esino, Cesano and Metauro. The scale of the event was so massive that it is described as outstanding and ranks as an "outlier event". This means that it is not included in the modeling of flood events conducted and considered. More specifically, it was a V-shaped self-healing thunderstorm (76), which will be described in detail later. The main feature of these events is the ability to feed continuously thanks to a constant flow of humid and cold air in the upper areas of the troposphere which contrasts with the presence of warmer air masses near the ground. This induces wind shear which causes the formation of V-shaped supercells, which are quasi-stationary storms leading to exceptional and persistent rainfall over the same area. The rainfall stations present in the area recorded average values of more than 100 mm of rainfall with peaks recorded in the municipality of Cantiano (PU) which reached a value of 419 mm in a day (74) (Figure 21).

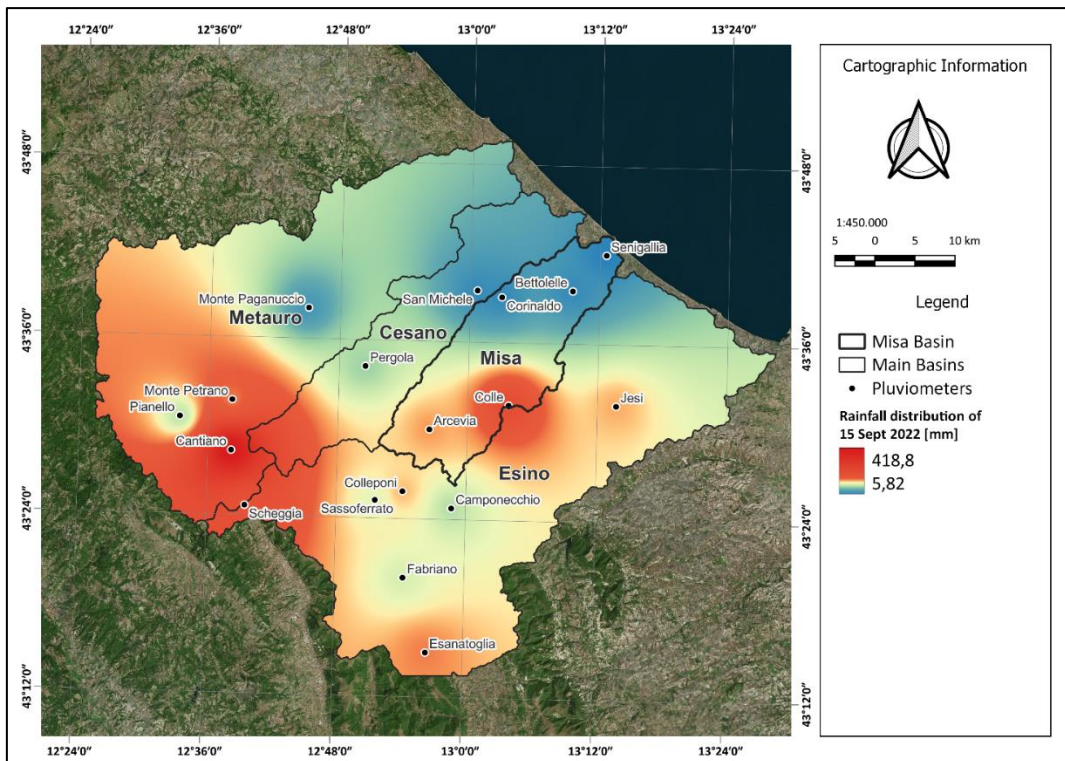


Figure 21: IDW map of 15<sup>th</sup> September 2022.

The exceptional rains caused the rapid saturation of the basin causing strong flood waves which caused extensive damage to both the artificial structures and the banks and slopes themselves due to the large amount of debris carried by the current. In fact, landslides and structural failures were recorded in correspondence with the main road sections and furthermore, in correspondence with inhabited centers, the flow of debris and water caused damage to buildings and even the death of 13 people (77).

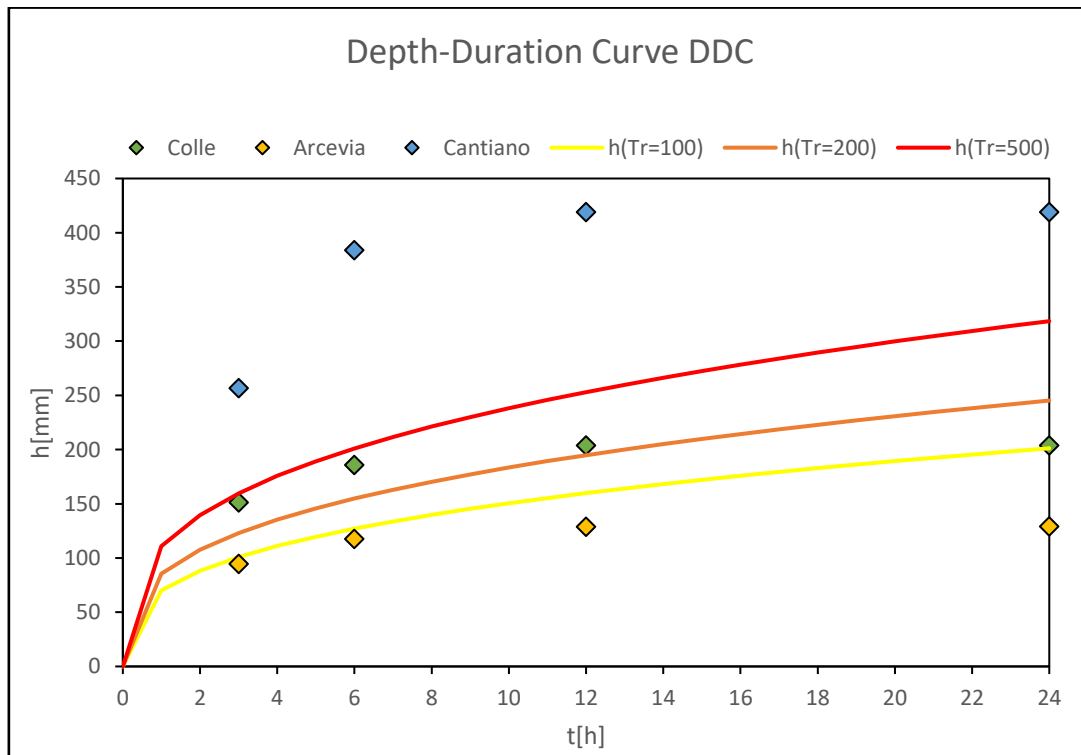


Figure 22: Depth-Duration Frequency curves for 100, 200 and 500 years and comparison with Colle, Arcevia and Cantiano pluviometers (Figure 19).

The graph (Figure 22) shows the comparison between the rainfall possibility curves for three return periods corresponding to 100, 200 and 500 years (78,79). They express the relationship between precipitation depths and their duration for different return times, which is defined as the probability of occurrence of a given event in a given year. In the case of alluvial phenomena, the return time is the probability that a certain amount of rain will occur in any year. The curves in the graph are estimated from the data relating to the maximum precipitation heights expected after 1, 3, 6, 12, 24 hours for the “Ancona Torrette” station (79). The series of data used goes from 1955 to 2007 and refers to two different datasets. The first goes from 1955 to 1989 and derives from the digitization of paper data made available by Servizio Idrografico e Mareografico Nazionale. The second



goes from 1990 to 2007 and are derived from the database of Centro Funzionale. For each series, the height-duration and intensity-duration relationships of the annual maxima were evaluated by Civil Protection. These relations follow a characteristic trend that follows a 3-parameter law:

$$i = \frac{a}{(b + \delta)^m} \text{ (Eq. 52)}$$

Where:

$i = \text{rainfall intensity}$

$\delta = \text{fixed duration}$

$a, b, m = \text{law's parameters}$

The data used are the following:

Duration[h]\RetT[y]	2	5	10	20	50	100	200	500
1	20.77	28.68	35.5	43.57	56.79	69.27	84.43	109.63
3	30.63	42.28	52.35	64.24	83.75	102.15	124.51	161.66
6	38.46	53.09	65.73	80.66	105.15	128.25	156.32	202.97
12	47.99	66.25	82.02	100.66	131.22	160.06	195.09	253.3
24	59.71	82.43	102.05	125.24	163.25	199.13	242.71	315.13

Table 3: Rainfall height in function of Duration and Return Period.

These data were derived through probabilistic relationships by Civil Protection of Regione Marche with a Frechet probability law (79), which was preferred to the Gumbel that is normally used because the data set analyzed was better approximated by the former.

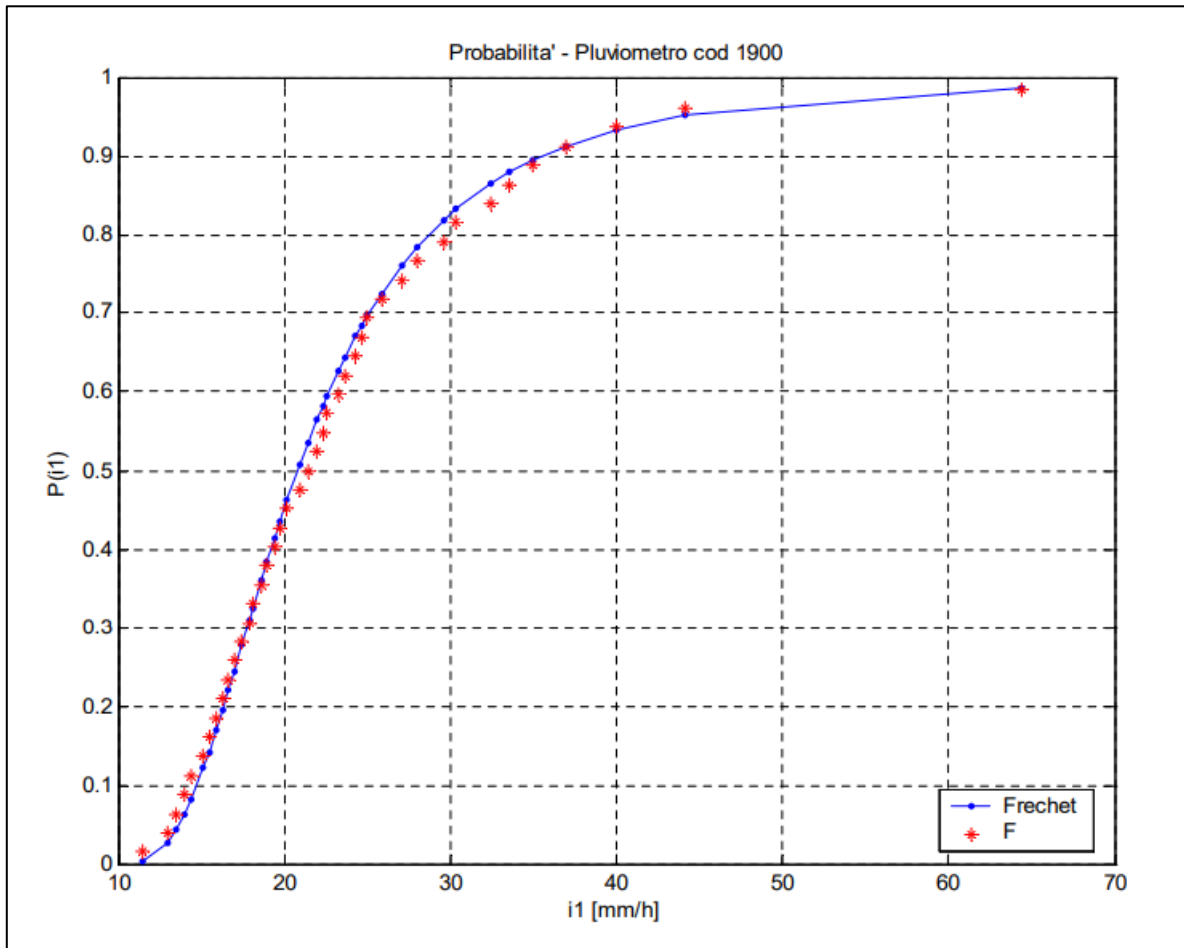


Figure 23: Cumulative probability of the maximum hourly intensity of the year at the "Ancona Torrette" rain gauge, with Frechet distribution (79).

In statistics, Gumbel's, Frechet's and Weibull's laws are part of the family of probability laws defined as generalized extremes, used mainly to model phenomena characterized by extreme events, as in the case of rainfall. In particular, Gumbel is defined as type 1, Frechet as type 2 while Weibull as type 3. The definition is unique for the three laws, and they differ only in the value that the parameter  $\xi$  takes, which determines the behavior of the law in the tails at the extremes.

The cumulative CDF function is as follows:

$$F(x; \mu, \sigma, \xi) = e^{-\left[1 + \xi \left(\frac{x - \mu}{\sigma}\right)^{\frac{1}{\xi}}\right]} \quad (Eq. 53)$$

While the probability density function PDF (Eq. 54) is obtained by deriving the former (Eq. 53):

$$f(x; \mu, \sigma, \xi) = \frac{1}{\sigma} \left[1 + \xi \left(\frac{x - \mu}{\sigma}\right)\right]^{-\frac{1}{\xi} - 1} e^{-\left[1 + \xi \left(\frac{x - \mu}{\sigma}\right)^{\frac{1}{\xi}}\right]} \quad (Eq. 54)$$

The Gumbel distribution (Eq. 55) is obtained by imposing the parameter  $\xi$  equal to zero:

$$F(x; \mu, \sigma, 0) = e^{-e^{-\frac{(x - \mu)}{\sigma}}} \quad (Eq. 55)$$

The Frechet distribution (Eq.56) is obtained by imposing  $\xi = \alpha^{-1} > 0$

$$F(x; \mu, \sigma, \xi) = \begin{cases} 0 & x \leq \mu \\ e^{-\left(\frac{x - \mu}{\sigma}\right)^{-\alpha}} & x > \mu \end{cases} \quad (Eq. 56)$$

The Weibul distribution (Eq.57) is obtained by imposing  $\xi = -\alpha^{-1} < 0$

$$F(x; \mu, \sigma, \xi) = \begin{cases} e^{-\left(\frac{-(x - \mu)}{\sigma}\right)^{\alpha}} & x < \mu \\ 1 & x \geq \mu \end{cases} \quad (Eq. 57)$$



Thus, the three laws have three differently defined domains: in Gumbel the domain is defined  $\forall \mathbb{R}$ , in Frechet there is a lower limit, and in Weibul the limit is upper (80). To establish the rainfall height value at each interval of time for a particular Return Period, a monomial power law (Eq. 58) is generally used to describe the relationship between height and duration:

$$h = at^n \text{ (Eq. 58)}$$

Where:

$h = \text{rainfall depth [mm]}$

$t = \text{duration [h]}$

$a, n = \text{coefficient } f(Tr)$

The estimate of a and n for each curve is obtained through the logarithm of the precipitation and duration values using the least squares method (81,82).

Starting from the initial equation it can be passed to the logarithmic formula:

$$\log h = \log a + n \log t \text{ (Eq. 59)}$$

By imposing:

$$Y = \log h \text{ (Eq. 60)}$$

$$A = \log a \text{ (Eq. 61)}$$

$$X = \log t \text{ (Eq. 62)}$$

Finally obtaining the equation of a line:

$$Y = A + nX \text{ (Eq. 63)}$$

The number of height-duration pairs is defined as M, which in this case is 5. A and n are instead obtained by approximating the straight line with the least squares interpolation straight line (Eqs. 64, 65), which minimizes the sum of the squares of the distances between the straight line and the points identified by the pairs of values.

The equations are:

$$A = \frac{M \sum \log t \sum (\log h)^2 - \sum \log t \sum (\log t)(\log h)}{M \sum (\log t)^2 - (\log t)^2} \text{ (Eq. 64)}$$

$$n = \frac{M \sum (\log t)(\log h) - \sum \log t \sum \log h}{M \sum (\log t)^2 - (\log t)^2} \text{ (Eq. 65)}$$

where  $a = 10^A$

The three curves obtained were compared with the rainfall data obtained from 3 stations on 15<sup>th</sup> September 2022. The selected stations located in Arcevia, Colle and Cantiano (Figure 21). The first two stations fall within the Misa basin while the last is in the province of Pesaro Urbino and is approximately 50 km from Senigallia. From the first two stations, the maximum rainfall values were obtained for durations of 3, 6, 12, 24 hours. In the case of Arcevia, the rainfall lasts from 3 to 6 hours with a return period of 100 years, which decreases considerably for periods of 12 and 24 hours. Colle, on the other hand, represents the station with the highest rainfall data, as far as the stations present in the basin are concerned. The rains with a duration of 3 and 6 hours reach return times of 500 years and then progressively decrease for durations of 12 and 24 hours in which the rains have a return time of 200 and 100 years respectively. The situation is

different for the Cantiano station where the rains have been exceptional, and for all durations the values are above the return time of 500 years, settling around return times in the order of thousands of years. The volume of precipitated water was so high that the outflow from the basin led to widespread flooding in the coastal areas at the outlet in the Senigallia area and the triggering of landslides and debris flows along the entire course of the Misa with consequent loss of human life and high economic damage. It is reasonable to assume values for return times of more than 200 years as the flood developed in inland areas of the region that were subjected to rainfall with average return times above that value. Moreover, it is the time normally chosen for the dimensioning of the hydraulic works present in the area. In fact, they were not sufficient to limit the damage caused by the flood (73)

## 4.2 Rainfall analysis and comparisons

After analyzing the September 2022 flood event and its return times, it is useful to look at the rainfall trends over time in order to understand the dynamics of the event and to make comparisons with past flood events. The analysis was conducted on:

- The flood event of 15<sup>th</sup> and 16<sup>th</sup> September 2022,
- the flood event of 2<sup>nd</sup> and 4<sup>th</sup> May,
- the year 2022,
- the year 2014,
- the year 2017.

These periods are the same taken into account for the SWAT analysis. The last one will serve as the comparative term. The rain gauges used for all the following analyses are the same and are shown in Figure 24:

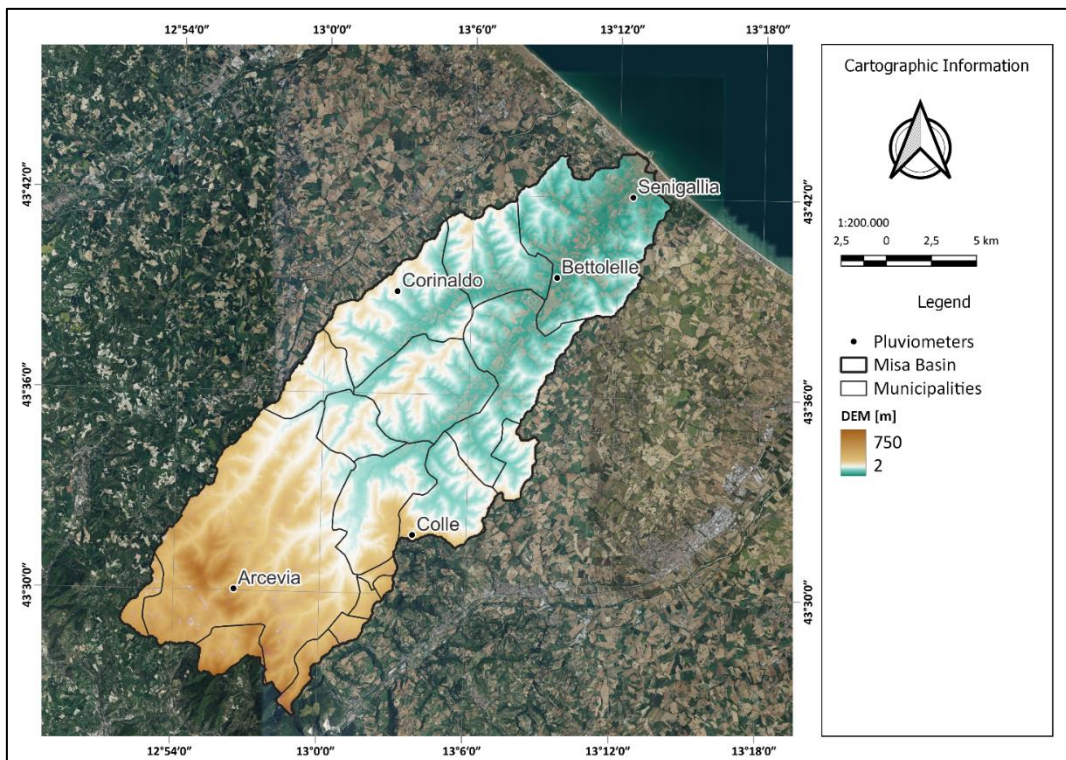


Figure 24: Pluviometers locations.

The graph (Figure 25) shows the rainfall assessed every 15 minutes and its cumulative amounts for the flood event of 2022. It can be immediately seen the wide gap between the measurements from Colle and Arcevia, in the western area of the region, compared to those obtained in the eastern portion. This distribution is typical of flash floods in that there is heavy rainfall in localized areas that discharge high amounts of water and debris downstream. During the event, major population centers, particularly the city of Senigallia did not anticipate such catastrophic consequences as there was light rainfall in the area. In addition, another factor that contributed to the increased hazard of the event was the failure to clean the riverbeds, which had been dry over the summer due to a prolonged dry spell. This greatly increased the transposed material of the flood wave, which aggravated the damage and contributed to the overflow from the banks.

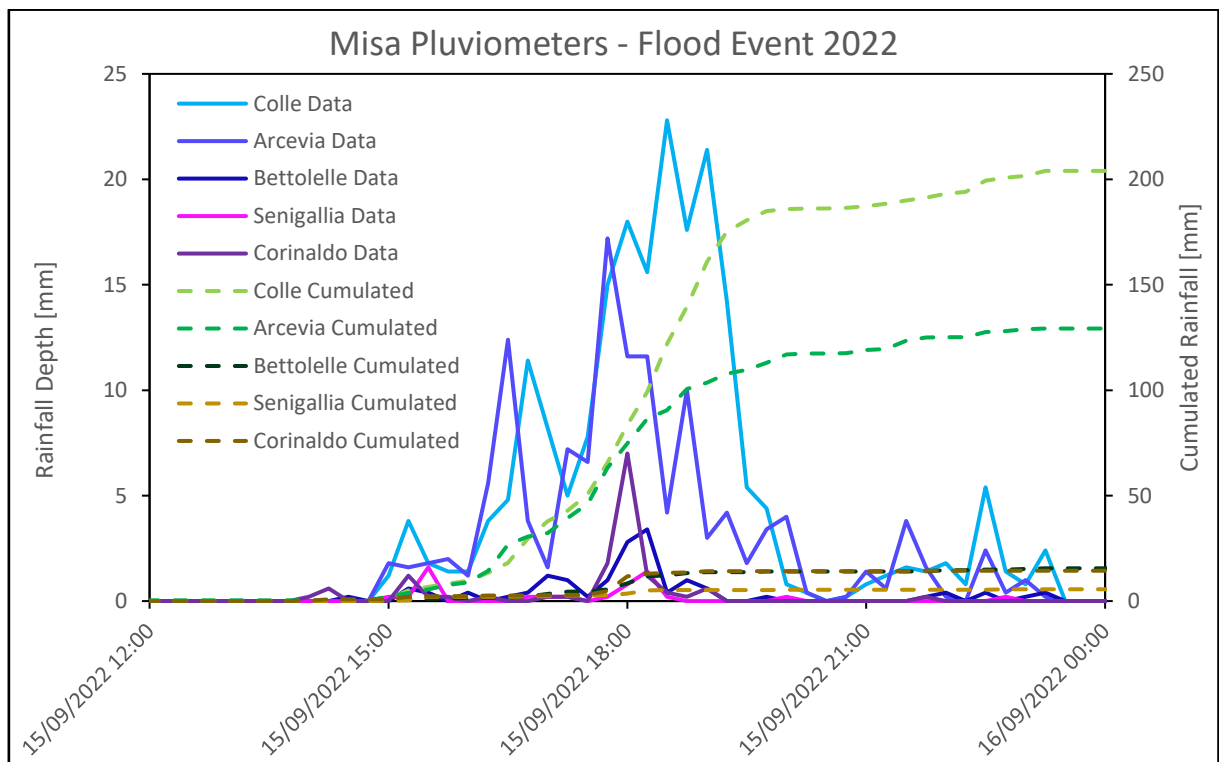


Figure 25: Rainfall data and cumulated rainfall from Misa pluviometers during Flood Event of September 2022.

The dynamics of the 2014 event is different from that of 2022, and this is evident from the graphs of precipitation and its cumulated (Figure 26). In fact, the event was more distributed throughout the basin and extended for a longer time. Nevertheless, rainfall peaks every 15 minutes reached highs up to 18 mm in Corinaldo, lower than the 2022 levels that reached values over 20 mm. The peak also persisted for a period of time of less than 15 minutes, then settled back to around 5mm. In addition, cumulations reached maximum value of 100 mm/event, much lower than the 220 mm/event recorded in 2022.

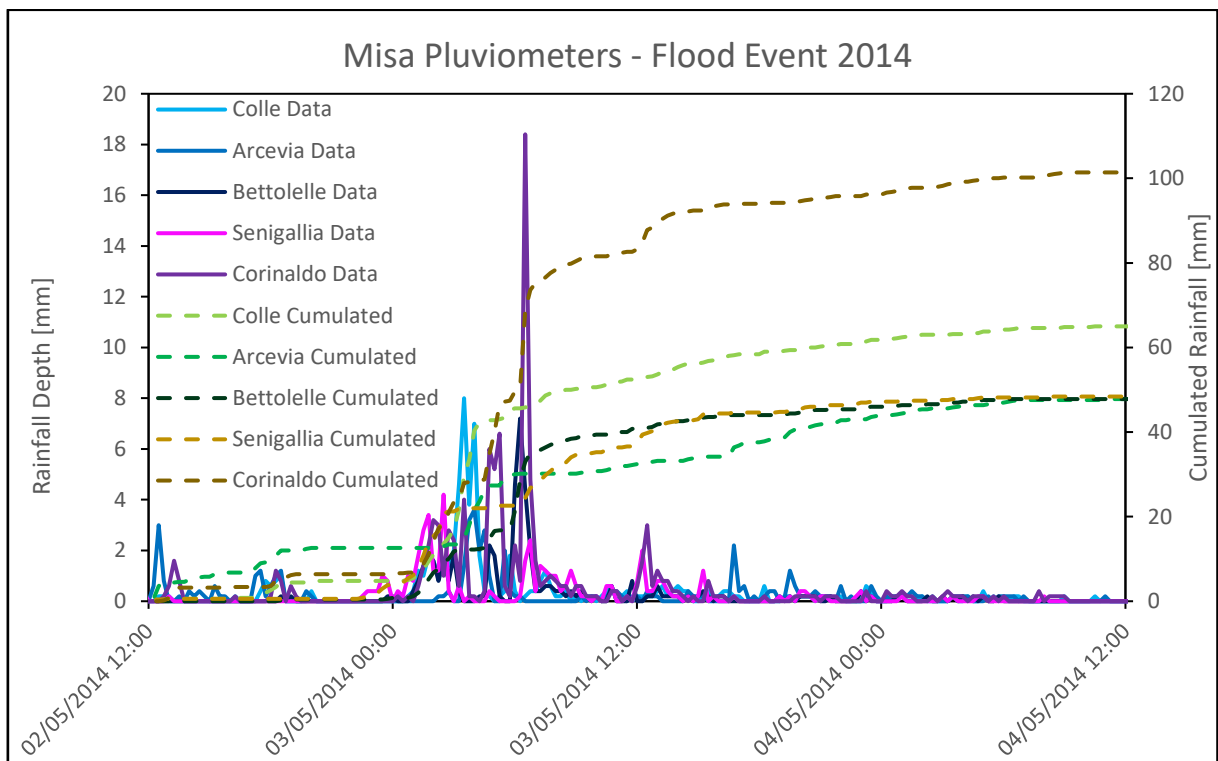


Figure 26: Rainfall data and cumulated rainfall from Misa pluviometers during Flood Event of May 2014.

In the case of annual analyses, only graphs containing daily precipitation over the entire year, which in this case is 2022 (Figure 27), are shown. In addition to this, a threshold value set at 30 mm of daily rainfall has been imposed, which defines extreme rainy days according to the Technical Office of Meteorology of the Italian Aeronautics. Through this, it is possible to determine how many relevant thunderstorms have hit the area. The number will be useful in obtaining correlations about average river discharge values, which are dependent on rainfall and storm events. In this case, the strongest thunderstorms are concentrated more on the mountainous areas inland and reach a maximum of 7 events/year in the Arcevia area, to a minimum of 3 events/year along the coastal areas. In addition, all these events have values reaching at least 40 mm of daily rainfall.

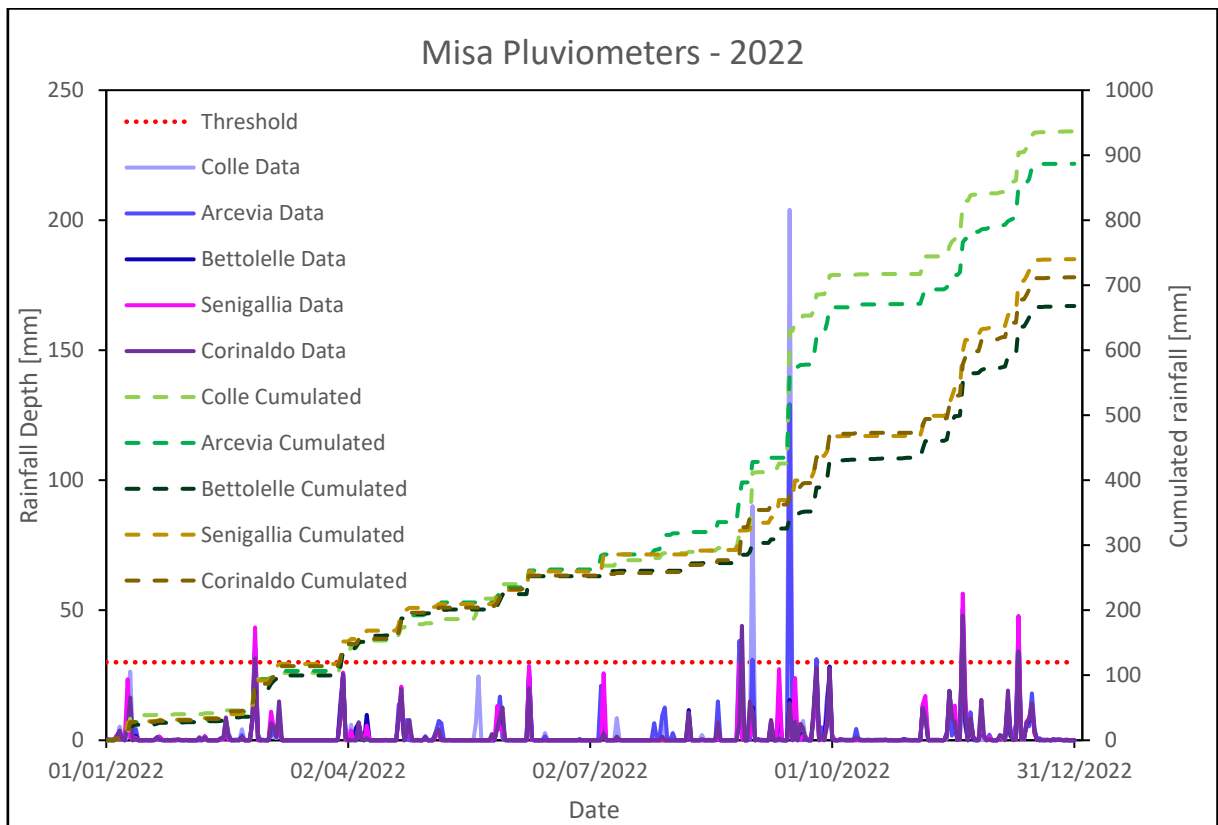


Figure 27: Rainfall data and cumulated rainfall during 2022.

The year 2014 recorded 6 to 7 events (Figure 28), depending on the rain gauge considered, above 30 mm. A preliminary analysis reveals that there were more events overall than in 2022, and they are relatively evenly distributed throughout the year. Excluding the May flood event, all these events are below 80 mm, categorizing them as within the range of heavy rainfall. In contrast, the distribution of 2022 is more concerning as the events are concentrated only in the second half of the year and feature extreme peak values, denoting an extremely dry spring and particularly dry summer. This precipitation distribution is typical of tropical climates where rainy seasons alternate with periods of warm and stable weather. The cumulative rainfall for the entire 2014 and 2022 years are similar in general, and almost the same for Arcevia and Colle stations.

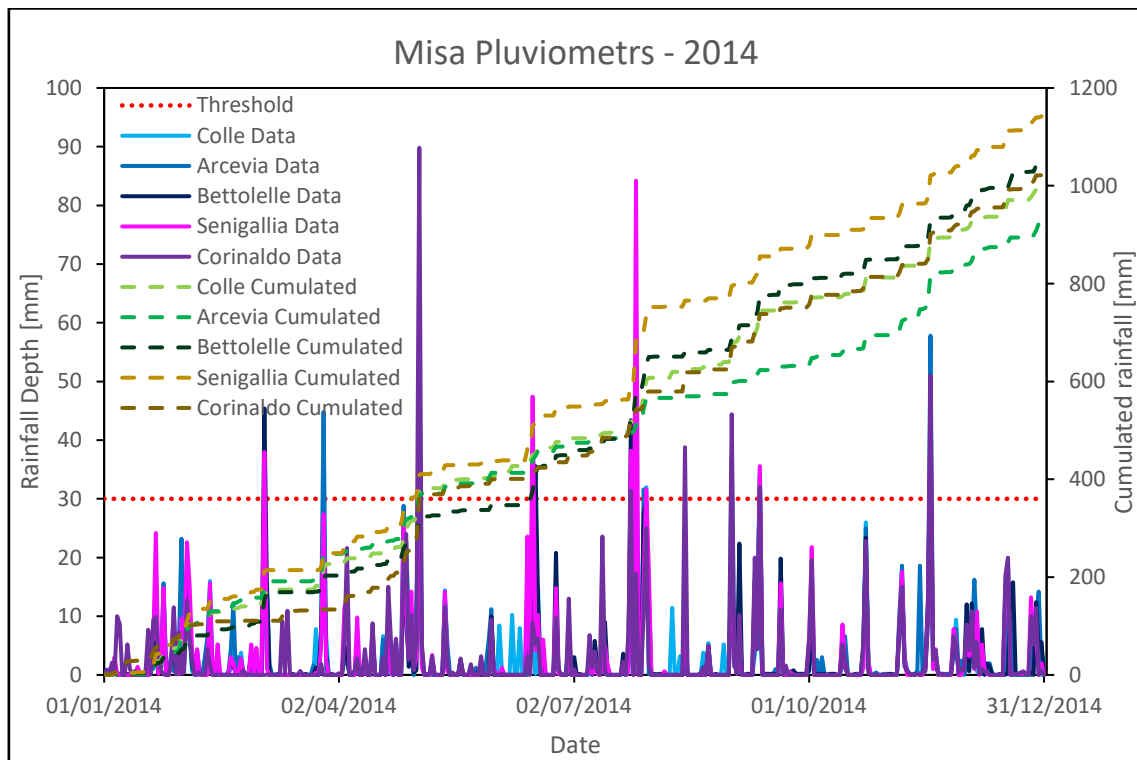


Figure 28: Rainfall data and cumulated rainfall during 2014.



The year 2017 is very similar to 2014 in terms of the distribution of rain events, as they occur in both the first and second half of the year (Figure 29). The difference between the two years analyzed is the amount of rain falling throughout the year, which in 2017 is less as well as the relevant events, which are 4 or 5 depending on the rain gauge considered. On the other hand, the only similarity with 2022 is the presence of a relevant storm event in September 2017 where about 90 mm of rain was recorded in one day in Senigallia. Despite this, the dynamics of the event remain totally different in that significant rainfall was recorded over the entire basin, making it more similar to the 2014 event. Moreover, in this case the event did not lead to flooding.

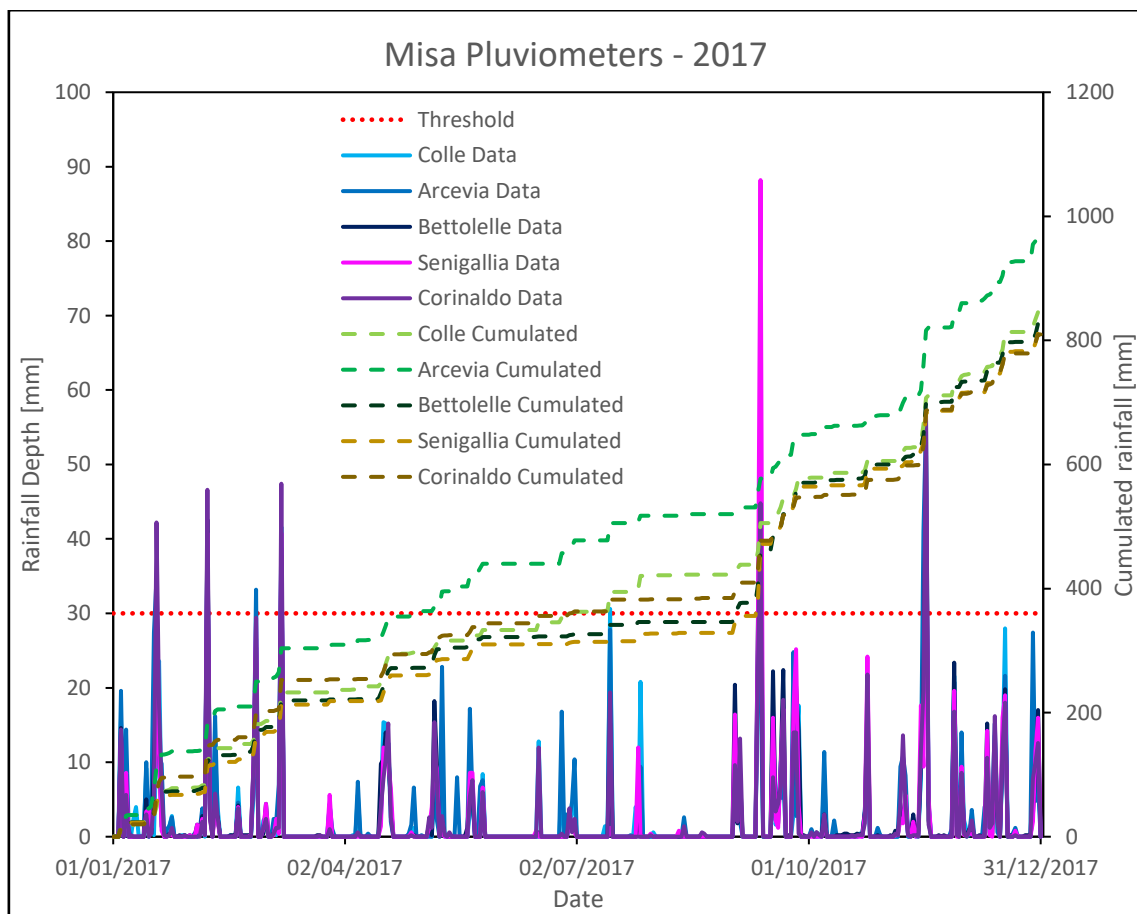


Figure 29: Rainfall data and cumulated rainfall during 2017.

### **4.3 Discharge analysis and comparisons**

After analyzing rainfalls, it is necessary to take into account how they translate into water flow rates within the riverbeds. These flow rates were derived using rating curves considering the water heights measured by the hydrometers, which were obtained from the SIRIMP (“Sistema Informativo Regionale Meteo-Idro-Pluviometrico”) portal. The analysis was conducted by considering the same events and years as the rainfall analysis. The flow rates are not directly measured by fixed instrumentation over the Misa River basin but are derived from flow height data. They are transformed into flow values through a height-flow relationship using correlation stage-discharge. The latter is determined from the characteristics of the riverbed itself and is presented as an exponential function. It is station-specific and also varies over the years, as the conditions of the riverbeds are not static. Data from 3 stations were analyzed:

- Bettollelle,
- Corinaldo,
- Serra de’ Conti.

They are distributed throughout the basin (Figure 30) and provide a general view of the flow rate trends from the higher spring areas to the flatter areas near the outlet. An attempt was also made to analyze the heights of the Ponte Garibaldi station in the center of Senigallia but unfortunately no flow rate scale is available for this. Stage discharge curves for the analyzed stations are in Figures 31, 32, 33 and comparison among the considered events are in Figures 34, 35, 36.

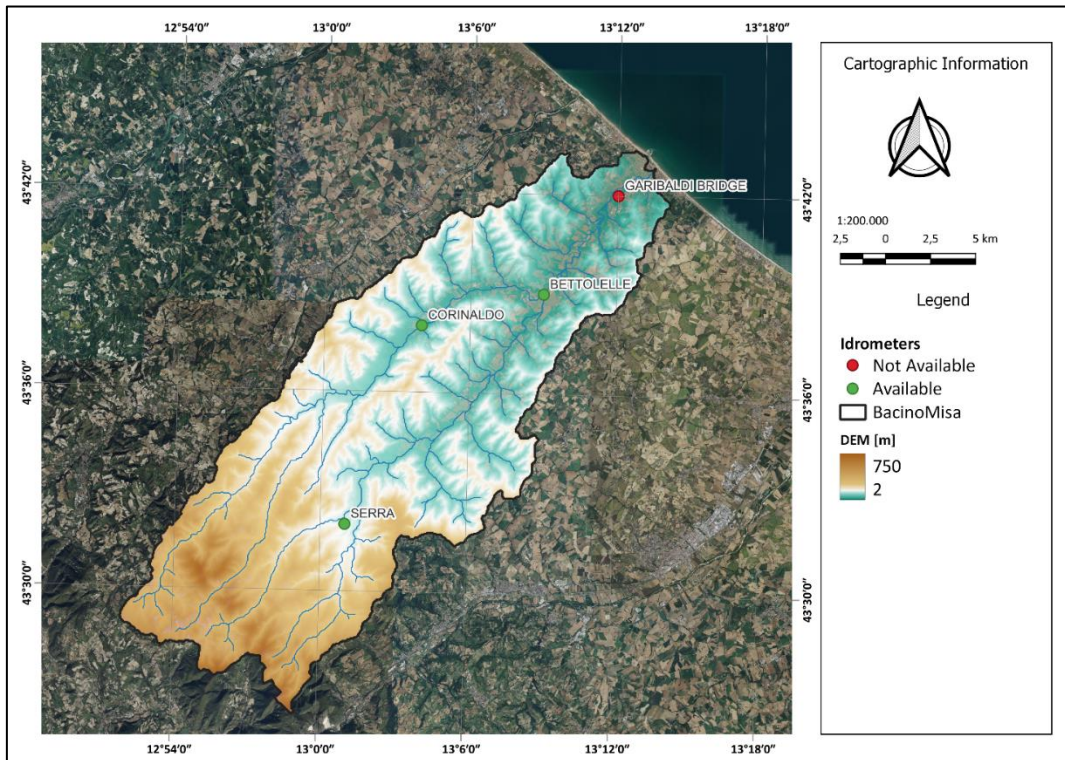


Figure 30: Hydrometers positioning and availability.

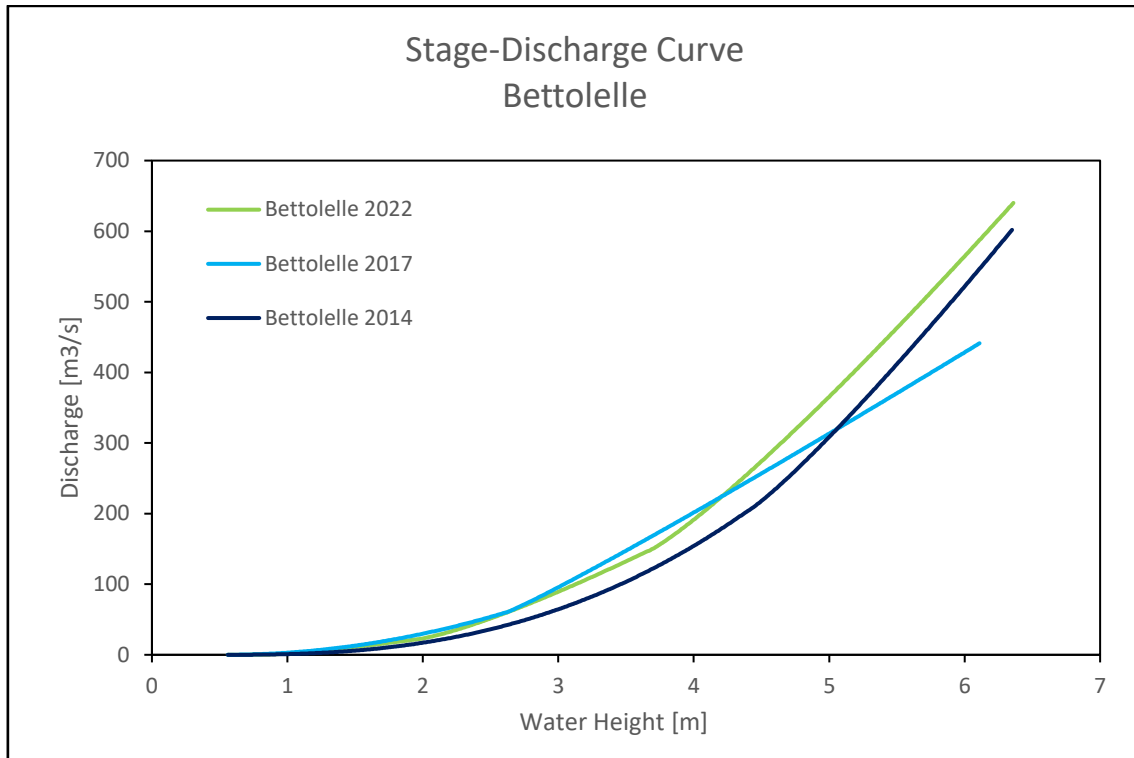


Figure 31: Stage-Discharge Curves Bettollelle.

Bettollelle 2022 (validity from 2019 to 2030):

$$\left\{ \begin{array}{ll} 0.85m \leq h \leq 1.03m; & 2.33 \cdot (h - 0.84)^{0.79} \text{ (Eq. 66)} \\ 1.04m \leq h \leq 2.1m; & 19.68 \cdot (h - 1.03)^{1.24} + 0.6 \text{ (Eq. 67)} \\ 2.11m \leq h \leq 3.8m; & 64.05 \cdot (h - 2.1)^{1.26} + 22.01 \text{ (Eq. 68)} \\ h \geq 3.81m & 155.87 \cdot (h - 3.8)^{1.16} + 146.7 \text{ (Eq. 69)} \end{array} \right.$$

Bettollelle 2017 (validity from 2017 to 2018):

$$\left\{ \begin{array}{ll} 0.95m \leq h \leq 3.02m; & 14.388 \cdot (h - 0.942)^{1.974} \text{ (Eq. 70)} \\ 3.03m \leq h \leq 6.5m; & 100.396 \cdot (h - 3.02)^{1.068} + 60.954 \text{ (Eq. 71)} \end{array} \right.$$

Bettollelle 2014 (validity from 2011 to 2015):

$$\left\{ \begin{array}{ll} 0.55m \leq h \leq 4.39m; & 6.195 \cdot (h - 0.517)^{2.576} \text{ (Eq. 72)} \\ 4.4m \leq h \leq 6.35m; & 185.568 \cdot (h - 4.39)^{1.138} + 202.776 \text{ (Eq. 73)} \end{array} \right.$$

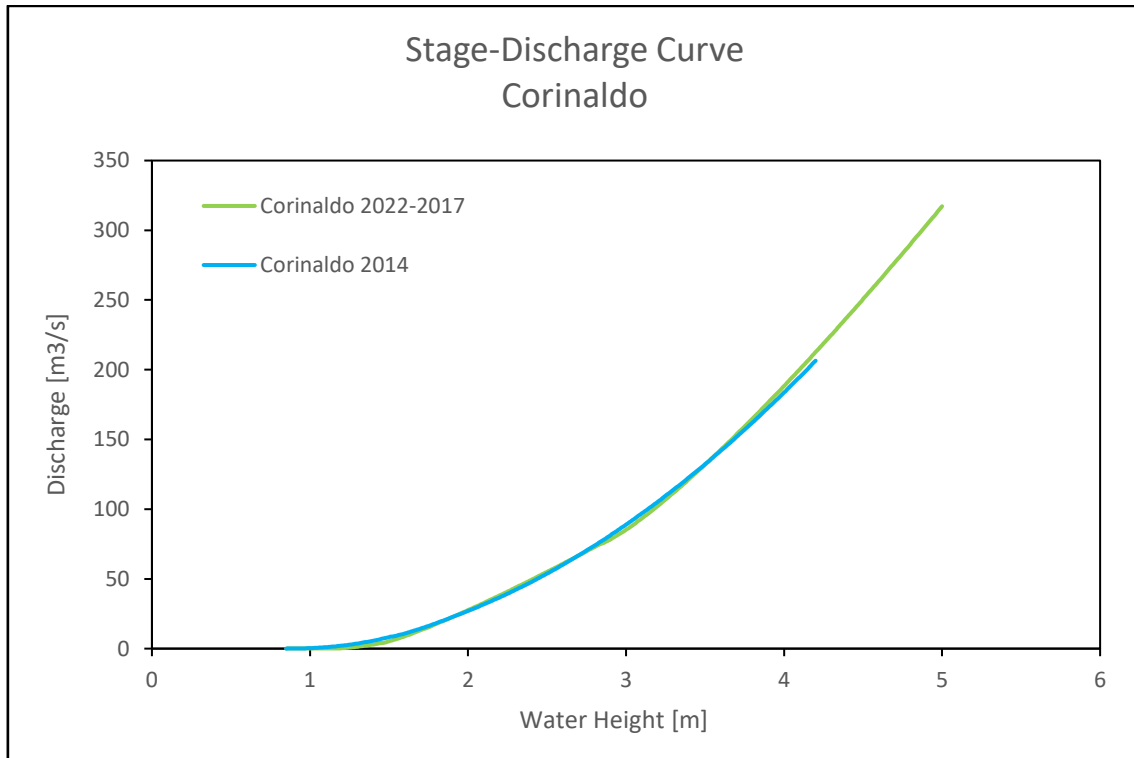


Figure 32: Stage-Discharge Curves Corinaldo.

Corinaldo 2022 and 2017 (validity from 2017 to 2030):

$$\left\{ \begin{array}{ll} 0.85m \leq h \leq 1.2m; & 0.628 \cdot (h - 0.849)^{0.957} \text{ (Eq. 74)} \\ 1.21m \leq h \leq 1.46m; & 22.094 \cdot (h - 1.2)^{1.295} + 0.231 \text{ (Eq. 75)} \\ 1.47m \leq h \leq 2.84m; & 48.606 \cdot (h - 1.46)^{1.18} + 4.091 \text{ (Eq. 76)} \\ h \geq 2.85m & 94.37 \cdot (h - 2.84)^{1.223} + 75.173 \text{ (Eq. 77)} \end{array} \right.$$

Corinaldo 2014 (validity from 2014 to 2015):

$$\left\{ \begin{array}{ll} 0.85m \leq h \leq 1.51m; & 21.041 \cdot (h - 0.837)^{2.28} \text{ (Eq. 78)} \\ 1.52m \leq h \leq 1.99m; & 44.368 \cdot (h - 1.51)^{1.223} + 8.528 \text{ (Eq. 79)} \\ 2m \leq h \leq 4.2m; & 20.76 \cdot (h - 0.85)^{1.9} \text{ (Eq. 80)} \end{array} \right.$$

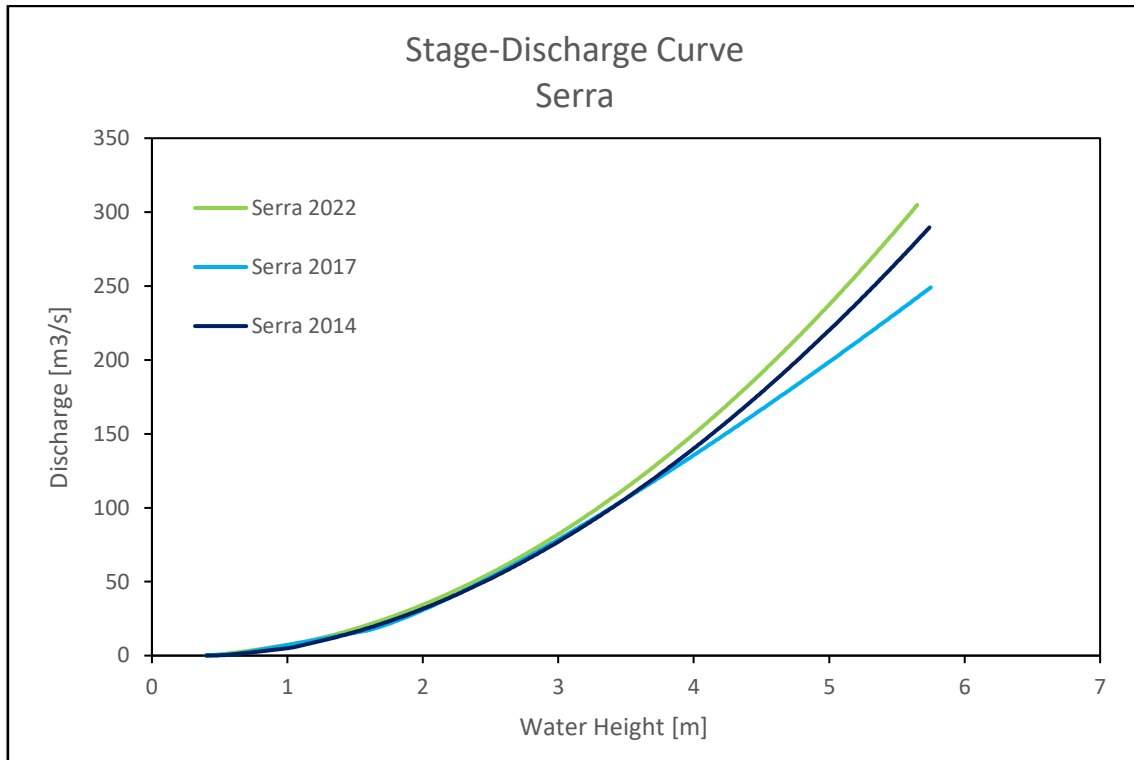


Figure 33: Stage-Discharge Curves Serra.

Serra 2022 (validity from 2022 to 2050):

$$\begin{cases} 0.55m \leq h \leq 4.39m; & 6.195 \cdot (h - 0.517)^{2.576} \text{ (Eq. 81)} \\ 4.4m \leq h \leq 6.35m; & 185.568 \cdot (h - 4.39)^{1.138} + 202.776 \text{ (Eq. 82)} \end{cases}$$

Serra 2017 (validity from 2015 to 2022):

$$\begin{cases} 0m \leq h \leq 0.64m; & 2.808 \cdot (h + 0.257)^{5.841} \text{ (Eq. 83)} \\ 0.65m \leq h \leq 1.56m; & 16.399 \cdot (h - 0.64)^{1.04} + 1.492 \text{ (Eq. 84)} \\ 2m \leq h \leq 4.2m; & 39.456 \cdot (h - 1.56)^{1.238} + 16.53 \text{ (Eq. 85)} \end{cases}$$

Serra 2014 (validity from 2014 to 2015):

$$\begin{cases} 0.41m \leq h \leq 0.53m; & 11.829 \cdot (h - 0.381)^{1.994} \text{ (Eq. 86)} \\ 0.54m \leq h \leq 1.01m; & 10.996 \cdot (h - 0.53)^{1.151} + 0.266 \text{ (Eq. 87)} \\ 1.02m \leq h \leq 1.22m; & 25.767 \cdot (h - 1.01)^{1.1693} + 4.992 \text{ (Eq. 88)} \\ h \geq 1.23m & 12.97 \cdot (h - 0.39)^{1.85} \text{ (Eq. 89)} \end{cases}$$

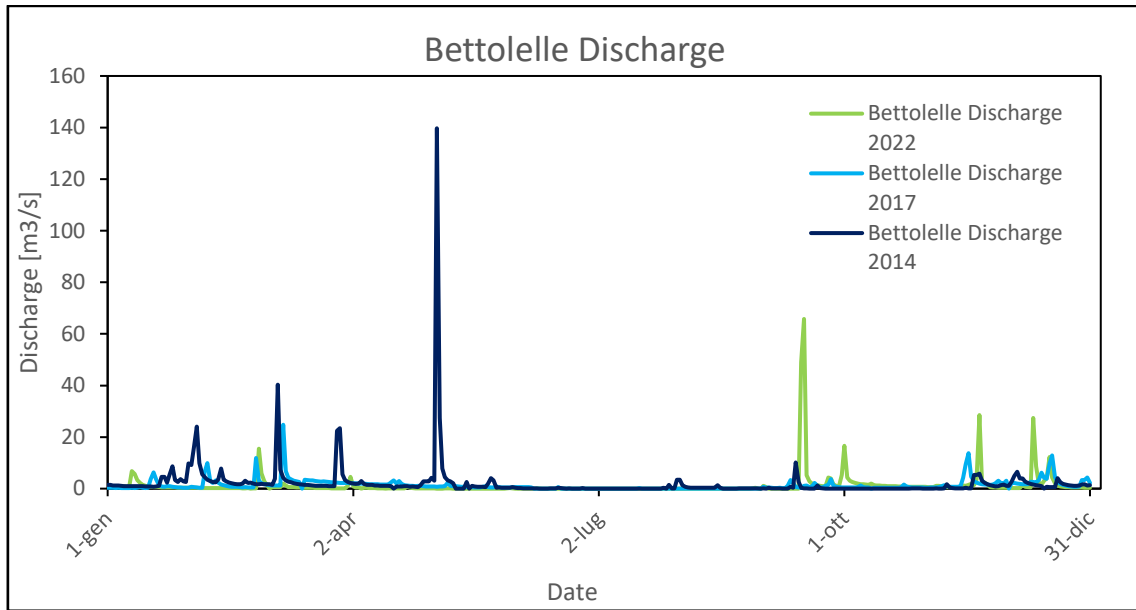


Figure 34: Discharge comparison for Bettollele station.

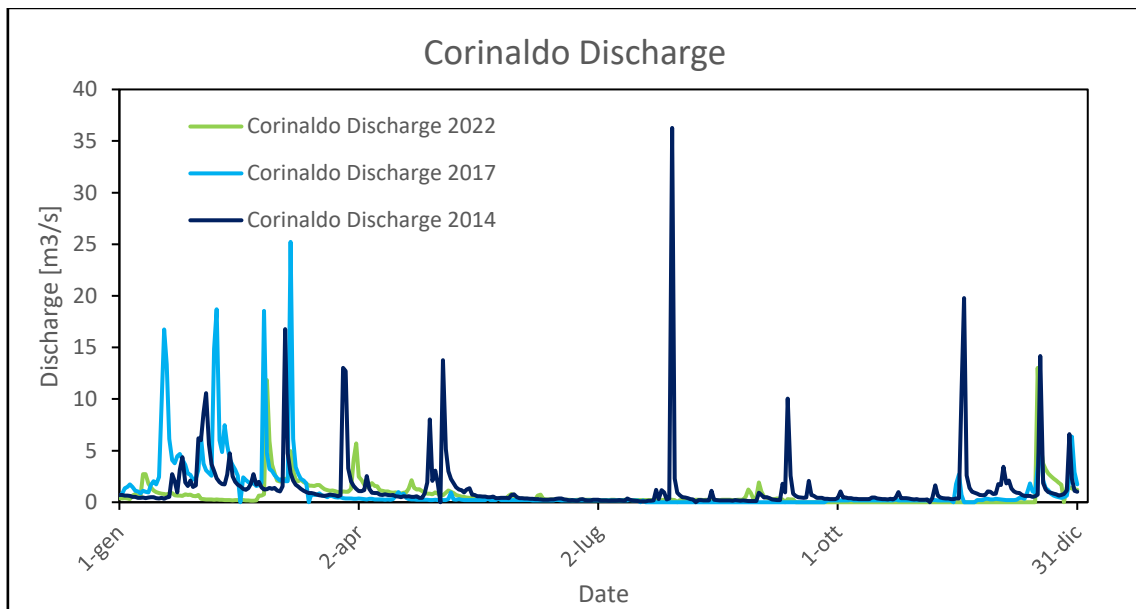


Figure 35: Discharge comparison for Corinaldo station.

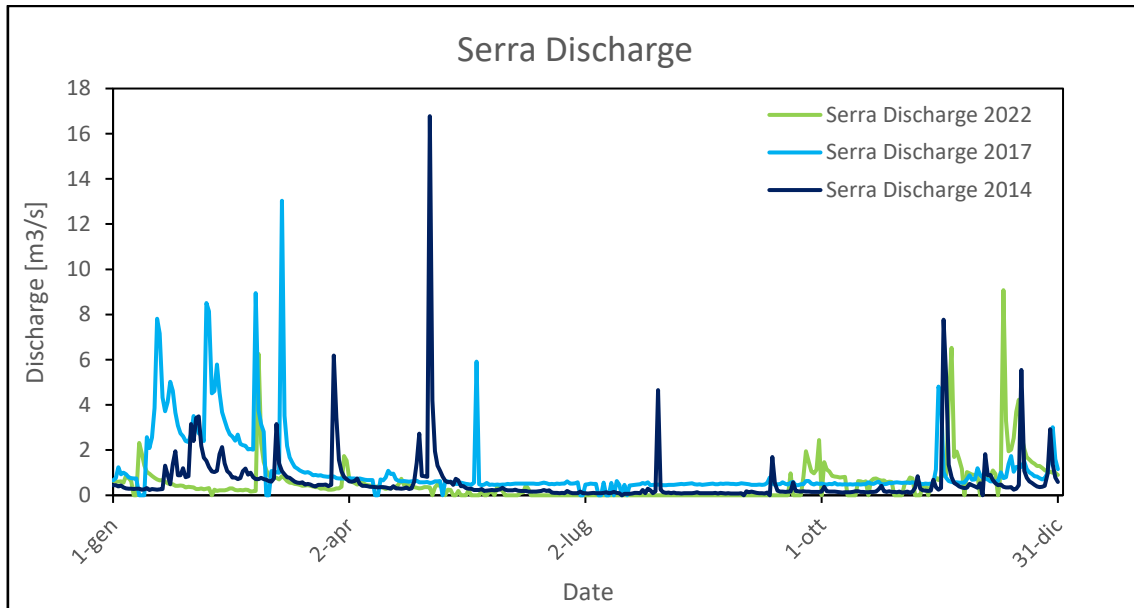


Figure 36: Discharge comparison for Serra station.

The annual flow rates are shown in the graphs (Figures 34, 35, 36) above. Note that the 2017 stage-discharge curve of the Bettolle station was used also for the year 2014, because the one estimated for 2014 produced results that were totally incompatible with the average flow measurements recorded in the Misa basin. In fact, the flow rates obtained were too high and resulted in an average annual value of about  $5 \text{ m}^3/\text{s}$ , which is far from the average value of  $2 \text{ m}^3/\text{s}$  that is normally recorded in Senigallia. The peaks produced by the flood events of the years 2022 and 2014 are immediately noticeable, even if in the latter the peak is higher. This is mainly due to the nature of the event itself that lasted much longer compared to the 2022 event, which lasted only a few hours. In addition, the flood peak developed in the morning, causing a significant increase in the average flow rate over the course of the day. On the other hand, the 2022 event was characterized by a higher intensity, but the flood peak was reached during the night of September 15<sup>th</sup> after a period of severe drought. This significantly affected the average flow rate. In fact, the highest flows occurred between the night of the 15<sup>th</sup> and the morning of the 16<sup>th</sup>, resulting in average flows that were not as significant. It is also observed that there are no peak recordings available for Corinaldo and Serra de' Conti since the sensors stopped working when the flood wave passed through. In contrast, during the 2014 event, all sensors recorded values correctly. The graphs displaying the flood wave peaks are shown below, in Figures 37 and 38.



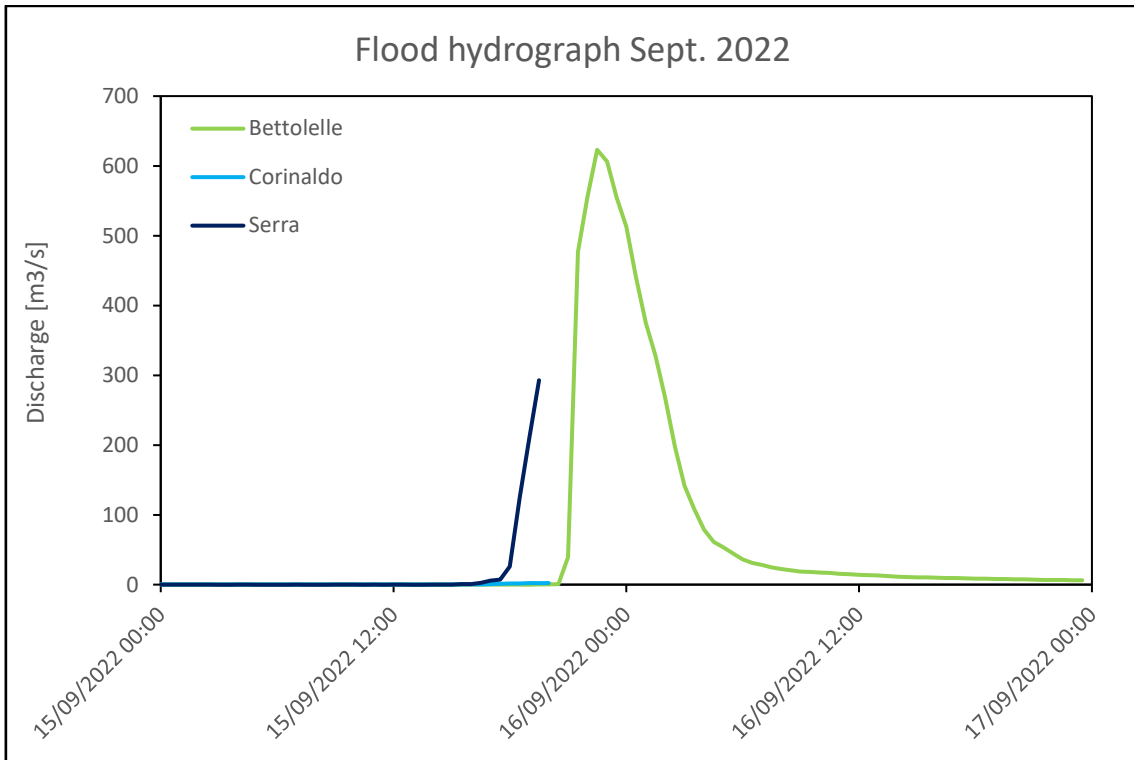


Figure 37: Peak flow of flood event of Sept. 2022 for the 3 stations.

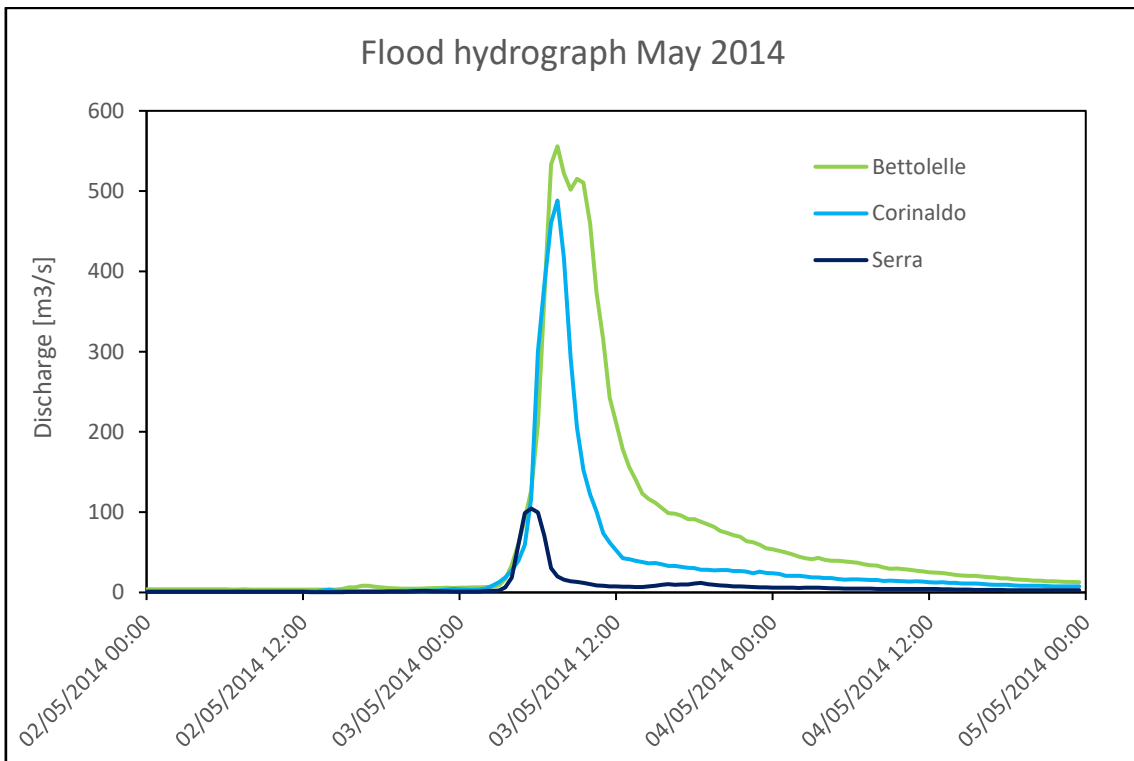


Figure 38: Peak flow of flood event of Sept. 2022 for the 3 stations.

## 5. SWAT analysis

### 5.1 Simulation setup

QSWAT is the SWAT+ operating interface that allows the setup of the basin using QGIS. This interface can be installed as a plugin directly from QGIS itself. QSWAT is supported from QGIS3 version onwards. The interface is divided into 3 main steps:

- definition of the morphology of the basin
- definition of the hydrologic response unit (HRU)
- definition of atmospheric conditions and analysis period.

In the first section, the map is defined in sequence with the elevations of the basin (DEM), the position of streams and channels and the sub-basins, which will define which parts of the basin will drain into which parts of reaches. By specifically analyzing the creation of streams and channels, QSWAT exploits the potential of the *TauDEM* (Terrain Analysis Using Digital Elevation Models) suite of tools (83). It automatically executes a series of commands to define how the water will move inside the basin. The commands are in sequence:

*PitRemove, D8FlowDir, DInfFlowDir, Area D8, AreaDinf, GridNet, Threshold, and StreamNet.*

Note the use of *D8*, which represents the number of MPI (Message Passing Interface) processes to use, which in this case is 8. It will also be the number of subareas into which the domain will be divided and consequently the number of processes parallel MPI used to process each of the individual subareas.

After defining the stream network, it can be moved on to defining the inflow and outflow points, which have been manually determined. The last step consists in determining the boundaries of the sub-basins, which uses part of the tools to produce them (Figure 39).

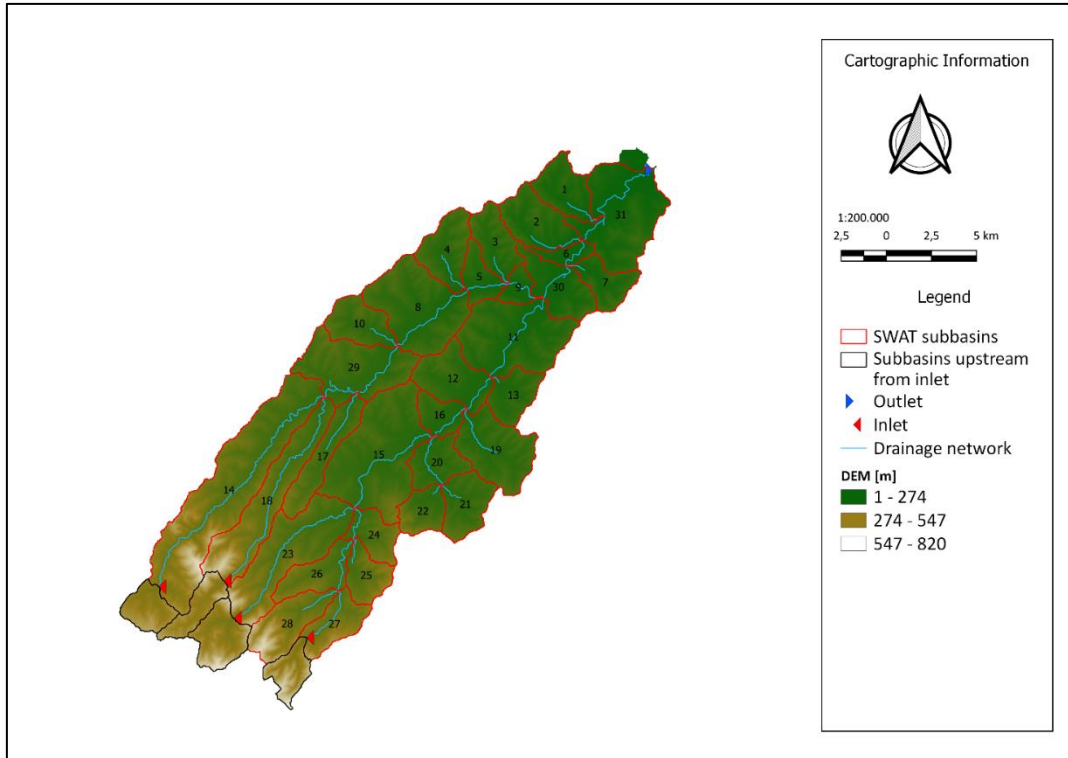


Figure 39: SWAT subbasins subdivisions of Misa Basin.

The second step that the QSWAT interface presents is the definition of the HRU. SWAT+ uses the Hydrogeological Response Units as a subdivision of the landscape units (LSU). Each of these is determined on a particular combination of land use, soil and slope range (Figure 40).

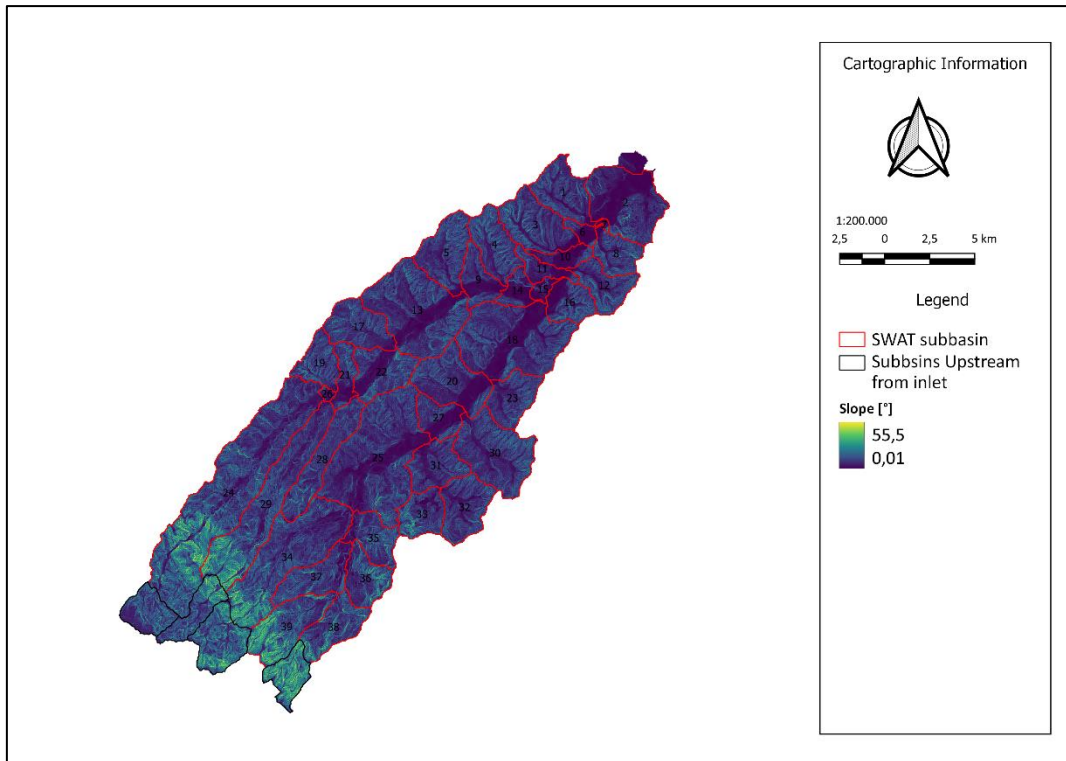


Figure 40: SWAT slope map.

These three parameters are in fact crucial in the erosion phenomenon as the chemical-geological characteristics and exposure to atmospheric agents determine the overall erosion behavior (84). For this reason, soil and land use maps are defined. The former (Figure 41) is obtained through Food and Agricultural Organization (FAO) data, which define classes of based on the specific composition of soil components. Each soil unit is defined by a numerical code, which in turn is composed of multiple soil types, which are defined by an alphabetical code (Table 4). These are defined by a specific grain composition and are defined by the percentage present within the soil unit. The Table 5 also shows the textural class and topography of the specific soil (85).

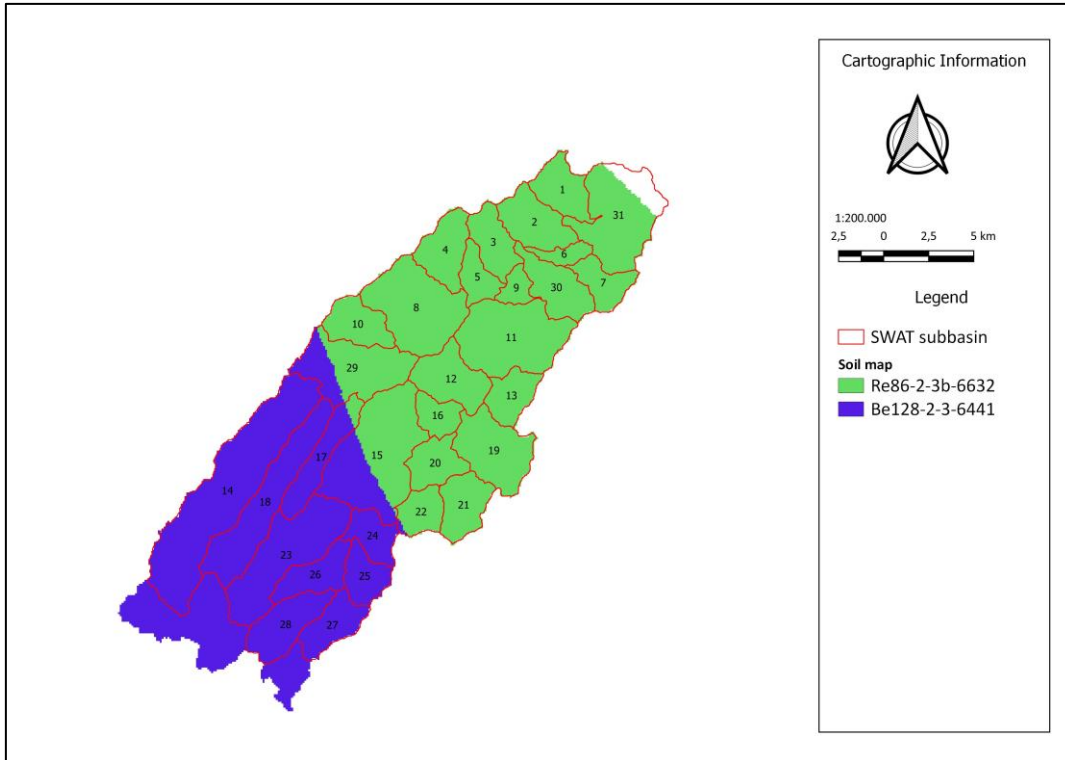


Figure 41: SWAT soil map.

Soil Mapping Unit Number	Soil Mapping Unit Symbol	Dominant Soil Unit	% of dominant soil unit	Composition of soil unit 1 (% that belongs to texture-slope class)									
				1a	1b	1c	2a	2b	2c	3a	3b	3c	4d
6441	Be128-2/3bc	Be	40	0	0	0	0	10	10	0	10	10	0
6632	Re86-2/3b	Re	50	0	0	0	0	25	0	0	25	0	0

First associated soil unit	% of first associated soil unit	Composition of soil unit 2 (% that belongs to texture-slope class)								
		1a	1b	1c	2a	2b	2c	3a	3b	3c
E	20	0	0	0	0	20	0	0	0	0
Be	20	0	0	0	0	20	0	0	0	0
Second associated soil unit	% of second associated soil unit	Composition of soil unit 3 (% that belongs to texture-slope class)								
		1a	1b	1c	2a	2b	2c	3a	3b	3c
Lo	20	0	0	0	10	10	0	0	0	0
Vc	20	0	0	0	0	0	0	20	0	0
Third associated soil unit	% of third associated soil unit	Composition of soil unit 4 (% that belongs to texture-slope class)								
		1a	1b	1c	2a	2b	2c	3a	3b	3c
I	10	0	0	0	0	5	5	0	0	0
Je	10	0	0	0	10	0	0	0	0	0
Fourth associated soil unit	% of fourth associated soil unit	Composition of soil unit 5 (% that belongs to texture-slope class)								
		1a	1b	1c	2a	2b	2c	3a	3b	3c
Rc	10	0	0	0	0	10	0	0	0	0
	0	0	0	0	0	0	0	0	0	0

Table 4: Description and composition of the used soil.

Textural Class	Meaning	Topography Class	Slope [%]
1	Coarse	a	0-8 (gently undulating)
2	Medium	b	8-30 (rolling to hilly)
3	Fine	c	>30 (mountainous relief)

Table 5: Textural and topographic classes of soils.

Since the available land use maps vary and differ in terms of resolution and ground truth interpretation, a sensitivity preliminary analysis on this parameter was conducted. Three different maps have been selected. They are based on SWAT codes that specify the type of land use.

The used codes are defined in Table 6:

Codes	Land Covers
AGRL	Agriculture generic
URML	Medium-low density residential
RNGE	Grassland/Herbaceous
RNGB	Range Shrubland
FRSD	Deciduous Forest
FRSE	Evergreen Forest
MIGS	Mixed shrubland/grassland
CRDY	Dryland and cropland pasture
FODB	Deciduous broad-leaf forest
CRWO	Mosaic cropland/woodland

*Table 6: Codes of the considered land use.*

The first is obtained by processing the CORINE map (Figure 42) from the geoportal of the Marche region.

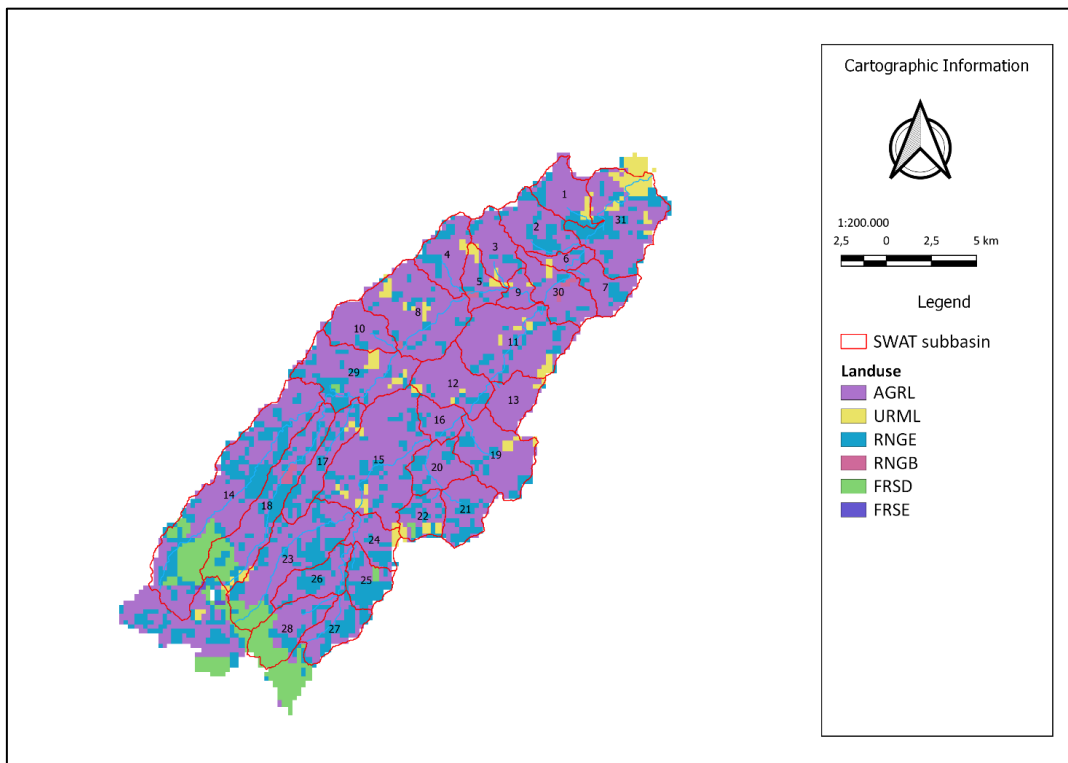


Figure 42: CORINE land use of Misa basin.



The second is obtained directly from the SWAT+ website, which provides data for all continents. The service relies on the USGS EROS Archive - Land Cover Products - Global Land Cover Characterization (GLCC) portal (Figure 43).

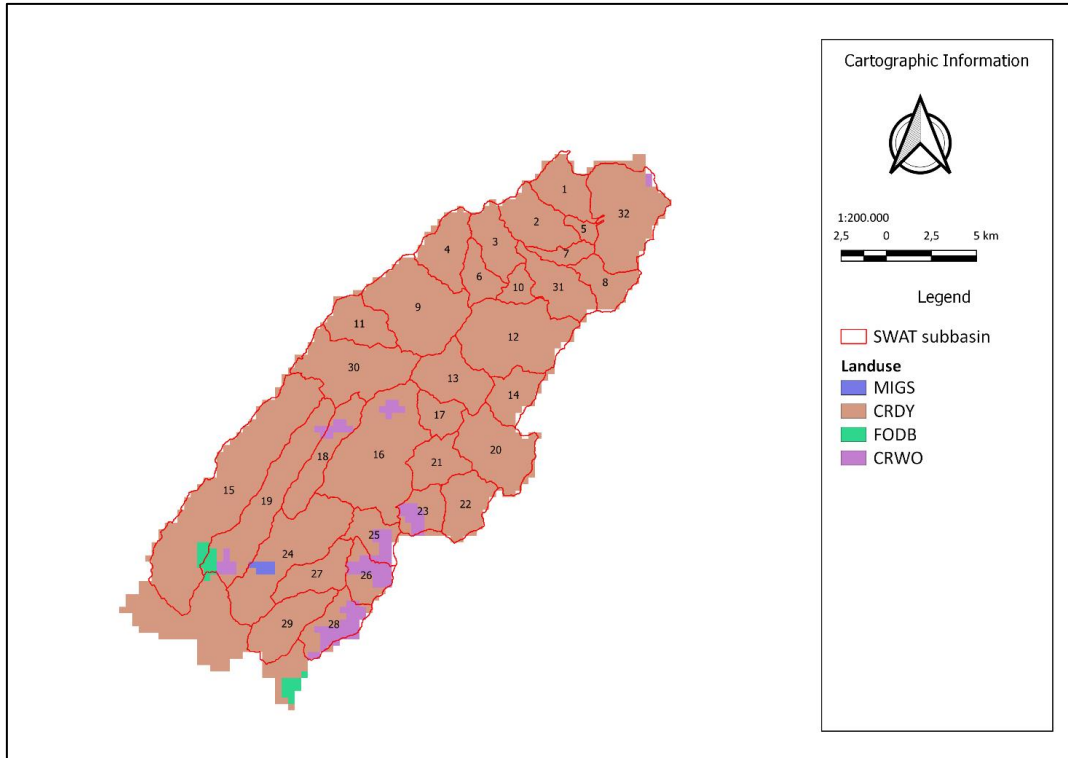


Figure 43: GLCC portal land use of Misa Basin.

The third instead was defined by hand sampling a satellite image obtained by EO browser using the Sentinel 2A (86), from the Copernicus Program (Figure 44). This satellite is part of a constellation made up of two devices, 2A and 2B, in orbit respectively since 2015 and 2017, whose mission is Earth observation. Both are equipped with a MultiSpectral Instrument (MSI) that measures the earth's reflectance with 13 bands, from visible/NearInfrared VNIR to Short Wave Infrared spectral range SWIR. The band chosen for the satellite image comes from the visible spectrum and has a ground resolution of 10 meters.

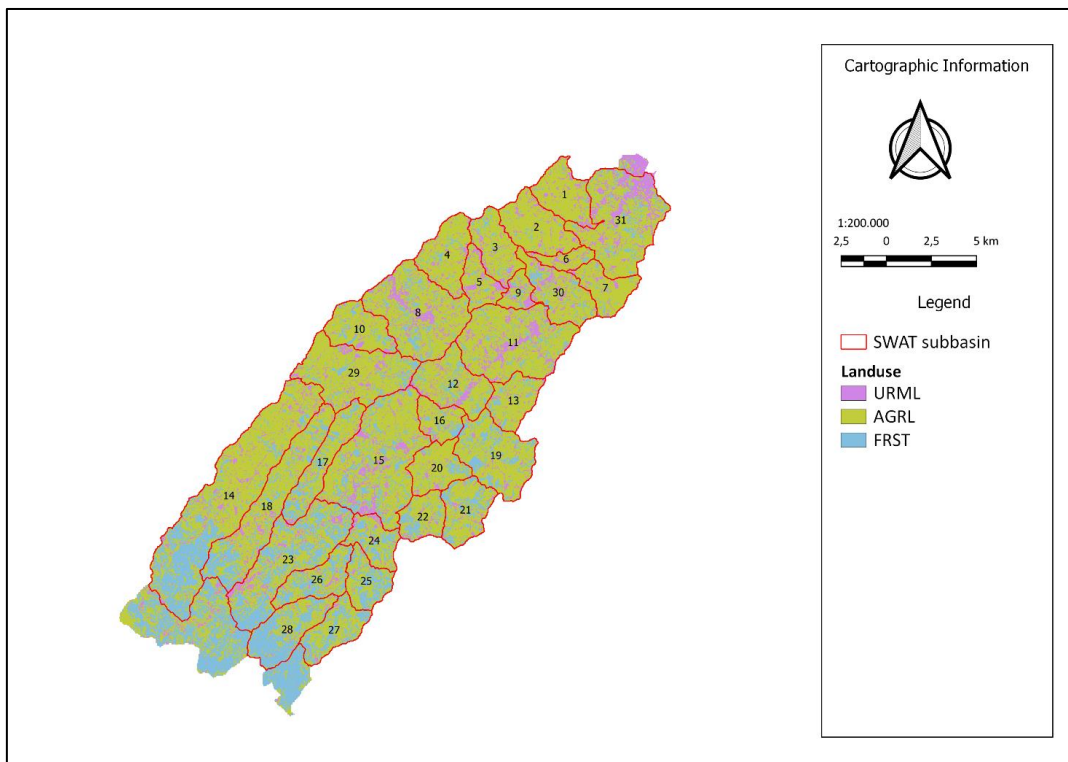


Figure 44: Supervised classification land use of Misa Basin.

Results from this sensitivity analysis are in the next section.

Then, HRUs were defined according to specific criteria of the software. QSWAT offers two options:

- single HRU in which the result will be one in which the HRU is given the land use with the largest surface area in the entire LSU (same for soil and slope range)
- multiple HRU through which it is possible to reduce the number of HRUs through filters that impose thresholds on the values (by percentage or by area) of land use, soil, and slope range. HRU below these thresholds will be eliminated and redistributed proportionally among those with greater surface area.

For analyzing the Misa Basin, it was decided to use the second option, because by imposing the land use with larger area in each HRU, it was noticed that the agricultural component of the land use was imposed with too high a percentage (Figure 45). In order to maintain as accurate a description as possible, it was decided to impose a multiple HRU that maintains an accurate description of the basin. In fact, it imposed the elimination of all those HRUs with a percentage of less than 1% (lower admissible value) on the area of the respective LSU.

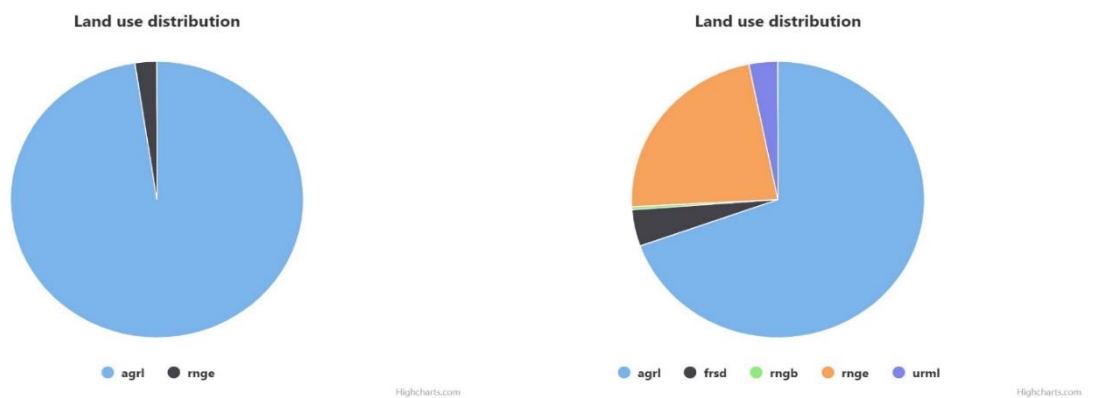


Figure 45: Land use distribution comparison between single and multiple HRU.

The last step required by the QSWAT interface is to enter the global weather generator database. It contains monthly atmospheric statistical data from points located all over the globe. In addition to the definition of the weather generator, the meteorological observations obtained through stations must also be defined. The data that must be provided include the daily rainfall value and the coordinate of the corresponding weather station. For all the periods analyzed, the same rain gauges were used, and their data are derived from the Civil Protection website through the SIRIMP (“Sistema Informativo Regionale Meteo-Idro-Pluviometrico”) system. The data are recorded every 15 minutes and were processed in order to obtain the daily rainfall amounts. The locations of the rain gauges are shown in Figure 24. In addition to the rainfall data, the temperature, humidity, and wind values can also be defined. If they are not defined, they will be derived from the values contained in the weather generator database. The stations used to obtain the rain data are five and contain the daily rainfall data ranging from 1<sup>st</sup> January 2013 to 31<sup>st</sup> December 2022. In order to model a situation as close to reality as possible, a warm-up year (2013) was imposed, which allows to start printing results from a situation that is not perfectly dry soil, and results were printed for all years, from 2014 to 2022. The choice was made because SWAT simulations focused both on the critical events of 2022 and 2014, and to a typical non-inundation year (2017) for comparison. The simulations of 2022 and 2014 were conducted for the single events and for the entire year, while year 2017 simulation was only annual. In addition, three different time steps were chosen that would model rainfall from the daily data. They are daily time step, 15-minute time step, and 1-minute time step. They will be discussed for specific cases but in general, the former is best suited for outputs greater than 30 days while the latter two better approximate periods of a few days.

## 5.2 Preliminary analysis: land use maps sensitivity

Before proceeding with the definition and the analysis of flood scenarios, the three different maps containing land use data (Figures 42, 43 ,44) were tested by doing the hydrogeological simulation of the Misa basin throughout the year of 2022. In particular, the annual average values of outflow discharge and sediment production were defined. This operation is interesting for the evaluation of the results discrepancy obtainable from different input sources. The values obtained were then transposed to the maps and compared. In order to obtain the precise value at the station the selection feature of QGIS is used to highlight the numerical value inside the attribute table of the output.

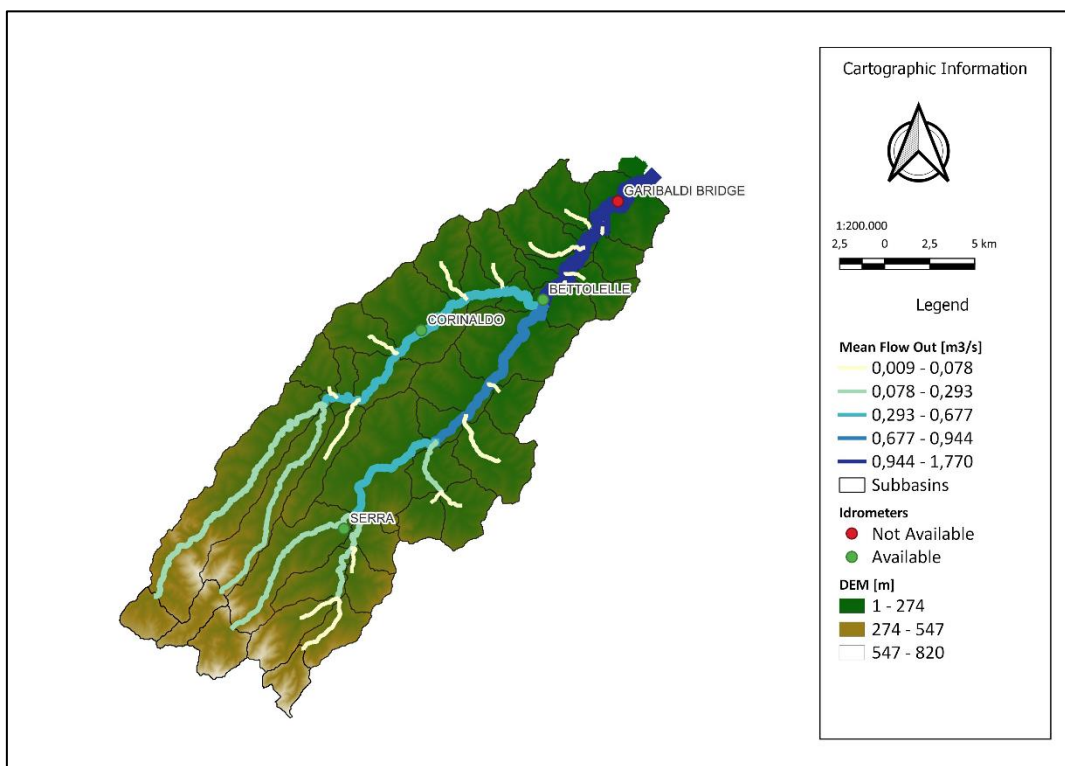


Figure 46: Mean flow out of Misa Basin in 2022 with Corine land use.

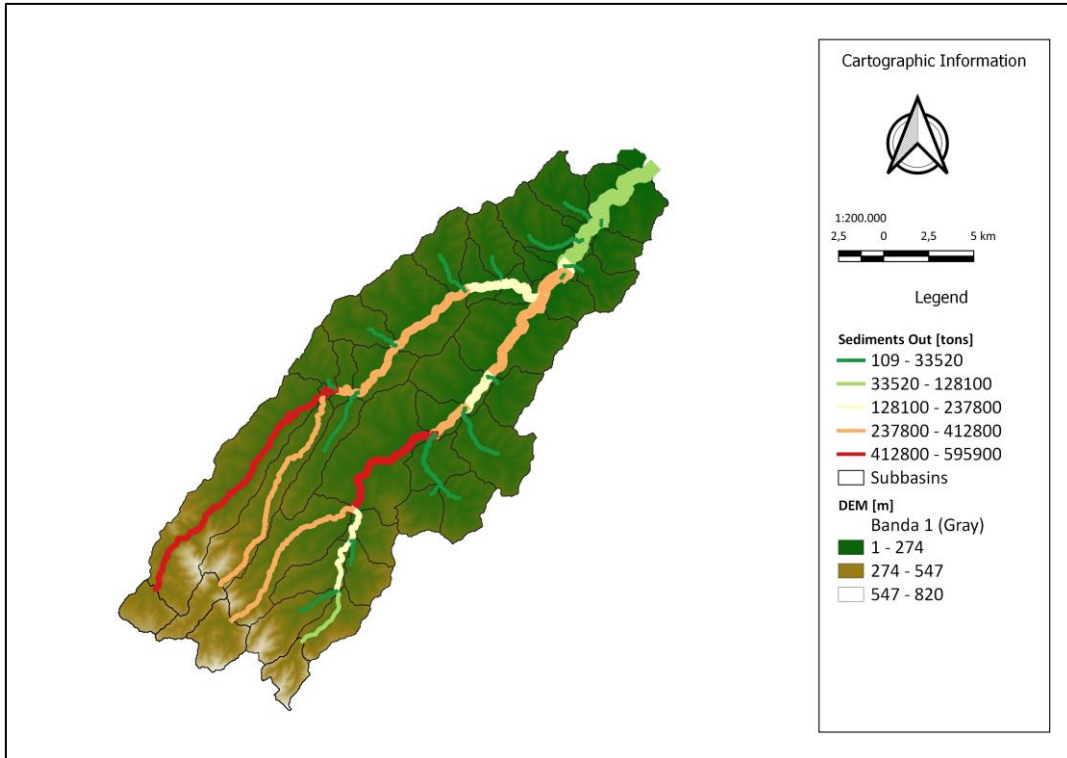


Figure 47: Mean sediments out of Misa Basin in 2022 with Corine land use.

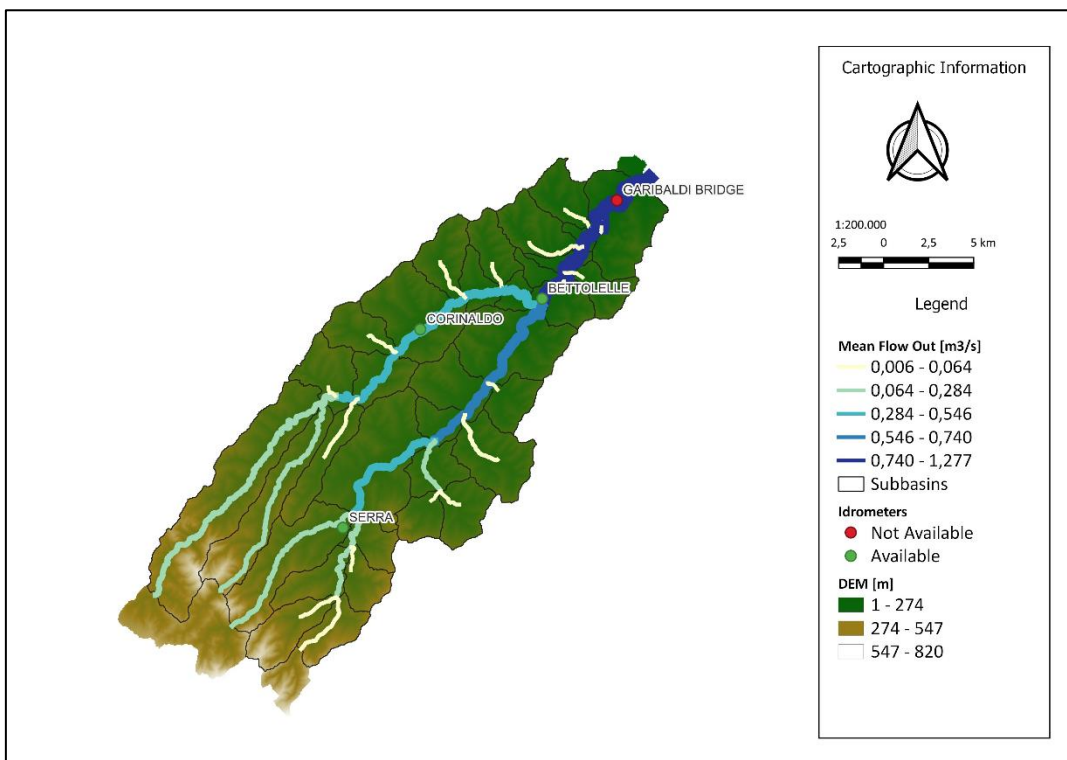


Figure 48: Mean flow out of Misa Basin in 2022 with GLCC portal land use.

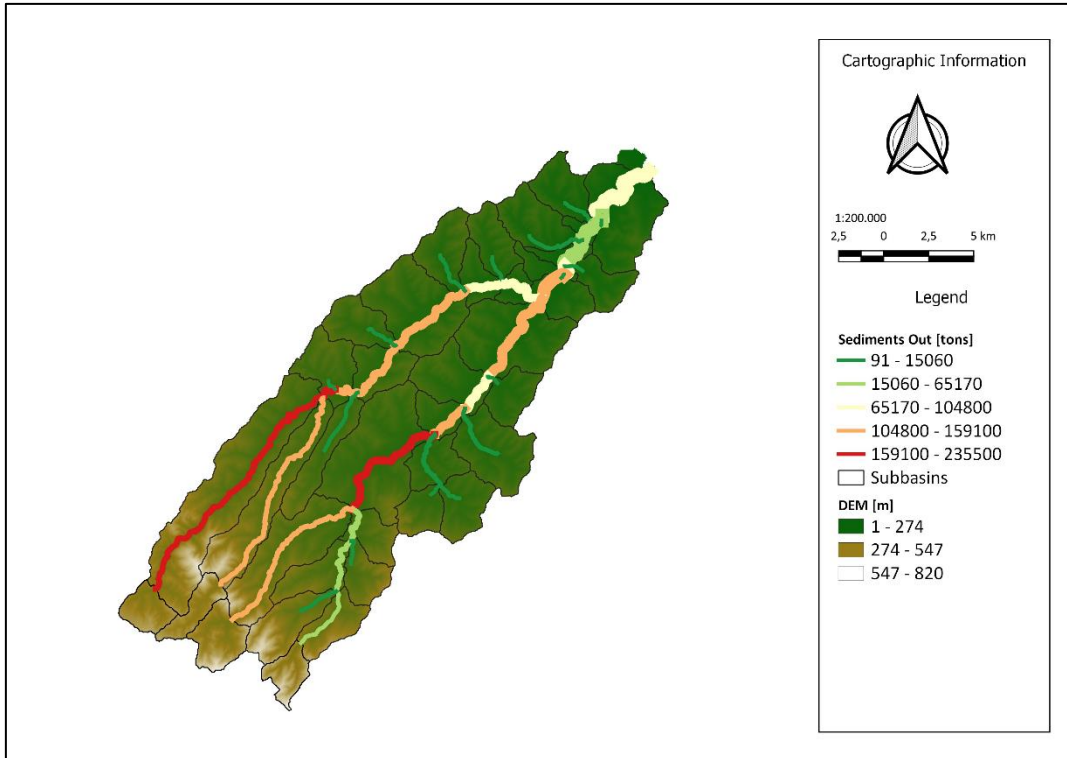


Figure 49: Mean sediments out of Misa Basin in 2022 with GLCC portal land use.

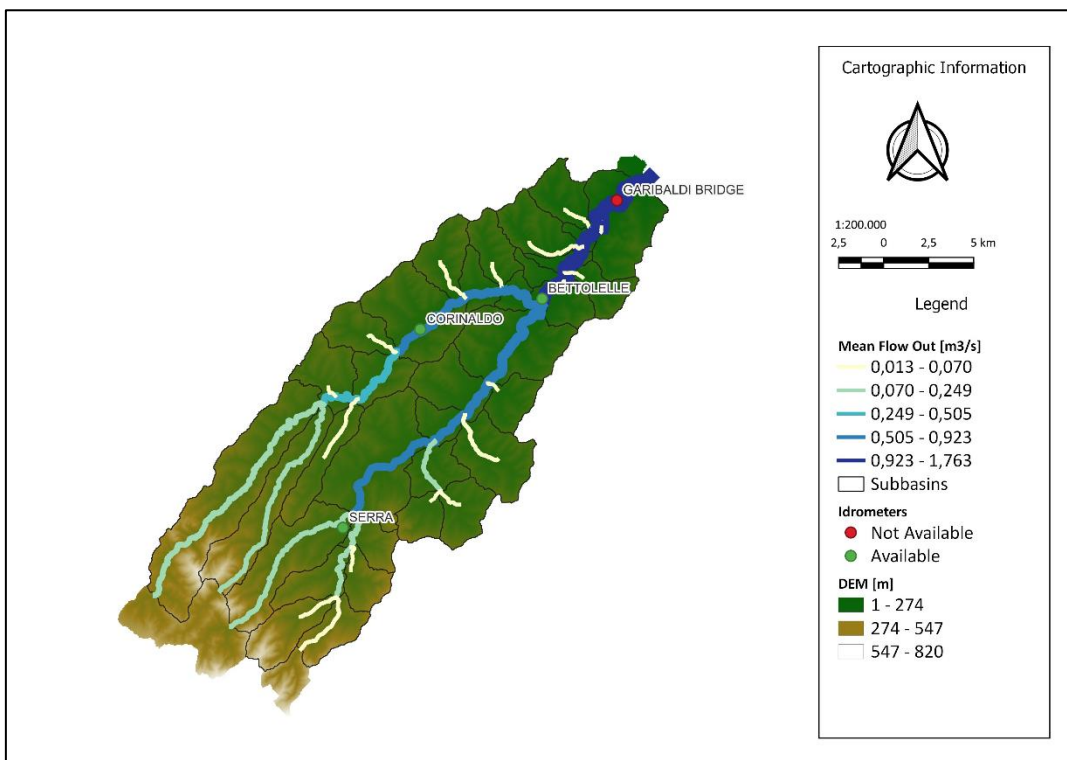


Figure 50: Mean flow out of Misa Basin in 2022 with auto sampling land use.

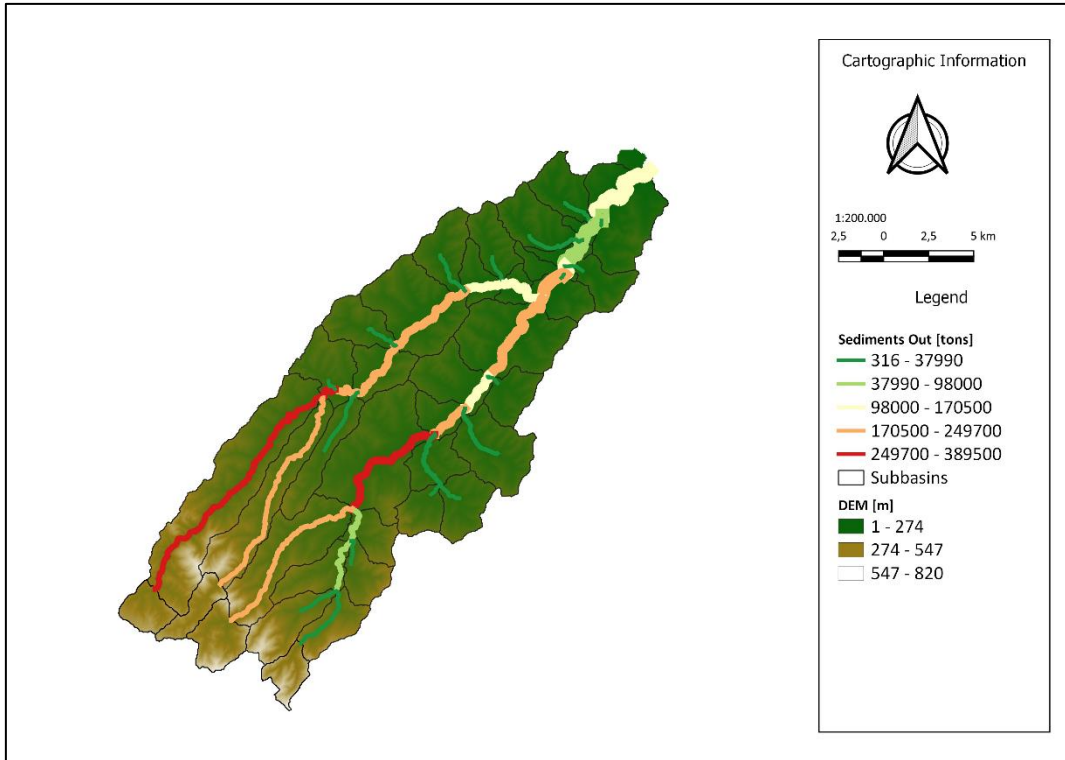


Figure 51: Mean sediments out of Misa Basin in 2022 with auto sampling of landuse.

The preliminary analysis conducted yielded interesting results, in which a discrepancy is immediately evident, particularly in those of average annual flow rate. They can also be validated as mean flow values at 3 localized points throughout the basin. They cover the main parts of the basin, in particular providing information about the mountainous areas with the Serra de' Conti station, the central hilly areas with the Corinaldo station, and the flat areas near the outlet with Bettollelle. SWAT results are thus compared and validated in the Table 7:

Stations	Mean Flow Out [m <sup>3</sup> /s] - 2022				Relative Errors [%]		
	Observed	CORINE land use	GLCC land use	Sampled land use	CORINE land use	GLCC land use	Sampled land use
Bettollelle	1.18	1.39	1.2	1.59	16%	2%	30%
Corinaldo	0.69	0.62	0.44	0.59	-11%	-44%	-16%
Serra	0.51	0.58	0.55	0.63	13%	8%	21%

Table 7: Comparison and relative errors of the 3 land use maps respect to observed values.



The results obtained through the land use derived from the GLCC are good for the Bettolle and Serra de' Conti station, but they are poor for the Corinaldo station as there is a discrepancy of 44%. On the other hand, the maximum error considering the land use from satellite image sampling, is lower even though the results of the 3 stations are all affected by errors greater than 15%. Finally, CORINE land cover gave distributed small errors. Therefore, it was decided to consider the land use of the CORINE map for the subsequent analysis. This choice was also made for the following reasons:

- it provides a more accurate description of the classes,
- it gives smaller relative errors than the one sampled,
- it does not require the use of high-resolution satellite imagery,
- it requires less processing.

For the geologic part, the eroded volumes obtained from SWAT simulations are not a single value, as in semi-empirical models (USLE, RUSLE, etc), but they are referred to the different river reaches. The observation that can be made is that the orders of magnitude of the volumes remain constant among all the basins, typically in the range of hundreds of thousands of tons, and they exhibit similar distributions since the most and least exposed areas are consistent in all three cases.

### 5.3 Results

A numerical assessment of the main hydraulic and geological parameters affecting the Misa basin, at the channel level was obtained using SWAT from geomorphological data, land use and soil data, and precipitation data. The organization of the results is different for the flood event and for the annual simulation (Tables 8, 9). In the first case, both the average flow out and the peak flow discharge are reported, while in the second only the average flow out, because the average annual parameters were considered as input. As regards the geologic component, sediments out, suspended load, bed erosion and bank erosion are reported:

Flooded event outputs	
Hydraulic results	Geologic results
Average flow out [m <sup>3</sup> /s]	Sediments out [tons]
Peak flow discharge [m <sup>3</sup> /s]	Suspended load [tons]
	Bed erosion [tons]
	Bank erosion [tons]

Table 8: Outputs for Flood Events.

Annual outputs	
Hydraulic results	Geologic results
Average flow out [m <sup>3</sup> /s]	Sediments out [tons]
	Suspended load [tons]
	Bed erosion [tons]
	Bank erosion [tons]

Table 9: Outputs for Annual Analyses.

### 5.3.1 Hydraulic results (2022, 2014, 2017)

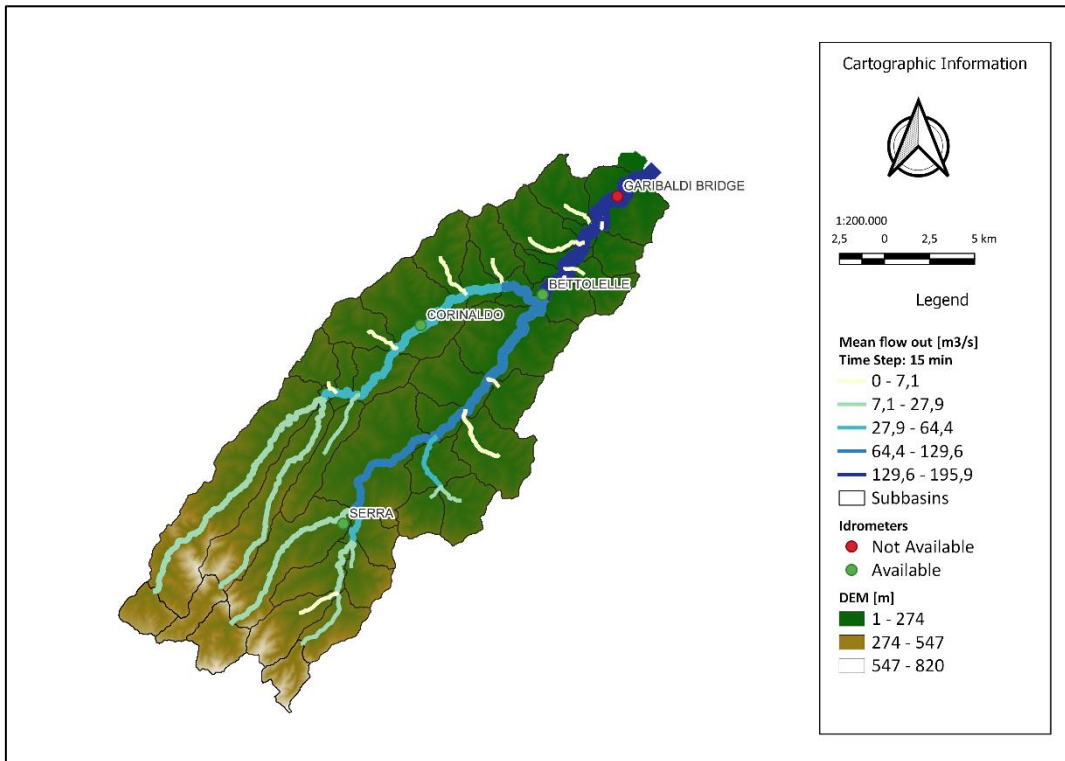


Figure 52: Average flow out during flood event in September 2022.

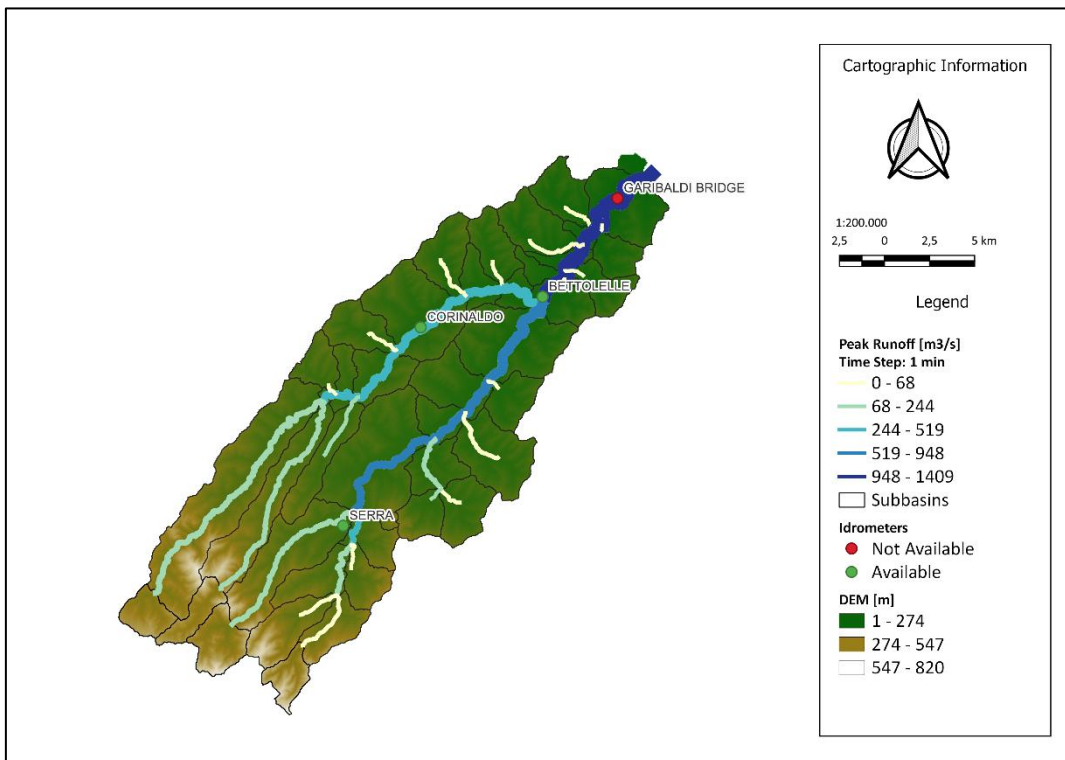


Figure 53: Peak runoff during flood event in September 2022.

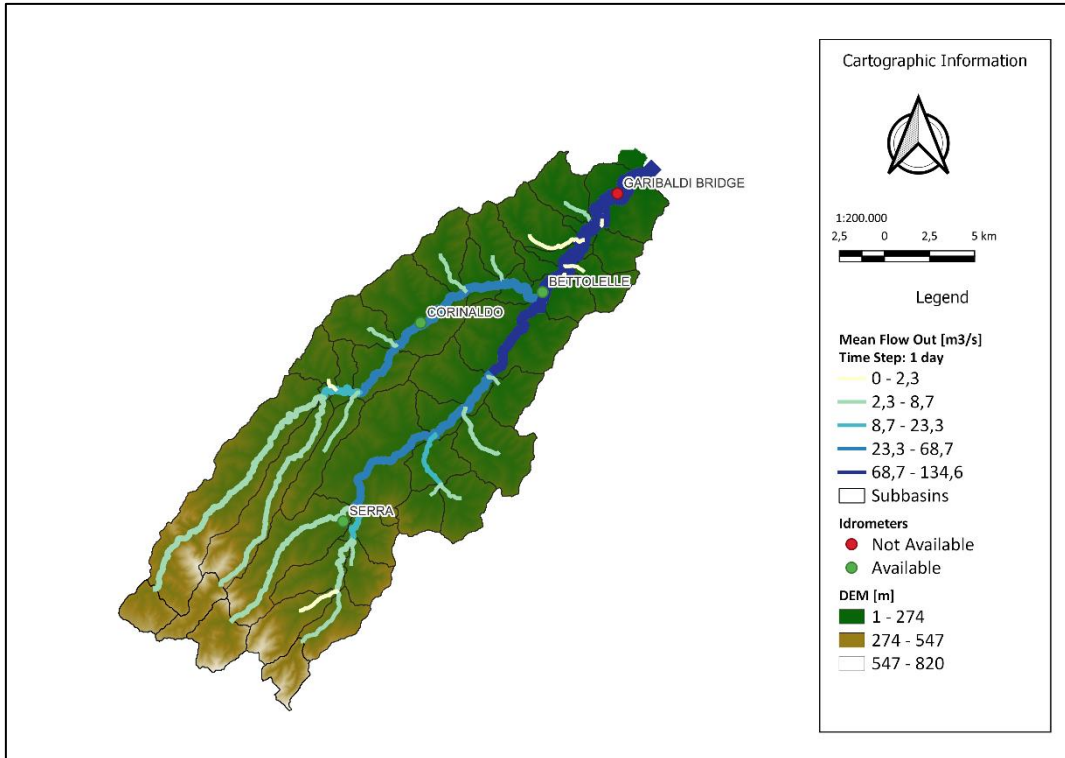


Figure 54: Average flow out during flood event in May 2014.

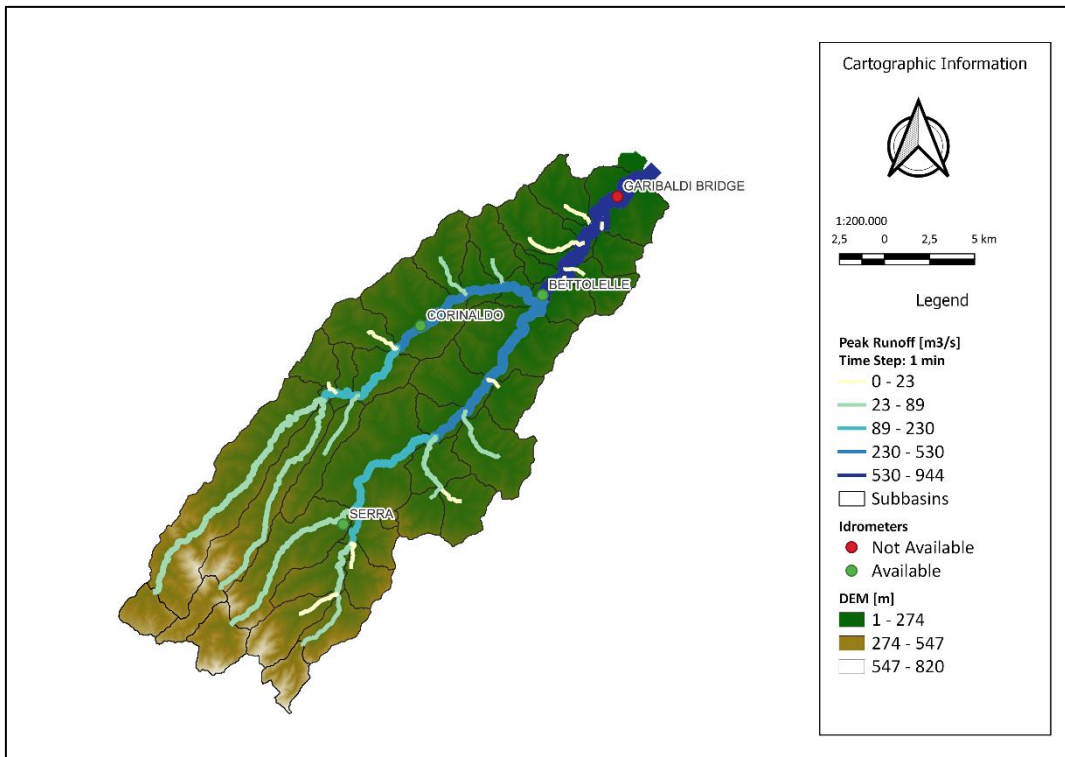


Figure 55: Peak runoff during flood event in May 2014.

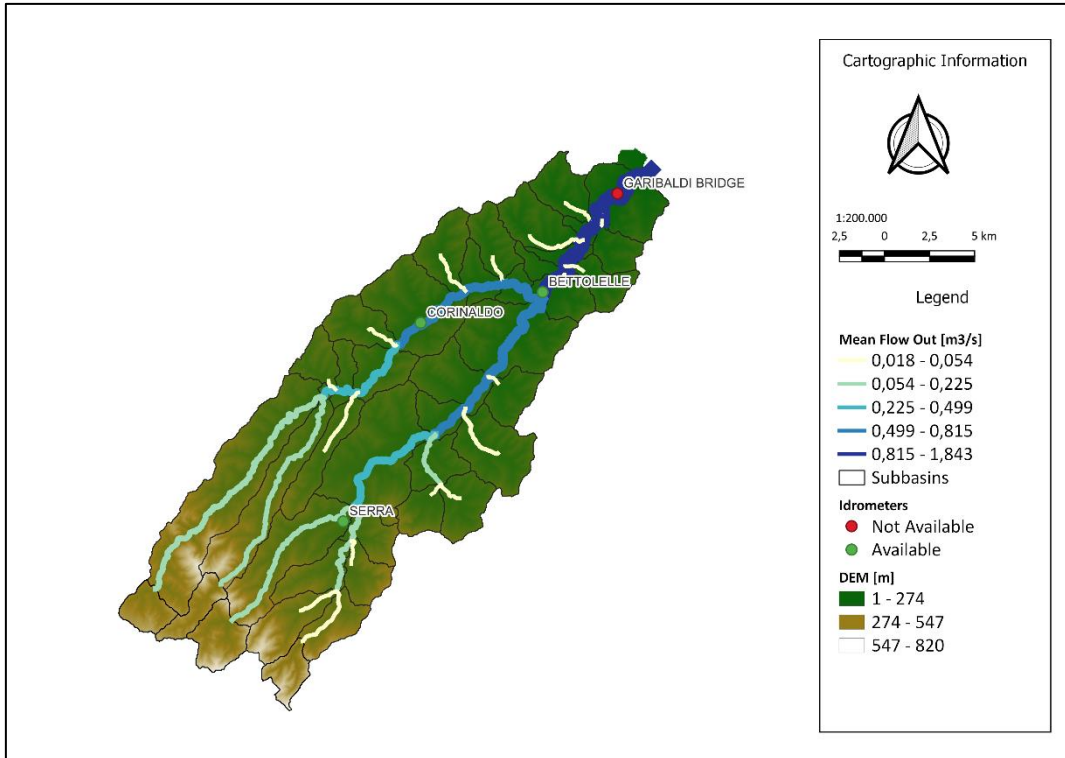


Figure 56: Average flow out during 2014.

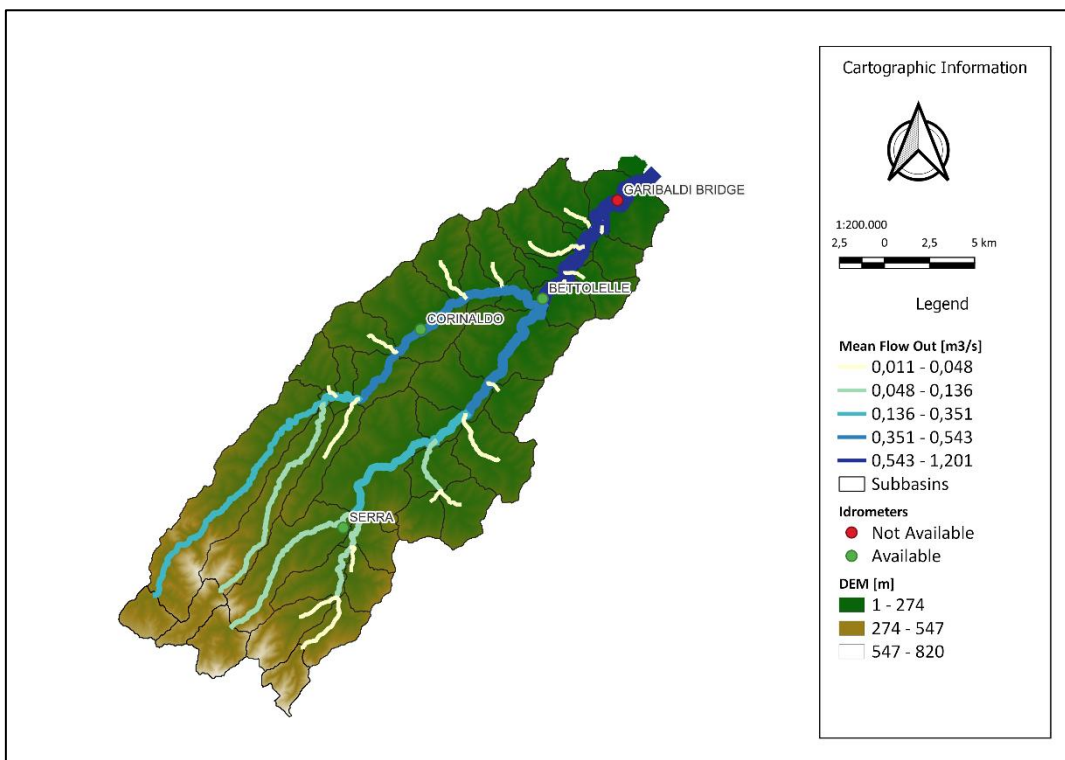


Figure 57: Average flow out during 2017.

### 5.3.2 Geologic results (2022, 2014, 2017)

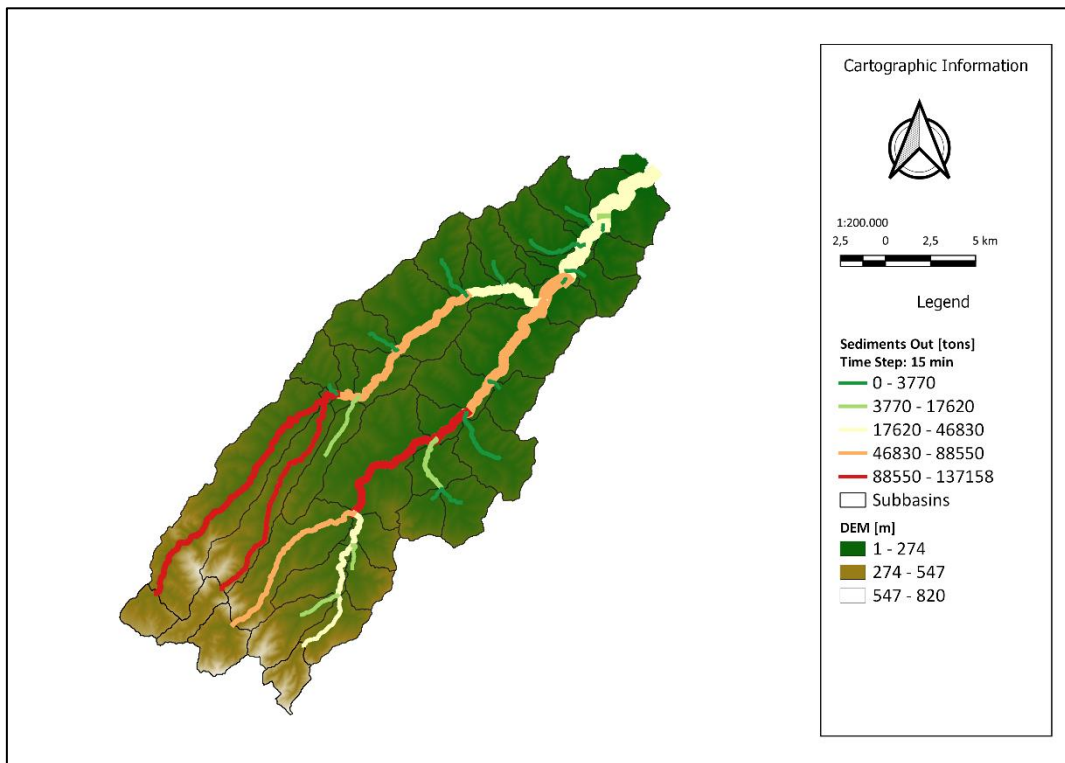


Figure 58: Sediments out during flood event in September 2022.

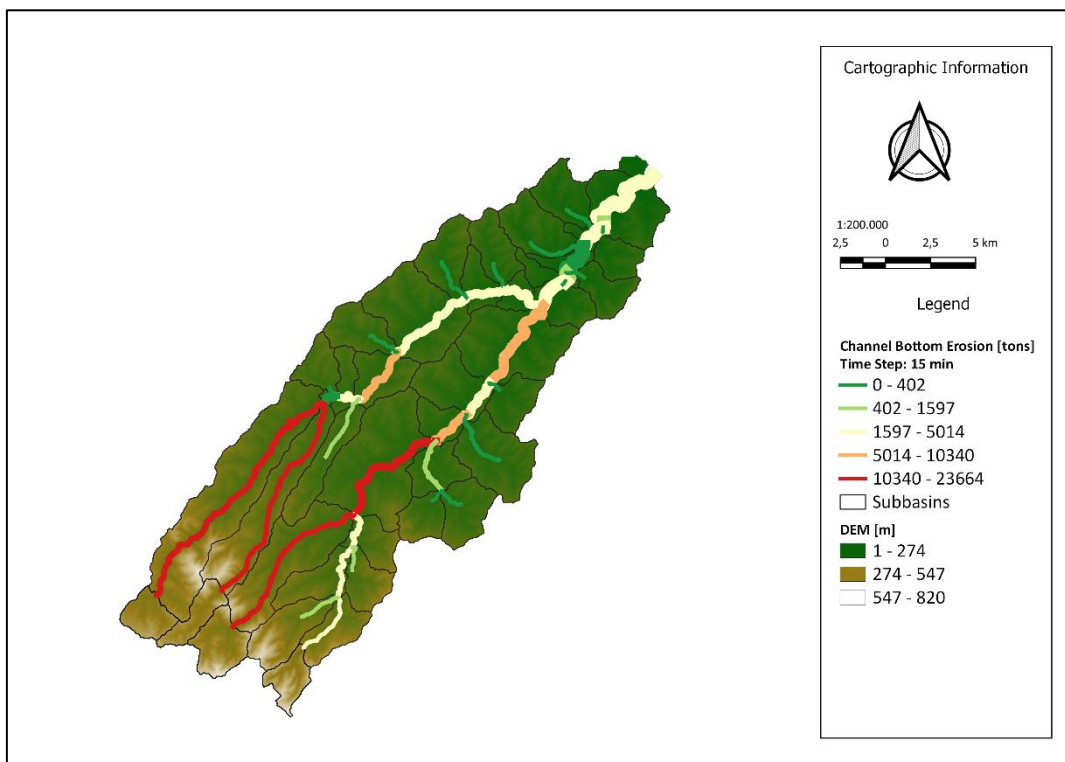


Figure 59: Channel bottom erosion during flood event in September 2022.

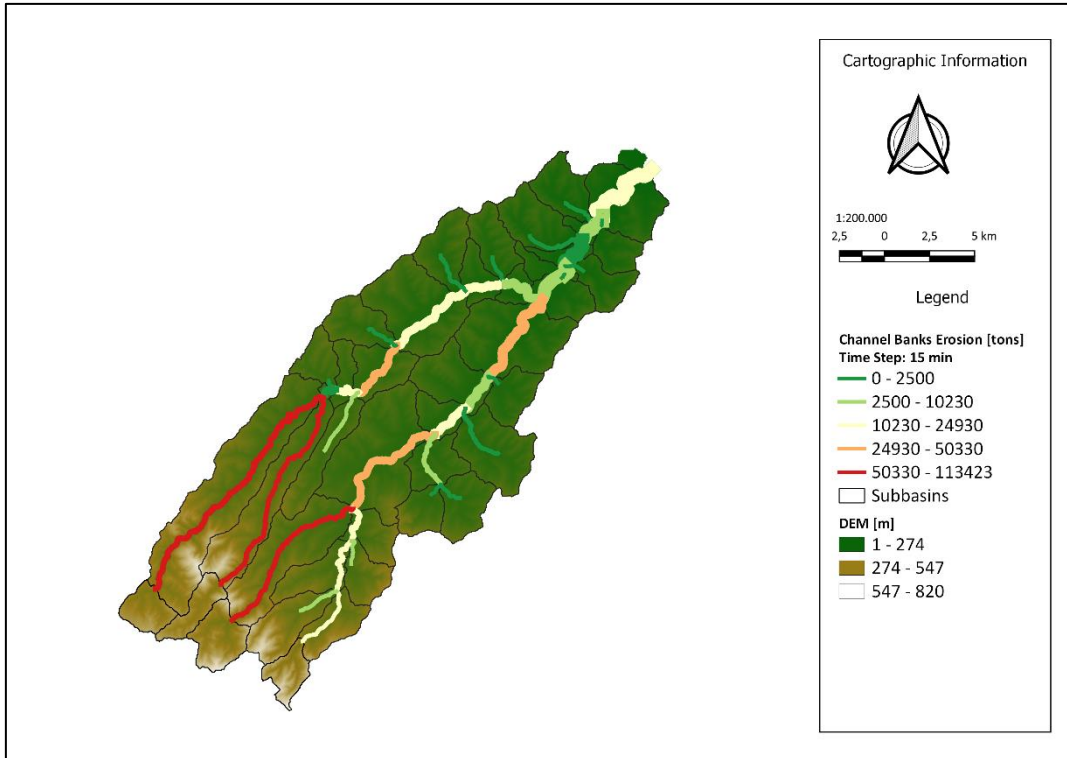


Figure 60: Erosion of banks during flood event in September 2022.

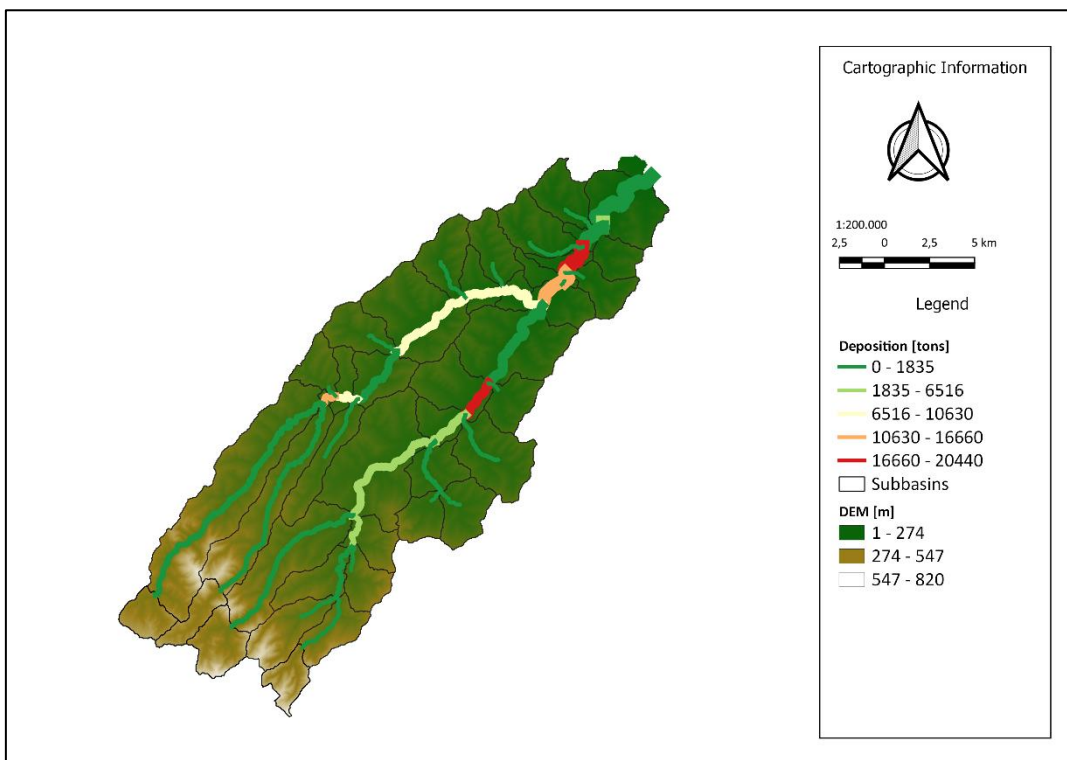


Figure 61: Deposition during 2022.



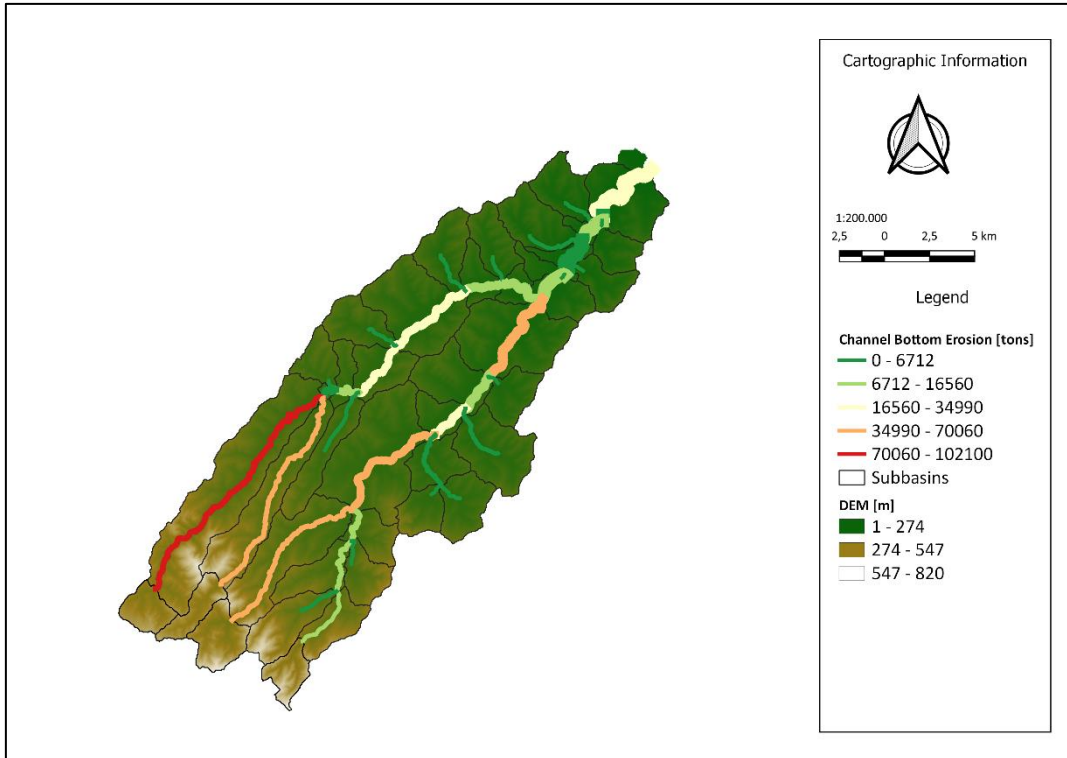


Figure 62: Channel bottom erosion during 2022.

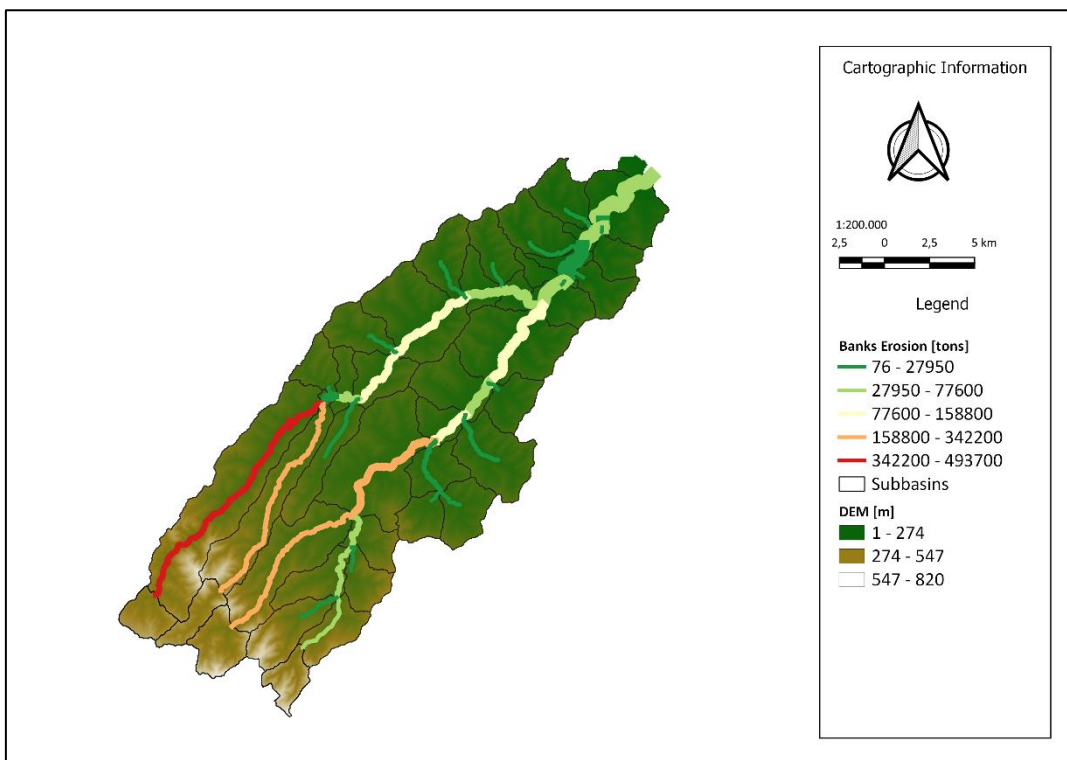


Figure 63: Banks erosion during 2022.



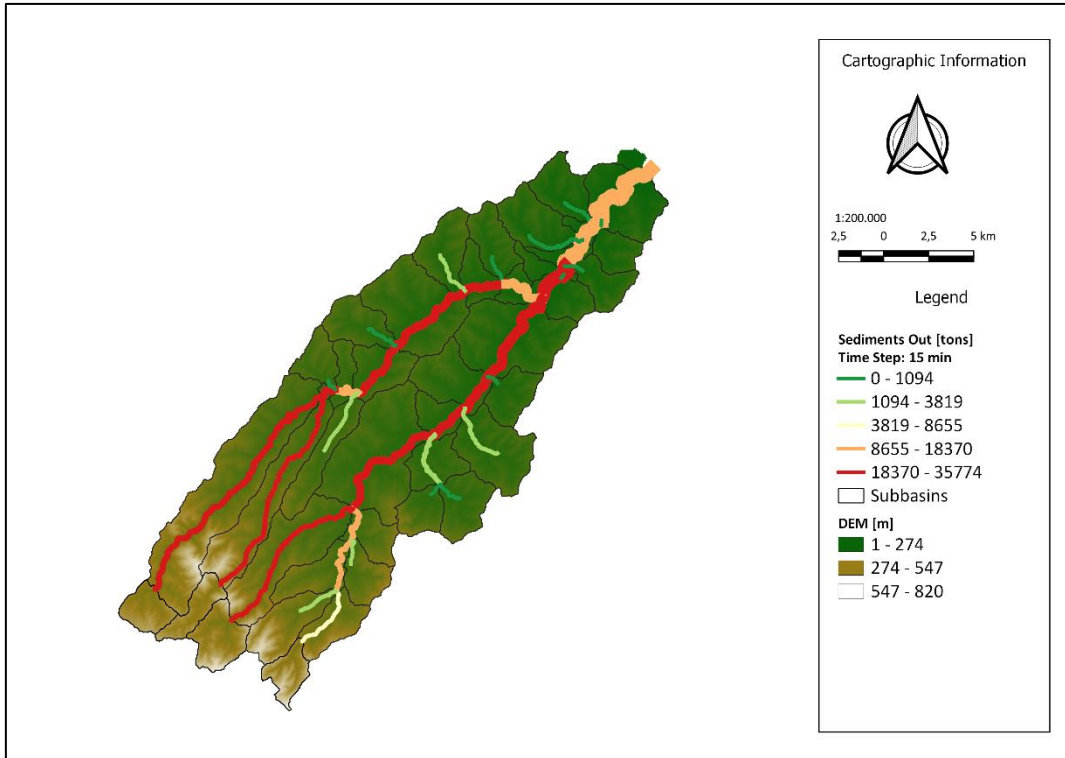


Figure 64: Sediments out during flood event in May 2014.

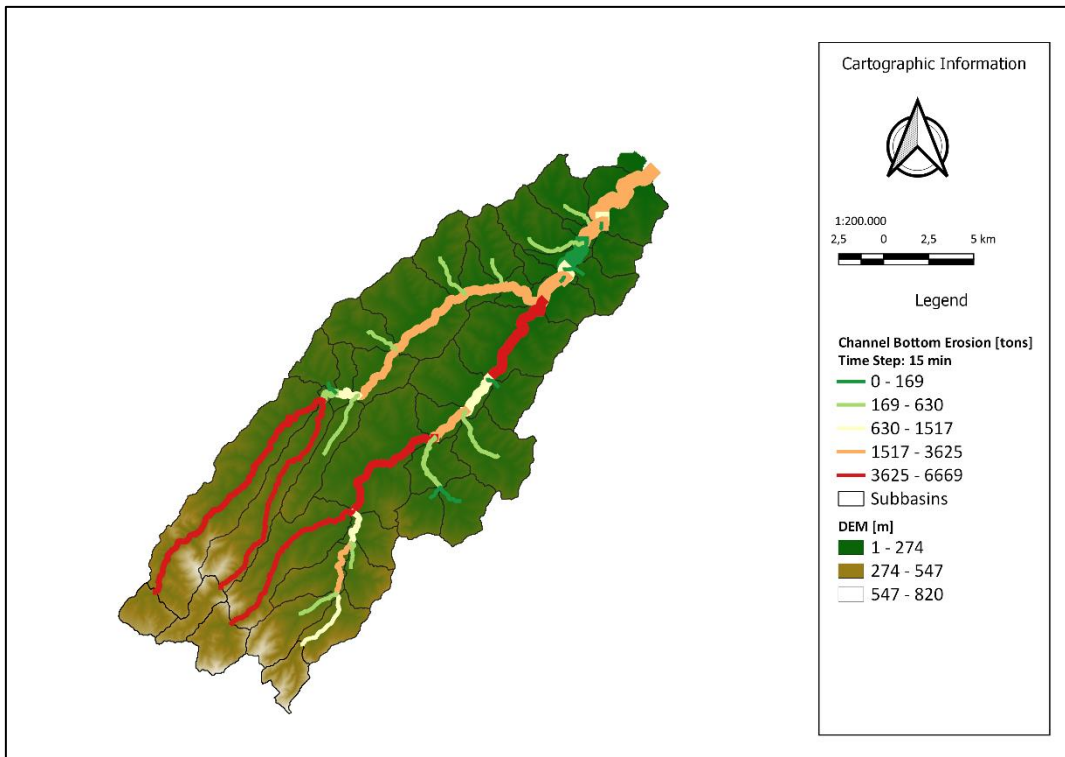


Figure 65: Channel bottom erosion during flood event in May 2014.

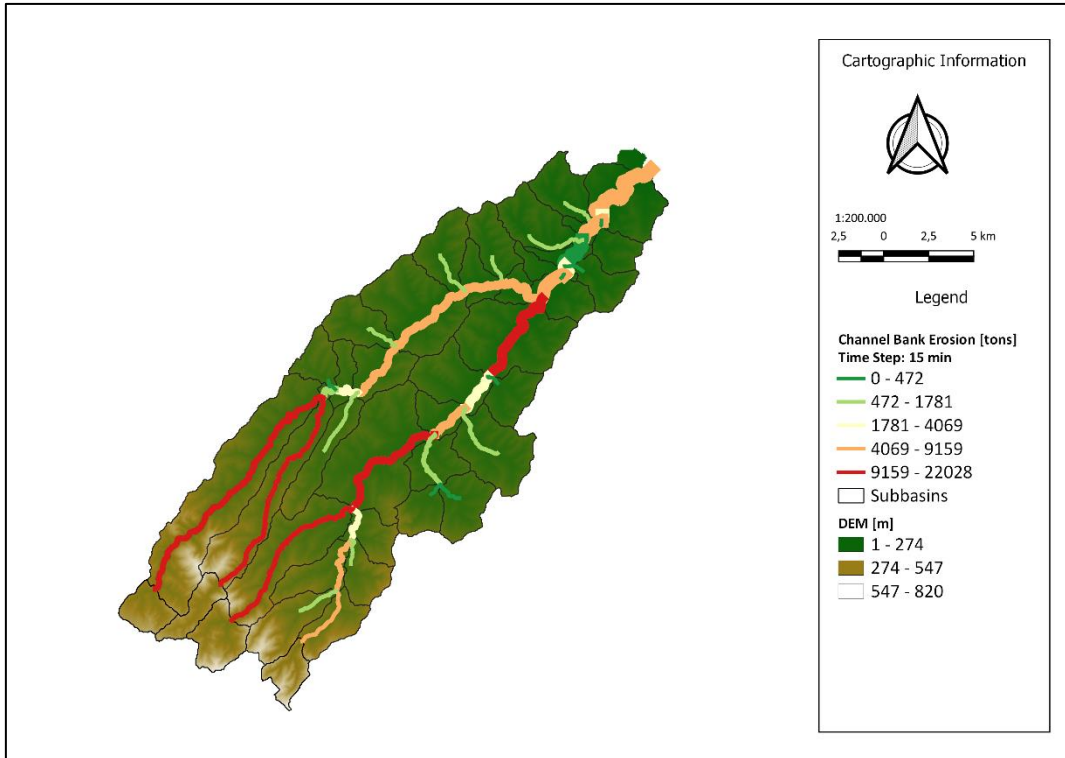


Figure 66: Banks erosion during flood event in May 2014.

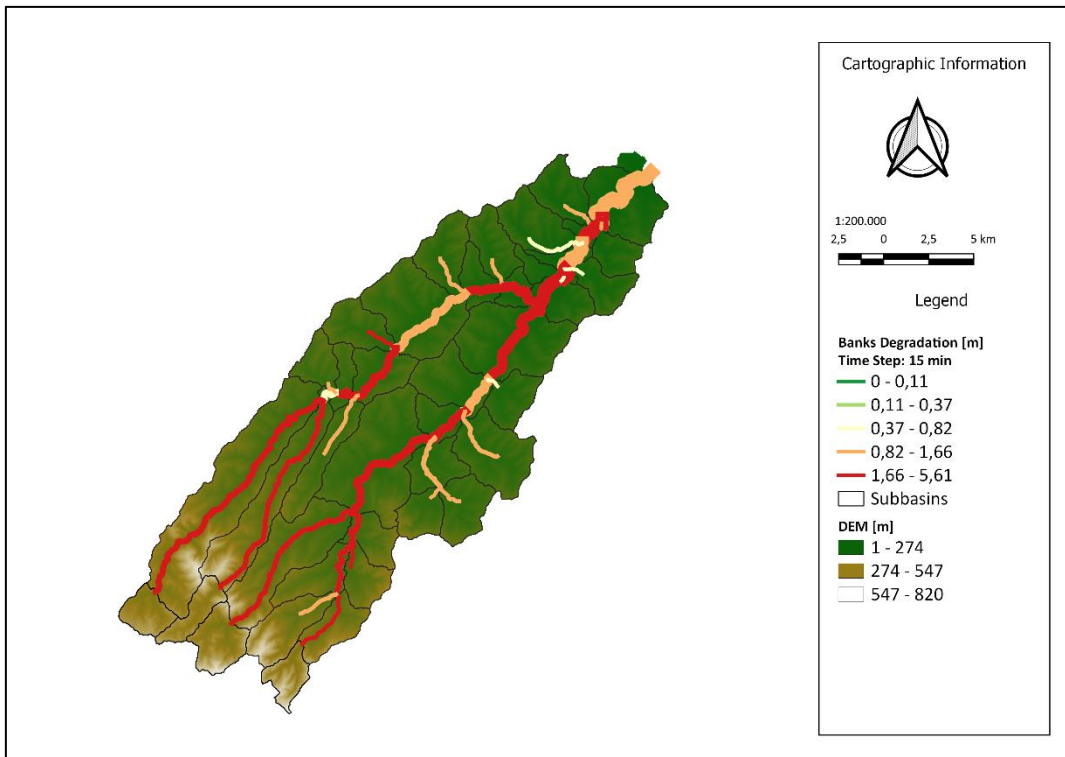


Figure 67: Banks degradation during flood event in May 2014.

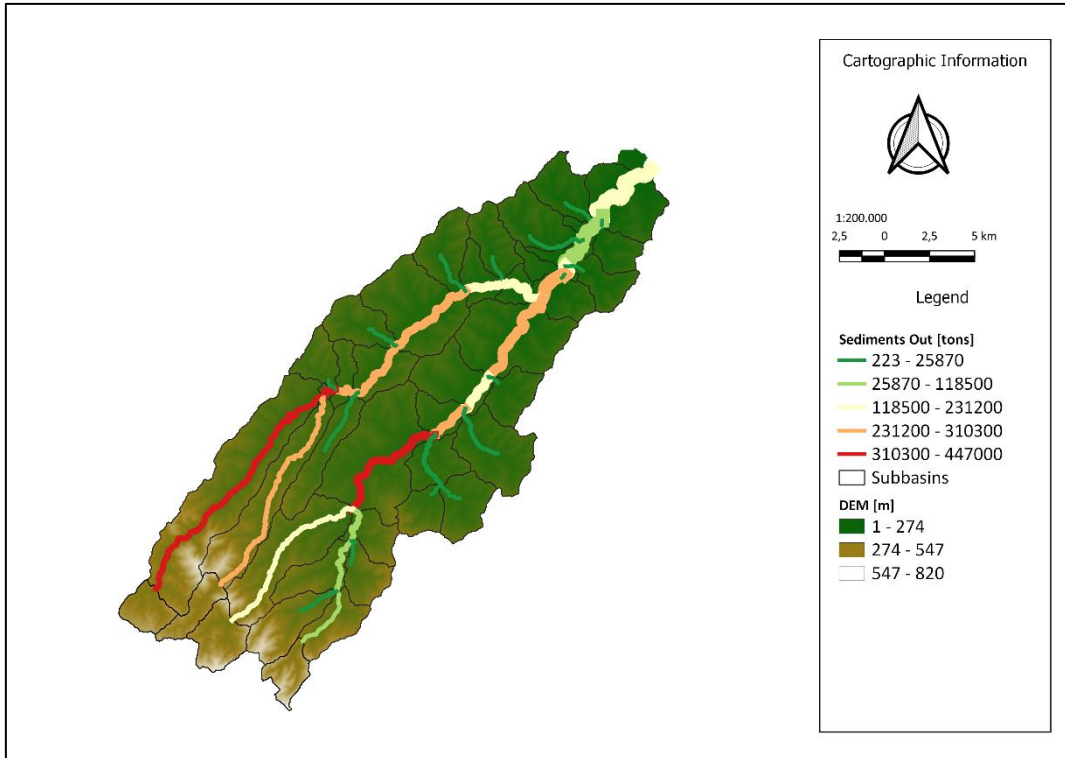


Figure 68: Sediments out during 2014.

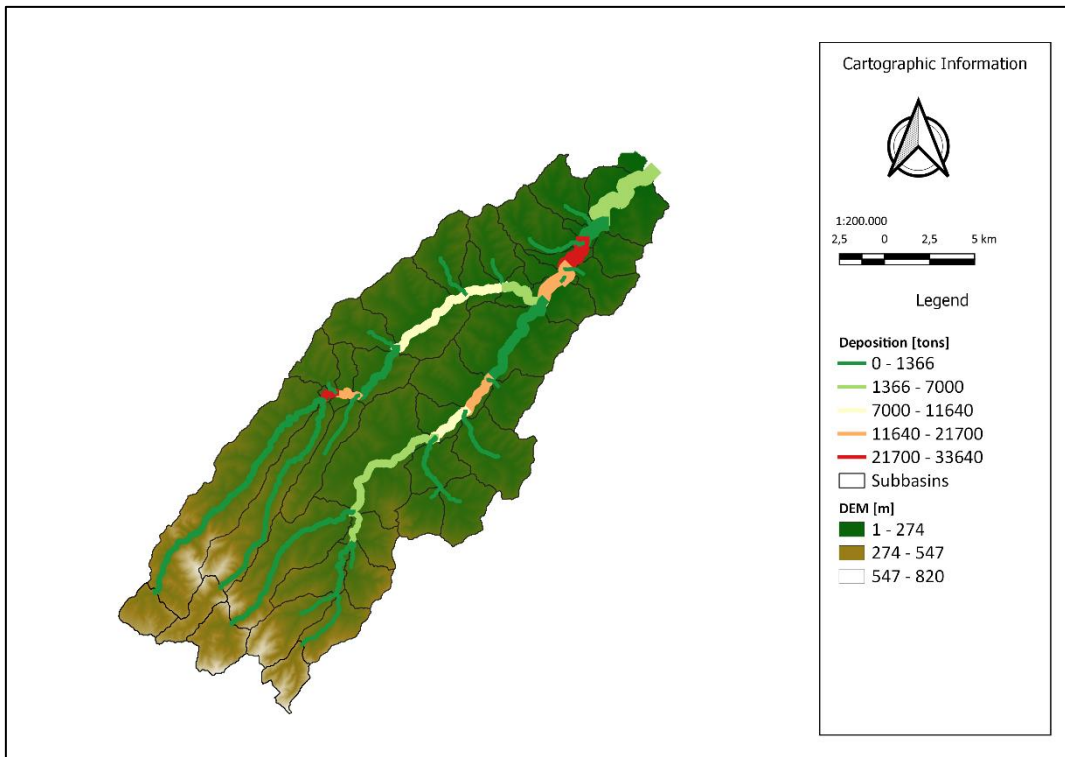


Figure 69: Deposition during 2014.

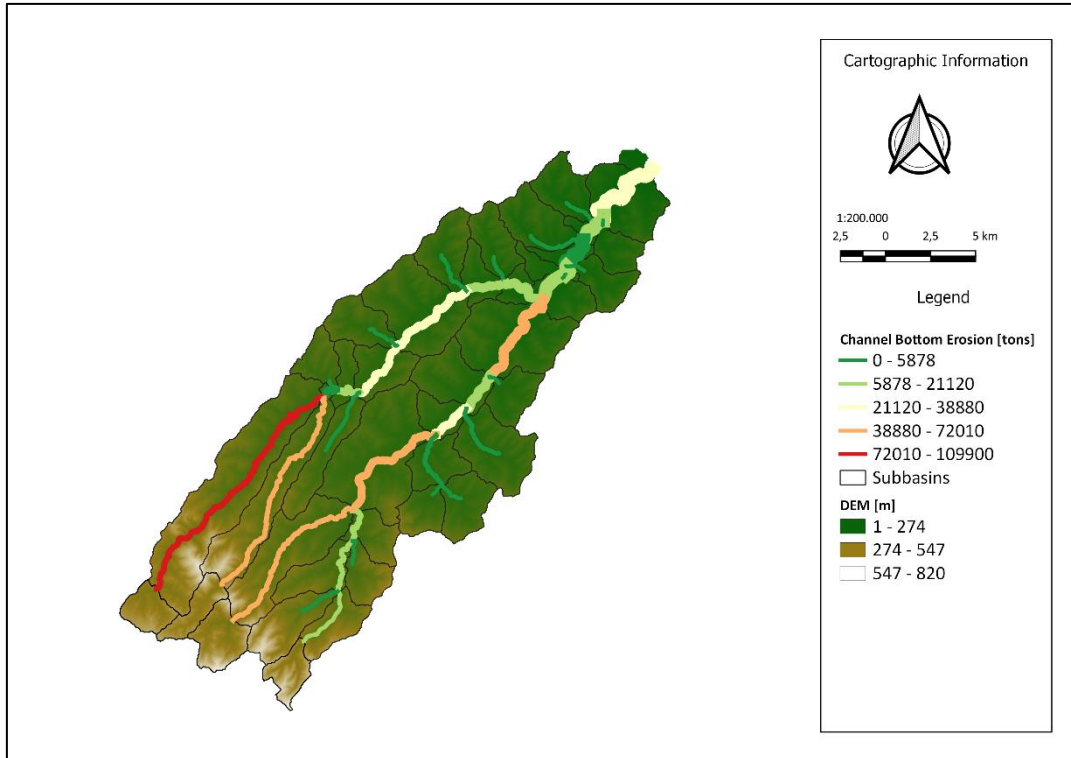


Figure 70: Channel bottom erosion during 2014.

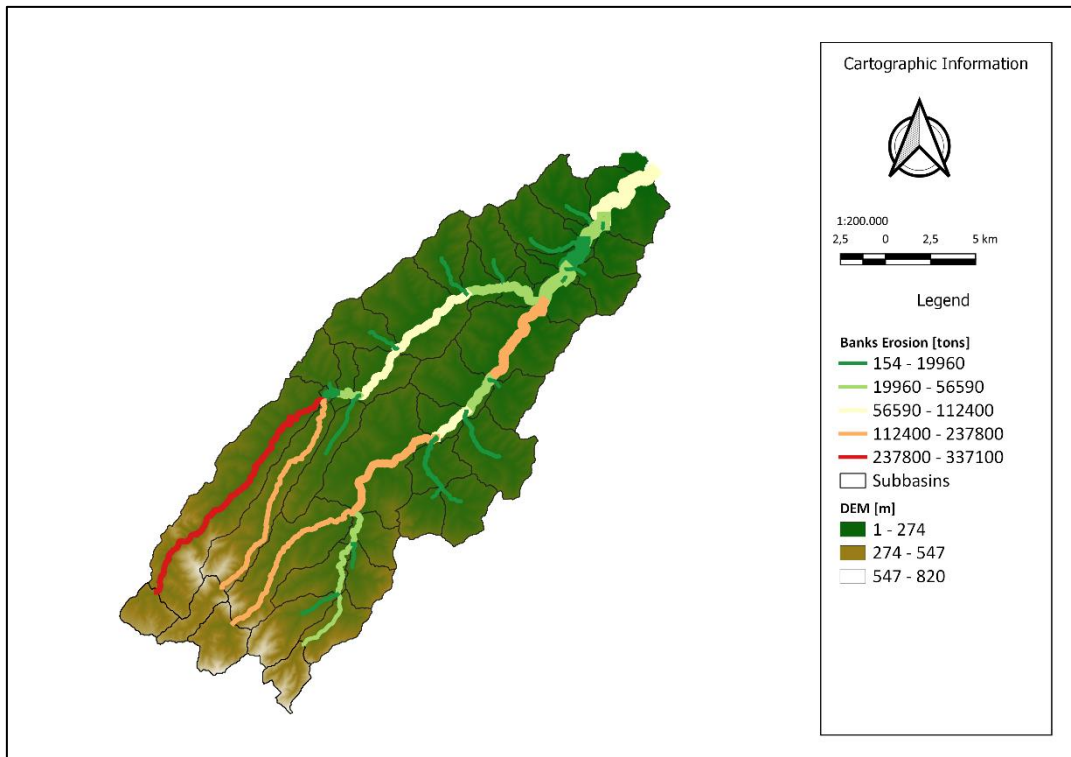


Figure 71: Banks erosion during 2014.

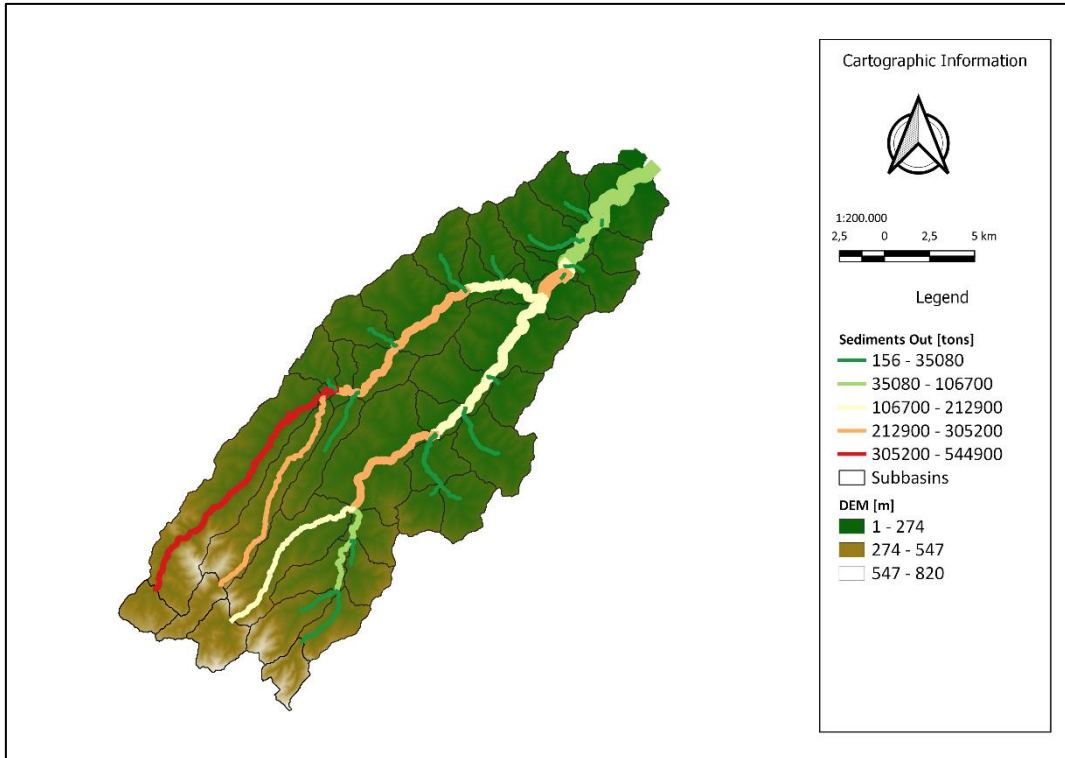


Figure 72: Sediments out during 2017.

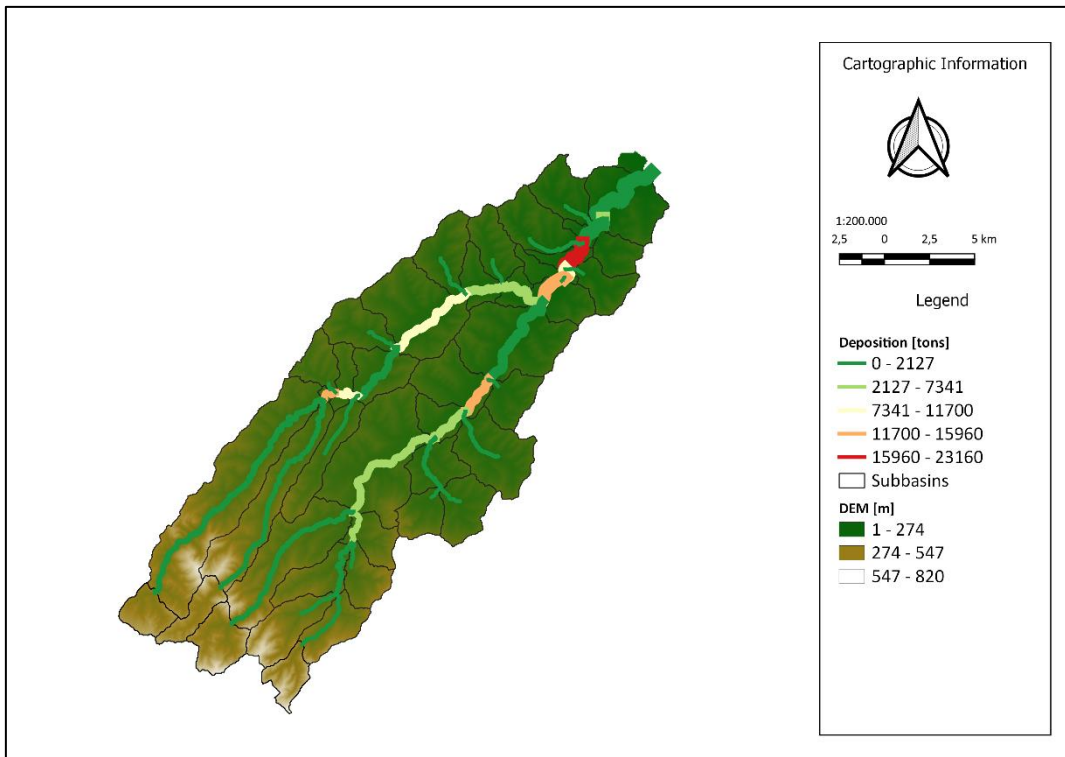


Figure 73: Deposition during 2017.



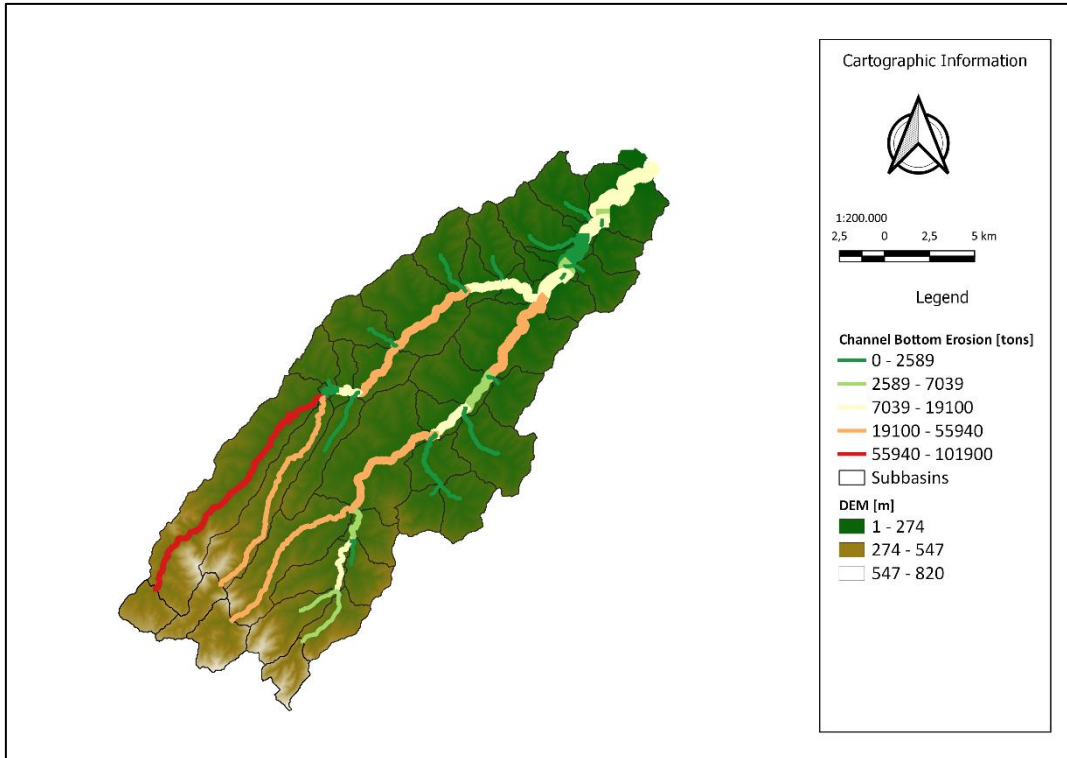


Figure 74: Channel bottom erosion during 2017.

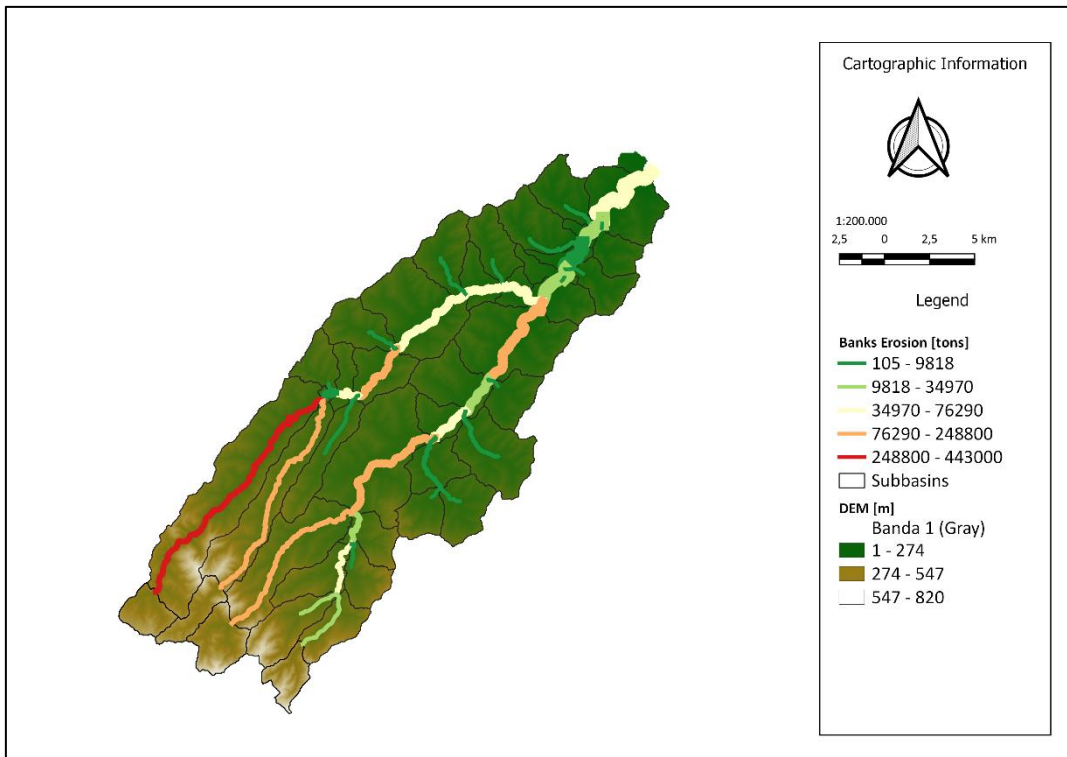


Figure 75: Bank erosion during 2017.

## 6. Discussions

### 6.1 Water discharge

The maps (Figures 52, 53) show the results obtained regarding the hydraulic part of the September 2022 flood event. The event was particularly complex to describe because the associated rainfall was extremely high and concentrated in the late afternoon of September 15<sup>th</sup>. For this reason, the average daily flow is not too high, as the ascending part of the wave was obtained between 10 p.m. and midnight on September 15<sup>th</sup> while the descending part was concentrated in the early hours of September 16<sup>th</sup>. This fact resulted in a huge obstacle in the modeling since SWAT cannot precisely determine the timing of the flood wave since it only has the daily cumulative in input. Despite this, SWAT allows the exploitation of several time steps (Table 10) that, starting from the daily precipitation data, make it possible to simulate with a good approximation the rainfall event.

Date	Mean flow out [m <sup>3</sup> /s]	Mean flow out [m <sup>3</sup> /s]		
	observed	SWAT		
	Bettolelle	Bettolelle 15 min	Bettolelle 1 day	Bettolelle 1 min
14/09/2022	0.0	0.1	0.1	0.1
15/09/2022	59.5	130.0	145.0	30.0
16/09/2022	64.6	20.0	5.0	25.0
17/09/2022	5.2	5.0	0.1	20.0
18/09/2022	2.9	0.1	0.1	16.0

Table 10: Mean flow out comparison for flood event of Sept. 2022.

The best result is offered by the 15-minute time step that assumes the flood wave concentrated mostly on September 15<sup>th</sup>. In fact, averaging the flood wave not taking into account the split into days gives a value of about 115 m<sup>3</sup>/s which is very close to the modeled value of 130 m<sup>3</sup>/s. The discrepancy between the two values is about 13 %.

On the other hand, the peak runoff, was modeled more effectively by the model having time step of 1 minute. Both the time step and the 15-minute time step generated extremely high peaks. This could be due to the lack of compatibility between the time step-based models offered by SWAT and the nature of the September 2022 event. Even considering the result offered by the 1-minute time step, the relative error is about 50%, thus being not significant.

Date	Peak runoff [m <sup>3</sup> /s] observed	Peak runoff [m <sup>3</sup> /s] SWAT		
	Bettolelle	Bettolelle 15 min	Bettolelle 1 day	Bettolelle 1 min
15/09/2022	623	4148	4582	948

*Table 11: Peak Runoff comparison for Flood Event of Sept. 2022.*



The hydraulic part for the year 2022 has been shown in Figure 46, and as a validation, a monthly analysis was carried out showing the flow rate trends compared to the values obtained by the hydrometers (Figure 76). The comparison will show not only the trend but also the absolute and relative discrepancy of the flow rate values obtained through hydrometers and those obtained through SWAT.

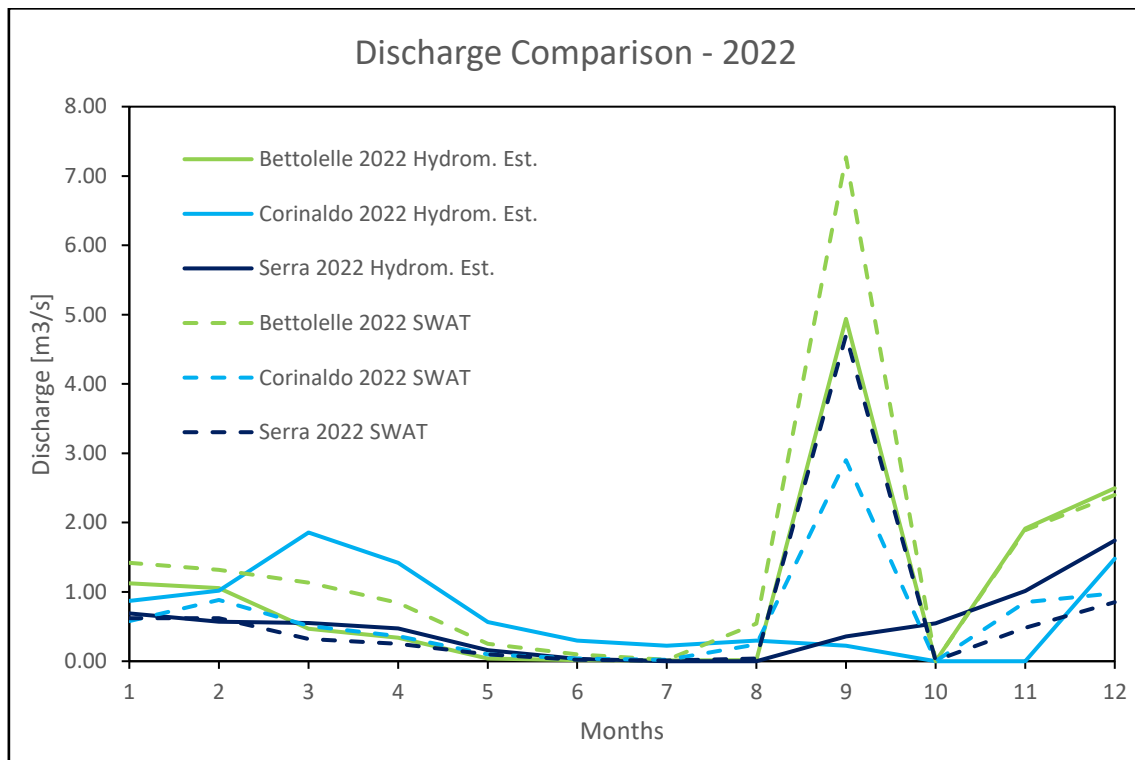


Figure 76: Discharge comparison for 2022 between SWAT results and discharge from hydrometrical estimation.

Comparison of the observed data with those obtained from SWAT yielded satisfactory results in that the flow rate trends are respected throughout most of the year and the values do not show obvious discrepancies. The major critical issues were found in the definition of flow values from the outflow scales. For rather high flow rates the results are satisfactory, but in the case of very low flow rates problems are present, as situations where the upstream flow rate is higher than the downstream flow rate. In addition, the Corinaldo and Serra de' Conti sensors present outlier values such as very high elevations on days without rain or with no match at the downstream station of Bettollelle. Moreover, the latter present periods without any data, which last for months. Particularly after the September 2022 flood event, the sensors stopped working for a long time. For these reasons, some months are characterized by larger or smaller differences; thus, the

Corinaldo and Serra de' Conti stations were excluded from the analysis on relative and absolute differences. The Bettollelle station has the most complete and consistent values for the 3 analyzed years so for this reason, it was chosen as the station for the validation of the monthly mean flow rate (Figure 77). The absolute differences over the year are maintained at small values except for the month of September, which leads to an absolute error of about 2.3 m<sup>3</sup>/s, and in the summer months the relative errors are high due to SWAT's lack of accuracy in defining dry weather flows. Nevertheless, the annual trend is modeled correctly, and the average annual value is very close to the observed one, with a discrepancy of about 25%.

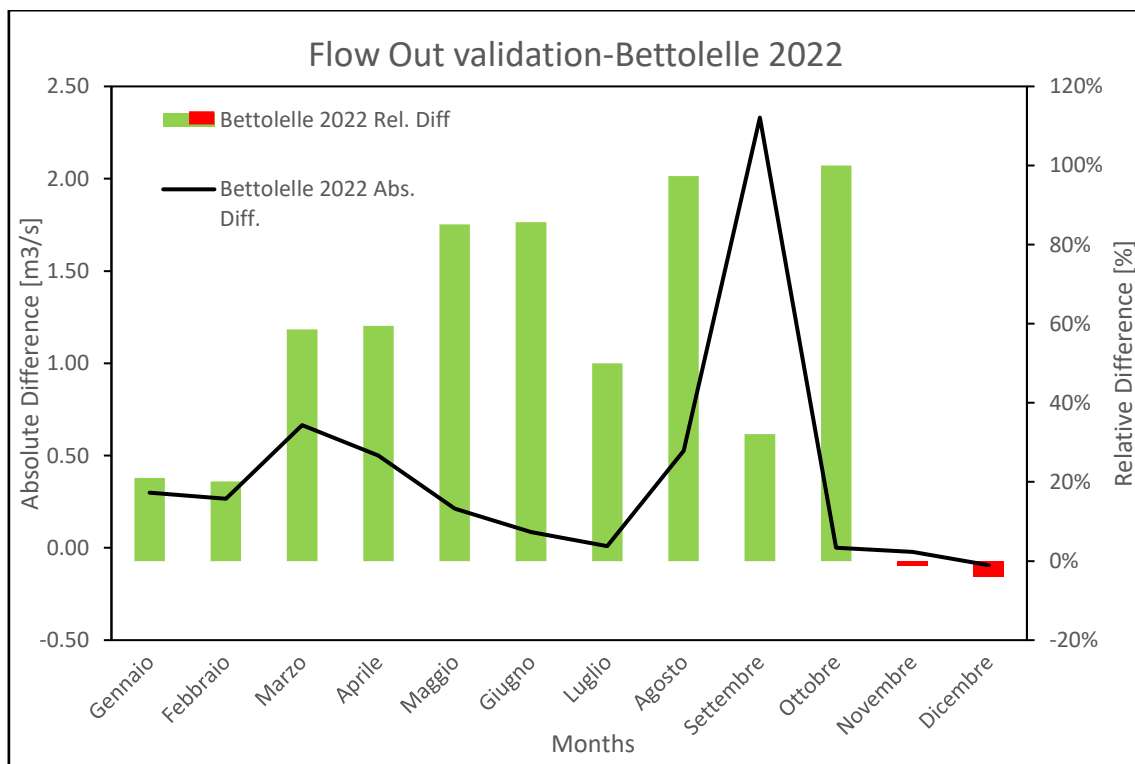


Figure 77: Flow Out validation at Bettollelle station for monthly analysis.

As a final verification, in the case of the annual simulations, the Nash-Sutcliffe efficiency (NSE) was evaluated, which is a useful statistical index for determining the relative magnitude of residuals defined as the difference between observed and simulated values squared compared with the measure of variance of the observed data (87). This index is expressed by the relationship (Eq. 90):

$$NSE = 1 - \frac{\sum_{i=1}^n (S_i - O_i)^2}{\sum_{i=1}^n (O_i - \bar{O})^2} \quad (Eq. 90)$$

Where:

$S_i = \text{simulated values}$

$O_i = \text{observed values}$

$\bar{O} = \text{mean of observed values}$

Stations	NSE index
Bettolelle	0.73
Corinaldo	-1.63
Serra de' Conti	-6.52

*Table 12: NSE indexes for 2022.*

The index ranges between a value of minus infinity and 1, and the closer this value is to 1, the more accurate the model is. Values equal to or close to 1 indicate that the model corresponds perfectly to the observed values. A value of zero indicates that the model and the mean of the observed values have the same accuracy while values less than zero indicate that the mean is a better predictor than the model. In the case of 2022, modeling Bettolelle gave a good result while in the case of Corinaldo and Serra de' Conti they are below zero. This fact could be attributable to the poor ability of SWAT to define extremely low flow rates or the low accuracy of the stage-discharge curves for low water heights. Indeed, 2022 was characterized by periods of extreme drought where discharges were close to zero. Another problem can be attributable to the lack of data due to the passage of the flood wave at the Corinaldo and Serra de' Conti stations.

The May 2014 event is configured extremely differently from the one that occurred during September 2022. In fact, it is characterized by smaller peaks of rainfall intensity but has a greater distribution over the entire Misa basin and a longer duration (Figures 54, 55). This certainly leads to greater modelability as floods of this type lead to rather high flows over a large period of time with high peaks but lower than events like the one in 2022 that was configured as a flash flood with extremely concentrated flood waves in a few hours and very high peaks. Given these characteristics, the time step that performs better about modeling the average daily discharge is the one-day time step. It in fact models with good approximation May 3<sup>rd</sup>, which was the one characterized by the highest flow rates. In fact, a discrepancy between actual and modeled value of about 15% is found.

Date	Mean flow out [m <sup>3</sup> /s]	Mean flow out [m <sup>3</sup> /s]		
	Observed	SWAT		
	Bettolelle	Bettolelle 15 min	Bettolelle 1 day	Bettolelle 1 min
01/05/2014	4.2	2.0	2.0	3.0
02/05/2014	4.5	3.0	2.3	3.0
03/05/2014	140.7	90.0	120.0	20.0
04/05/2014	28.0	8.0	2.3	20.0
05/05/2014	7.8	3.0	2.0	10.0

Table 13: Mean flow out comparison for flood event of Sept. 2014.

In contrast, for modeling peak flow rate, it is necessary to evaluate all time steps analyzed because 1-day and 15-minute time steps lead to outliers. In this case, the one that best approximates the situation is the 1-minute one, which produces a very good performance for short period analysis. In fact, the modeled value deviates by about 4%.

Date	Peak runoff [m <sup>3</sup> /s]	Peak runoff [m <sup>3</sup> /s]		
	Observed	SWAT		
	Bettolelle	Bettolelle 15 min	Bettolelle 1 day	Bettolelle 1 min
03/05/2014	555	1966	2193	530

Table 14: Peak runoff comparison for flood event of Sept. 2014.

The results obtained from the analysis of this event (Tables 13, 14) were more accurate than that of September 2022 because SWAT was developed to predict the hydrogeological routing of basins characterized by temperate climates, and floods such as that of 2014 can be modeled well. The one in 2022 was an unconventional event, both in terms of timing of occurrence and intensity. This explains the lack of precision for its modelling.

Flow rates calculated from heights, in the case of 2014, had the most problems particularly with regard to minimum runoff rates. The results (Table 15) were often conflicting and produced lower downstream flow rates than upstream flow rates. This was mainly due to not optimal definition of the stage-discharge curves, which were inaccurate for the year 2014. This resulted in high errors on the annual averages.

Stations	Observed Mean Flow Out [m <sup>3</sup> /s]	SWAT Mean Flow Out [m <sup>3</sup> /s]	Rel. Errors [%]
Bettolelle	2.01	1.53	-27%
Corinaldo	1.34	0.61	-75%
Serra	0.60	0.49	-20%

*Table 15: Mean flow out comparison.*

For the annual analysis of 2014 (Figure 56), despite the discrepancy in absolute value in particular in the first part of the year between the modeled values and those obtained through water heights, the annual trend is respected even though the modelled values are lower than the observed ones, in particular in the first half of the year (Figure 78).

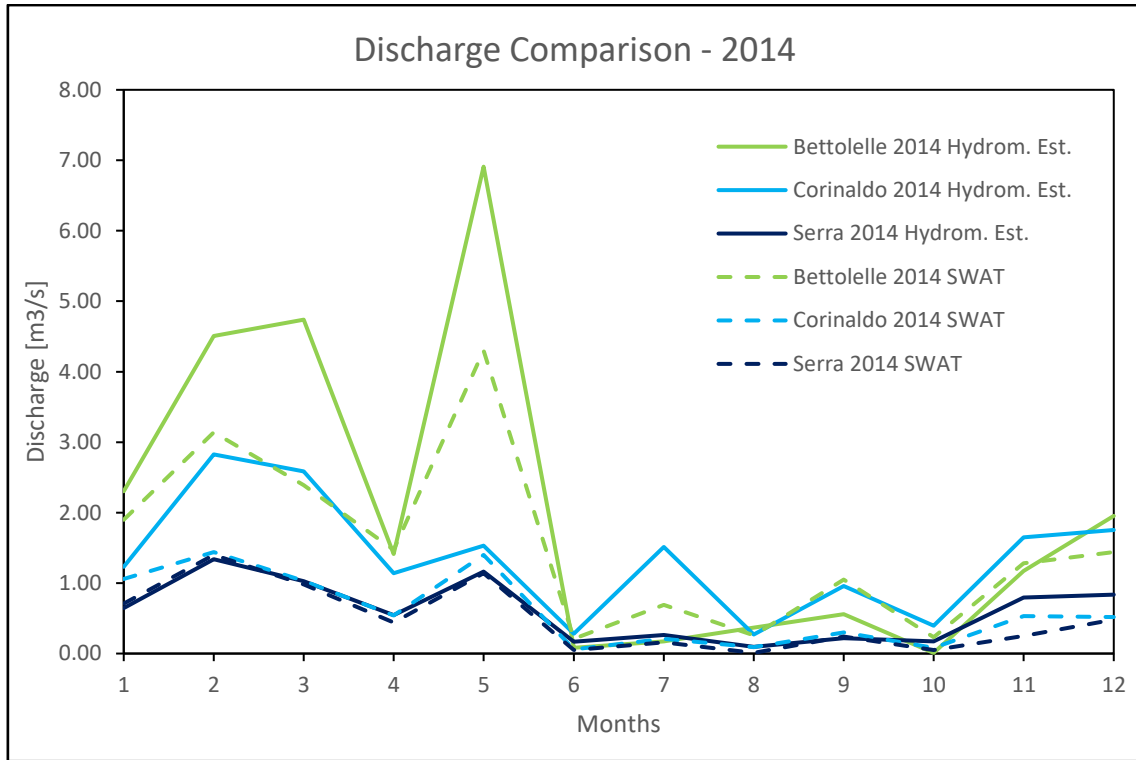


Figure 78: Discharge comparison for 2014 between SWAT results and discharge from hydrometrical estimation.

For the Bettollele flow out validation (Figure 79), the main problems are related to the first part of the year where errors, both relative and absolute, are most evident. In contrast, the second part of the year is well modeled and the trend is respected.

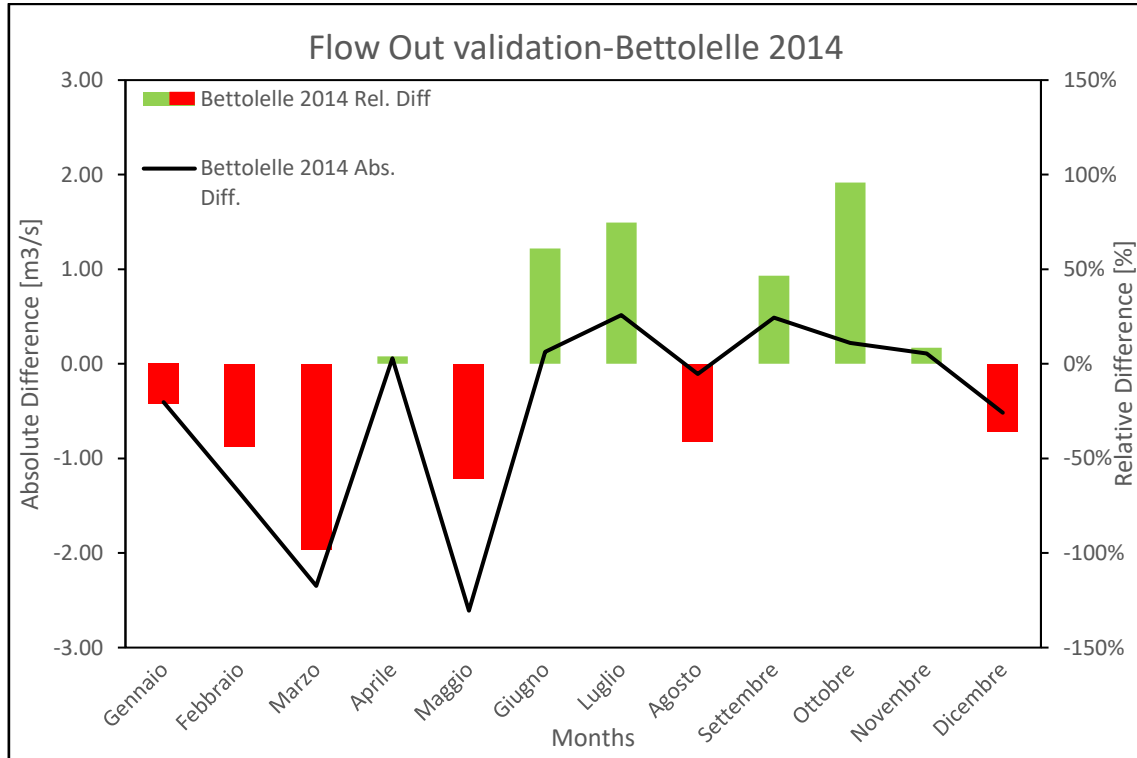


Figure 79: Flow Out validation at Bettollele station for monthly analysis.

Stations	NSE index
Bettollele	0.72
Corinaldo	-0.32
Serra de' Conti	0.76

Table 16: NSE indexes for 2014.

In the case of 2014, the NSE index provided better results than the analysis conducted for the year 2022 in that both the Bettollele and Serra stations are characterized by values greater than zero while the Corinaldo station, although still characterized by a value below zero, it is greater than in the previous case.

Modeling for 2017 (Figure 57) yielded good results for both the Bettolle and Corinaldo stations. The most problematic situation appears to be at Serra de' Conti where the discrepancy is quite high even though it is based on relatively small flow rates. It is also noted that the calculated flow rates are consistent with those calculated for 2022 and differ more from those of 2014, which suffer from the problems outlined above.

Stations	Observed Mean Flow Out [m <sup>3</sup> /s]	SWAT Mean Flow Out [m <sup>3</sup> /s]	Rel. Errors [%]
Bettolle	1.28	1.07	-18%
Corinaldo	0.49	0.49	1%
Serra	0.45	0.29	-42%

*Table 17: Mean Flow Out comparison.*

Comparison of monthly values shows an excellent trend for the Bettolle and Corinaldo stations, although the latter suffers from problems in the first part of the year, during the months of January through February. This problem could be attributable either to incorrect modeling by SWAT due to a lack of precision in defining geoclimatic conditions, or to errors attributable to the definition of stage-discharge curves. The Serra de' Conti station, on the other hand, suffers from noticeable problems throughout the year, and in this case the cause could be the lack of precision of the measurements or the incorrect definition of the stage-discharge curves.



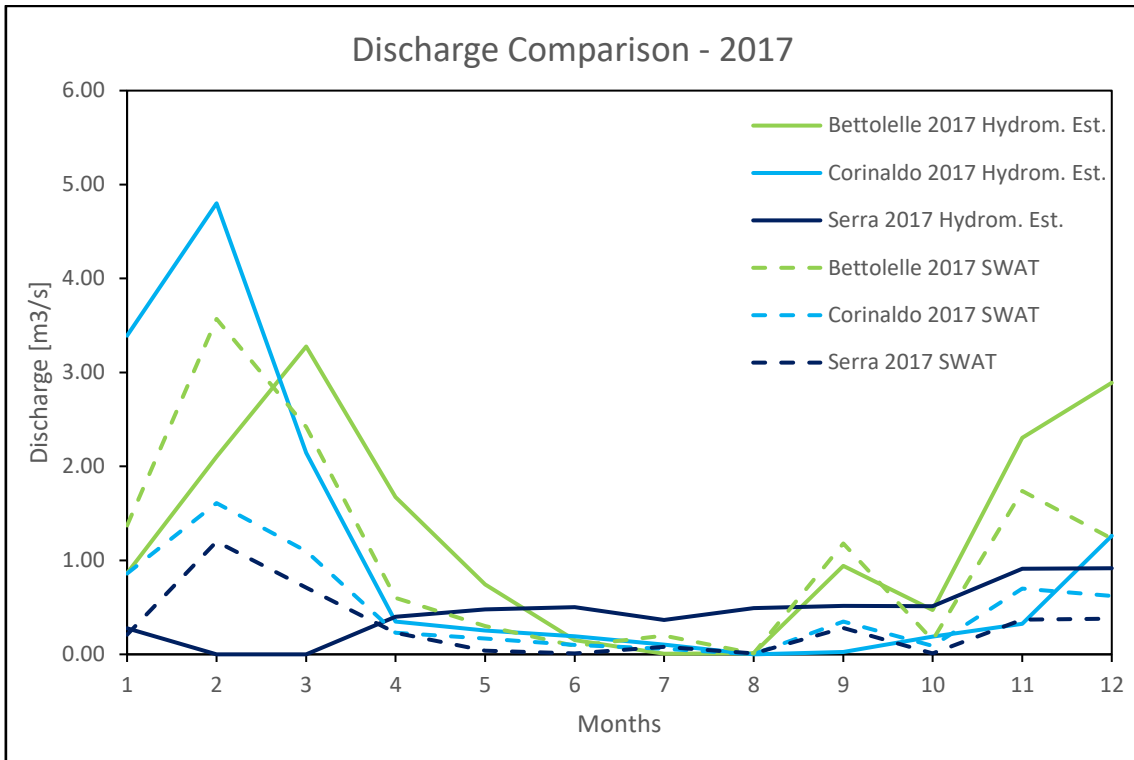


Figure 80: Discharge comparison for 2017 between SWAT results and discharge from hydrometrical estimation.

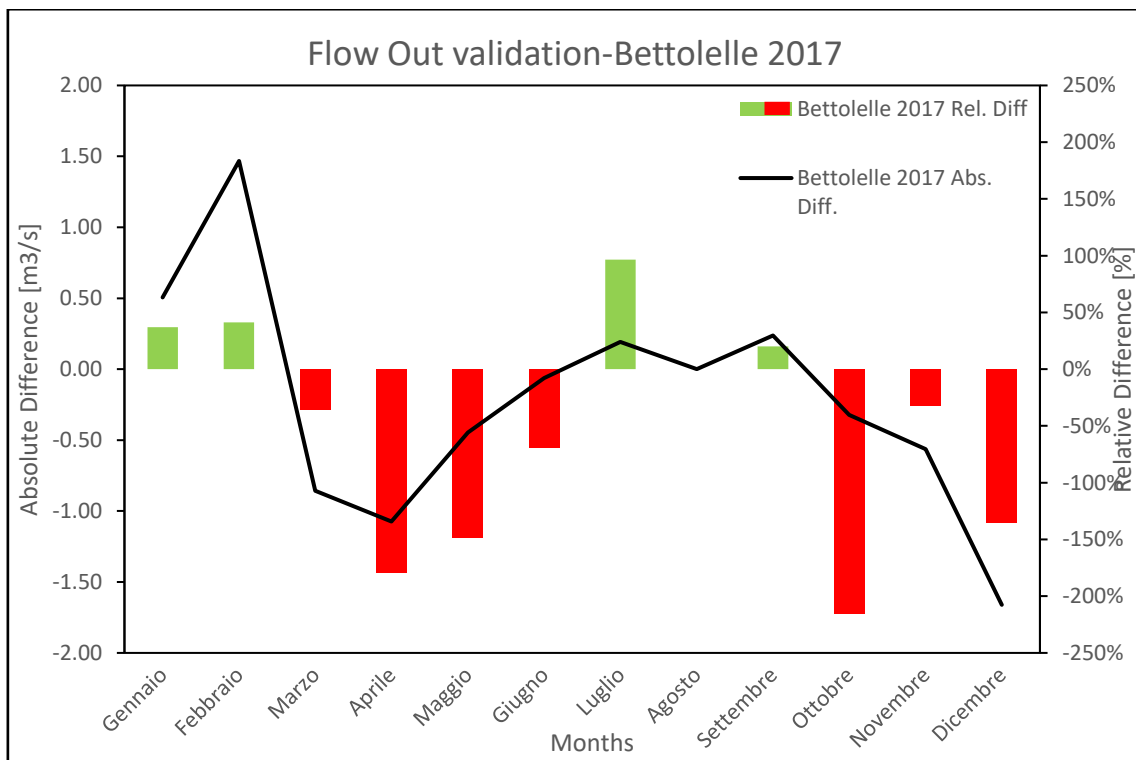


Figure 81: Flow Out validation at Bettlelle station for monthly analysis.

The determination of the NSE index for the year 2017 yielded good results for both the Bettolle and Corinaldo stations, as they have values above zero. The Serra station, on the other hand, presents a negative situation as the index stands at a value of about -3.

Stations	NSE index
Bettolle	0.45
Corinaldo	0.32
Serra de' Conti	-3.07

*Table 18: NSE indexes for 2017.*

As in the previous cases, the causes may be attributable both to SWAT inaccurately defining very low flow rates and to the definition of the observed flow rates due to poor accuracy of the stage-discharge curves. In conclusion to the determination of the NSE indices, it is evident that SWAT is not suitable for the analysis of very low flow rates but produces good results under conditions of higher flow rates, such as for the case of Bettolle, which is always characterized by values close or above 0.5.

## **6.2 Sediment erosion and transport**

In contrast to the hydraulic part, the sediment generation part cannot be validated quantitatively because there are no available sediment data. This also makes comparison with semi-empirical methods that assess basin-wide erosion at the outlet level ineffective. Nevertheless, it is possible to see how a flood event of this magnitude greatly affects annual sediment production. It can be seen from the maps (Figures 58, 59, 60) that erosion is concentrated more in the mountainous and hilly areas. This is due to two factors which are the positioning of rainfall with higher intensity that was concentrated between the municipality of Colle and Arcevia and the predisposition of mountain slopes to erosion since they are characterized by exposed terrain on steep sides and availability of loose material. The comparison of the maximum annual erosion values with the maximum erosion on September 15<sup>th</sup> shows that about 25% of the annual total (Figure 47) was produced in about 6 hours. This hints at the significance of erosion in flood events, which consequently produces extensive damage to areas in the valley bottom as debris is set in motion by the water current, which in turn generates solid flow. Based on the data about sediment production and deposition are not available, the comparison between the obtained results and the actual data will focus on estimating the extent of bank erosion, measured in meters (Figure 82), from photos of the event. They will refer to the areas that have been most subject to this phenomenon.

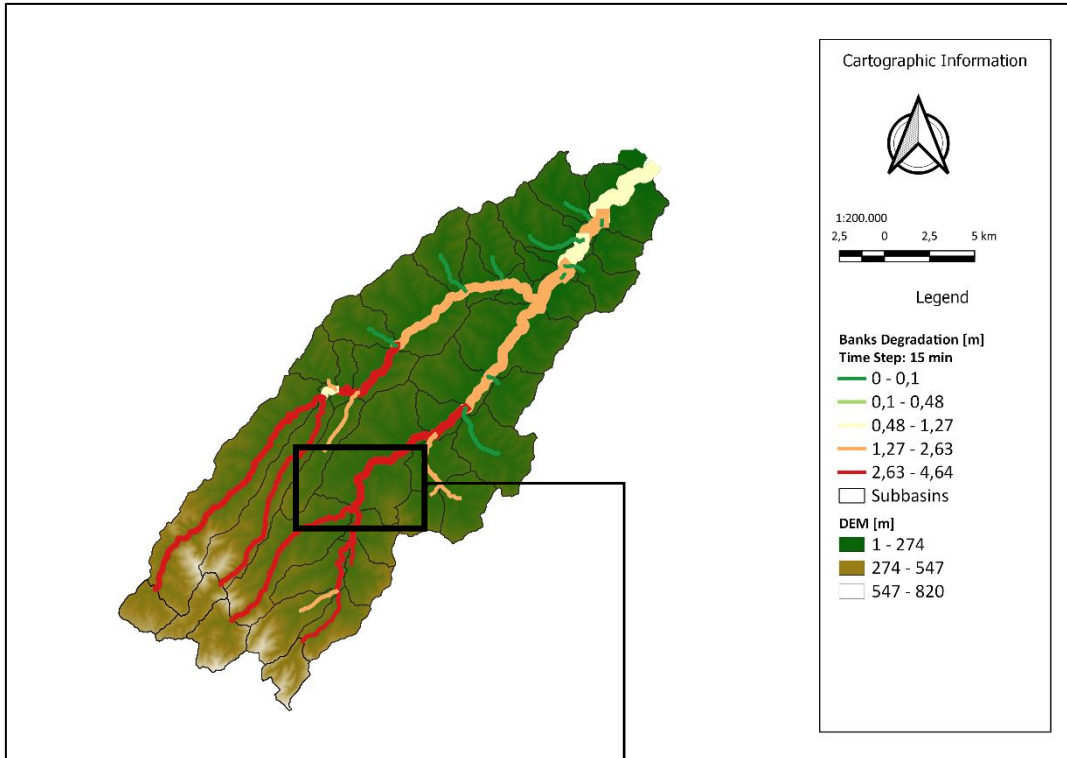


Figure 82: Banks degradation during flood event in September 2022 and photos of banks erosion.

The photos were taken near the municipality of Serra de' Conti, which is one of the centers closest to the area characterized by the highest rainfall intensity and therefore where the erosive action was most intense. The map obtained by SWAT defines a high level of bank erosion in the area, ranging from 2.63m to 4.64m. They give a range of values that have characterized erosion in the area. From the photos it is not possible to obtain extremely precise measurements, but it can be seen that the eroded part in each image is more than 2m, taking trees and houses as reference. Obviously, the values of bank erosion can vary enormously along the river shaft as there are also anthropogenic factors, such as civil and hydraulic works, which can affect the final value. Nevertheless, the result obtained by SWAT can be used as a starting point for more in-depth analyses, for example obtained with Lidar instrumentation, which through the comparison of pre and post event images allows the quantification of erosion to be precisely established.

For the geological part at the annual level, which includes analyses about erosion and sediment transport within the Misa basin from January to December, it is not possible to validate it at the quantitative level because there are no monitoring instruments in the area that can assess even partially the amount of debris moved. For this reason, monthly-level analysis of sediments-out volumes was conducted for the three years under analysis, which were compared in turn with monthly cumulative precipitation. This type of analysis makes it possible to observe the unsteady trend of erosion, which varies with rainfall amounts and the location of rainfall peaks. In fact, the Misa basin has a good variability at the level of slope, land use and soil which results in heterogeneity in erosion. Heavy rainfall in the Senigallia area will not result in high erosion in the area because the exposed land is for population centers and the slopes are almost zero. In contrast, rainfall even of moderate intensity in mountainous areas will result in an increase in erosion levels, which will also increase with a cascading effect in downstream areas. The year 2022 (Figure 47) is a perfect example that demonstrates how precipitation and its positioning determine even considerable changes in erosion levels (Figure 83). Taking September 2022, the month in which the flood occurred, as an example, we see a spike in the amounts of sediment volume produced. This is due to the intense rainfall localized almost entirely in mountainous and hilly areas, which are those most susceptible to erosion as they have areas with very exposed soil subject to moderate slopes. This led to the production of about one-third of the annual sediment in a single month. This result is also due to the scarcity of storms in the first half of the year, which resulted in very low levels of erosion from May to August. The drought combined with high temperatures resulted in extremely low flows, which lack the energy to transport sediment downstream. The same behavior is found for both bank and bed erosion (Figures 59, 60), which occur as fractions of the sediments out.

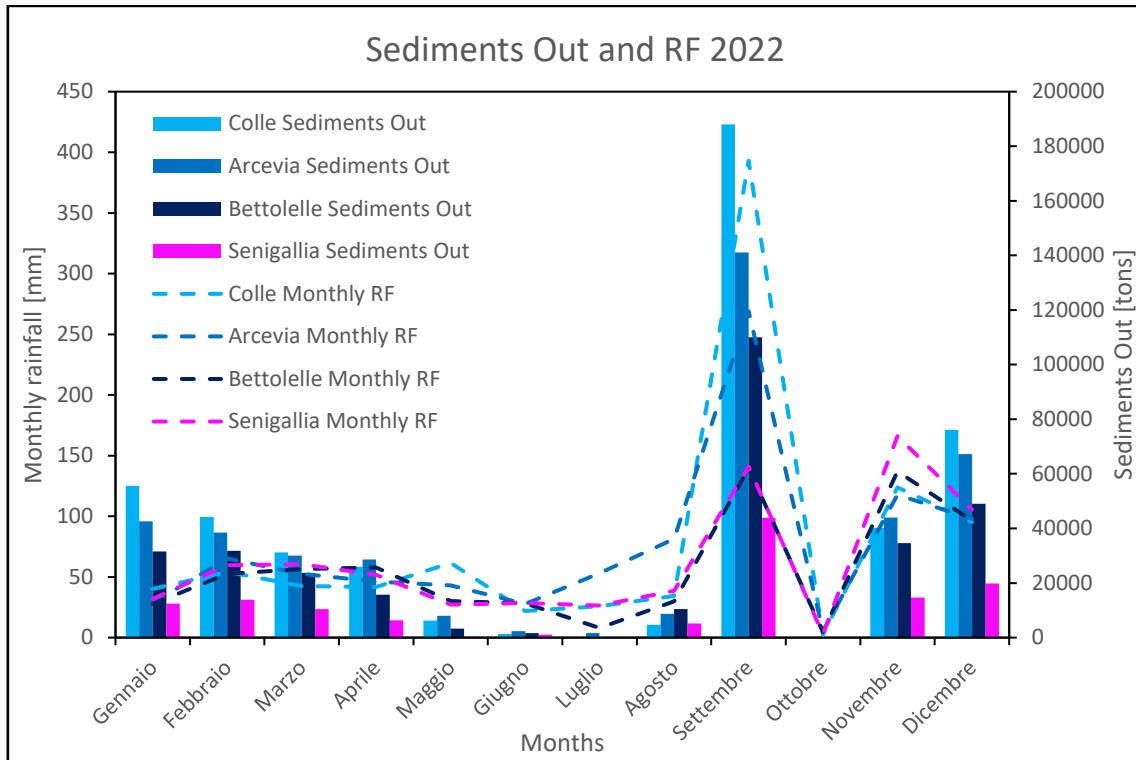


Figure 83: Comparison of monthly erosion and rainfall.

The erosional dynamics of the May 2014 event is different from the 2022 event in that the associated rainfall event is different in intensity and duration. In fact, the 2014 storm lasted for the entire day of May 3<sup>rd</sup>, and the rainfall intensity was evenly distributed throughout the basin. This results in milder but highly distributed erosion. In fact, it can be seen from the maps (Figure 64, 65, 66) that the riverbeds characterized by high levels of erosion reach all the way to the flat part of the basin, at the level of Bettollelle. Comparing the maximum erosion levels between the event values and the annual values (Figure 68) shows that 8% of the sediment is produced during the event, which is much lower than the level reached in 2022. Also comparing the annual erosion levels of 2014 and 2022 shows that although 2022 was a year with a lower annual rainfall cumulative it has higher erosion than 2014. This proves that erosion is strongly influenced by extreme events.



The year 2014, differently from 2022 is much more regular with respect to sediment distribution throughout the year (Figure 84). In fact, the highest levels are found during the winter and spring seasons when rainfall is concentrated and temperatures are low, allowing less evaporation and thus higher levels of flow within riverbeds. The action of temperature is most evident during July when, although rainfall was high, erosion amounts were lower than during the spring periods. This is due not only to temperature but also to the sporadic nature of summer storms, which also have high intensities but very short durations. Another important consideration is the one about the month of May, in which the flooding occurred. In fact, it can be seen that the event was distributed throughout the basin, starting from the most mountainous areas and ending at the outlet in Senigallia. In fact, all stations had recorded daily precipitation above 40 mm, up to a maximum of 90 mm in Corinaldo. This resulted in erosion distributed throughout the basin but not reaching 2022 levels due to lack of intensity. This did not lead to a peak in the May season, but a level that was still within the annual trend.

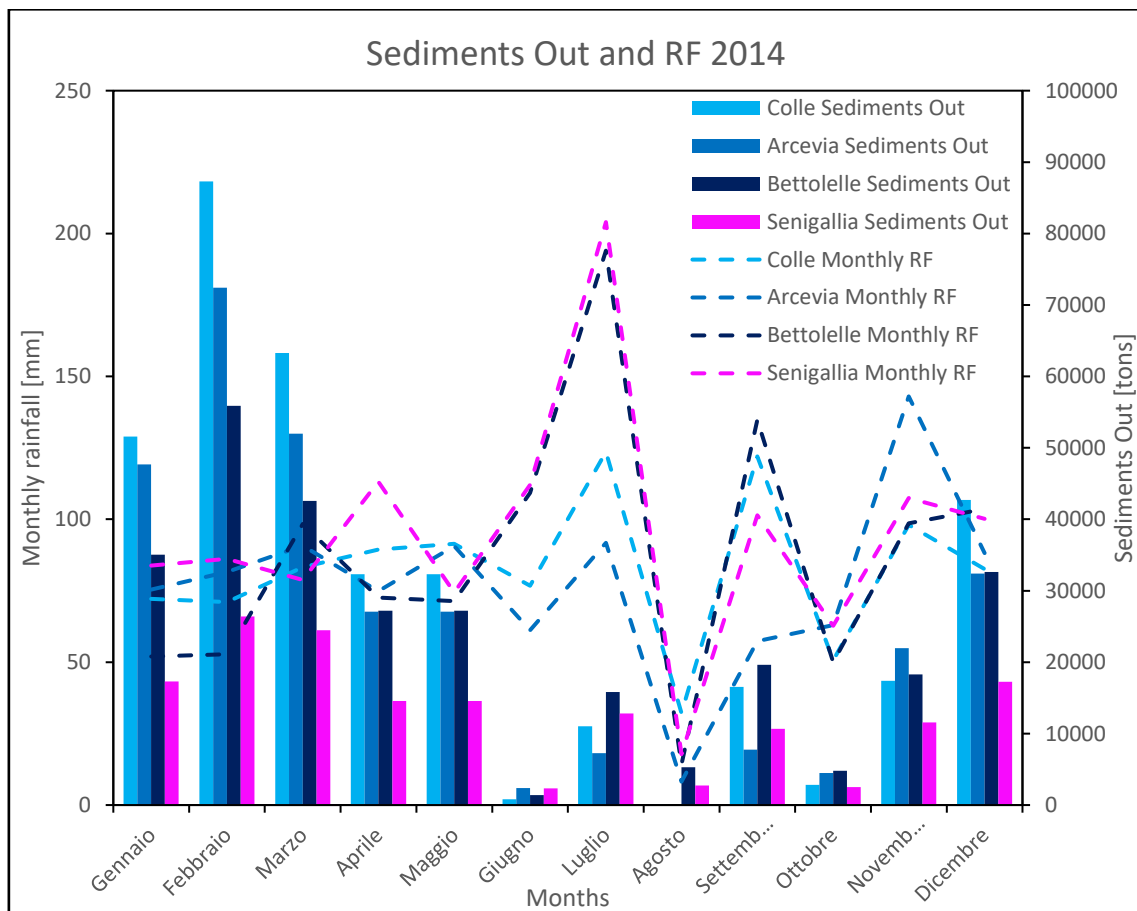


Figure 84: Comparison of monthly erosion and rainfall.

The year 2017 has high levels of sediments production (figure 85) particularly in the first months of the year since the cumulative rainfall is quite high, and looking at the daily rainfall graph (Figure 29) it can be seen that most of the storms above 30mm in the mountain range are concentrated between January and March. In particular, it is observed that values above 80000 tons are reached in February. Unlike 2014, spring was characterized by the scarcity of sediments. The recovery in production began in September, which is the month characterized by the highest amount of precipitation that has the highest intensities concentrated in the lowland areas, particularly Bettollelle and Senigallia. This leads to low sediment production, as these areas are the most urbanized and therefore it is much lower than if the same precipitation had been located in the mountainous areas inland where the availability of loose material and uncovered soil is higher.

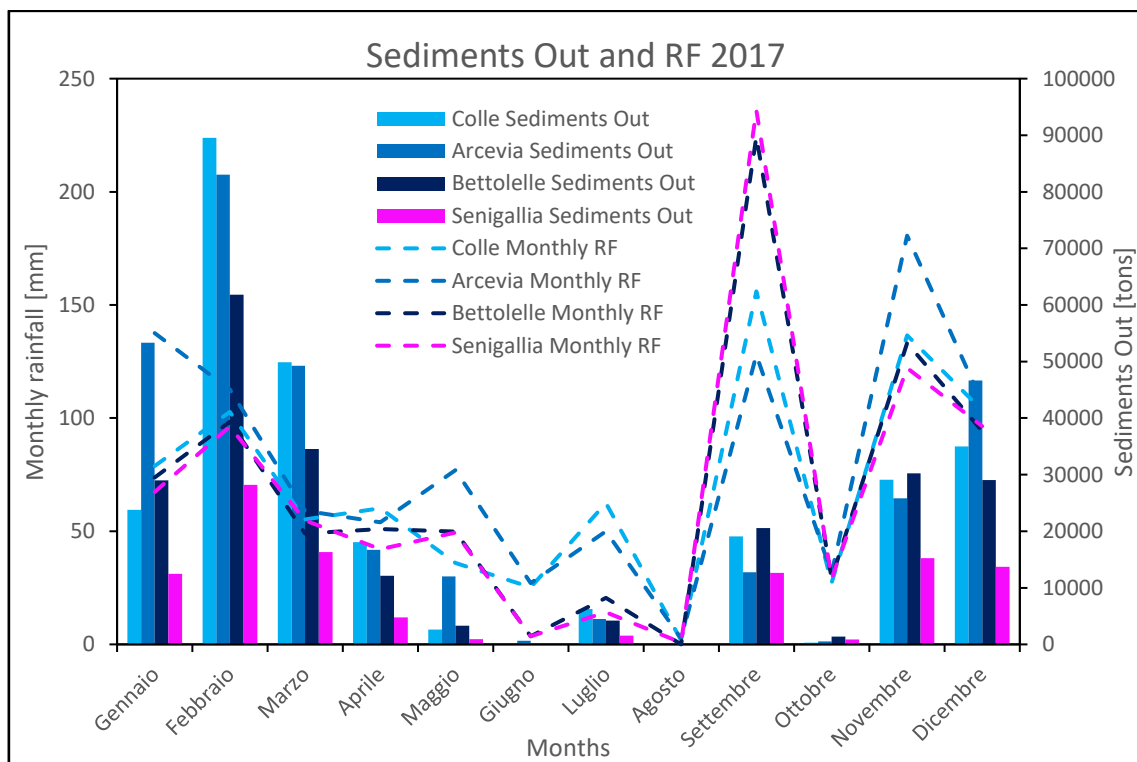


Figure 85: Comparison of monthly erosion and rainfall.

### 6.3 Climate change

The last discussion point aims to analyze the underlying causes of tropical V-shaped storm formation, which are related to climate change. The new Climate Change Report, released in 2022, (88) described the main growth trends related to climate warming. The analysis is conducted for all continents. At the European level, it is noted that extreme events have been steadily increasing since the 1950s. In Italy, there is a growing number of annual days when the temperature exceeds 40°C, leading to an increase in sea surface temperatures. In addition, there is a trend towards polarized rainfall regimes, with precipitation concentrated in distinct annual periods. This results in long periods of drought, interrupted by extremely rainy periods that resemble those found in tropical regions (88). During the autumn season, the Italian coasts are increasingly impacted by the occurrence of extreme rain events, notably due to the formation of V-shaped storms (89). These storms are named after their characteristic wedge shape, which is clearly visible in infrared satellite images (Figure 86).

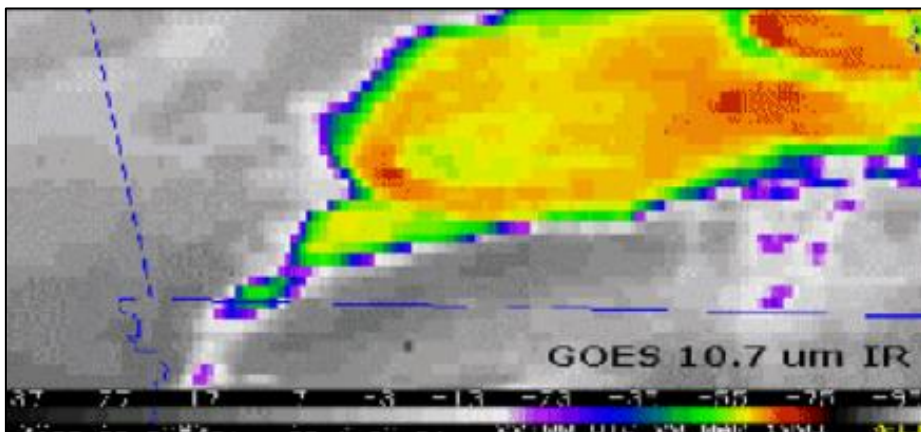


Figure 86: IR image of a V-shaped storm (90).

The cloud arrangement is due to strong updrafts that lift the clouds and cool them. This is also visible in the infrared image that shows the apex of the storm cooler than the tail. Advection currents in the troposphere then give the storm its characteristic shape. Thus, downstream of the apex, contrails with higher temperatures due to the lowering of altitude can be seen. Typically, these storms are characteristic in tropical climates where warm air masses are very energetic, due primarily to the high temperatures and large basin surfaces available (91). As atmospheric and consequently marine temperatures rise, Italy is also increasingly exposed to this type of phenomenon. In addition to the Senigallia event, there

were also other cases of V-shaped storms in Sicily, in the Messina area, and in north and central Italy, particularly in Liguria and Tuscany. The peculiarity of these phenomena is that they develop in geomorphologically similar areas, and furthermore they are all relatively recent events (92). The Sicily event dates back to November 2019, while those in Liguria and Tuscany, occurred in 2014 and 2017, respectively. The Mediterranean Sea, characterized by moderate to shallow depth and slow water circulation, is strongly influenced by global warming (93).

In order to analyze the trend of sea surface temperature (SST) over the years (94,95), two sets of data were taken into consideration. The first set refers to data provided by the National Center for Atmospheric Research and are cataloged under the name of International Comprehensive Ocean-Atmosphere Data Set (ICOADS). The series refers to a historical period of 50 years that goes from 1960 to 2010 (96). The surveys are also filtered in order to obtain SST data localized in a stretch of sea that extends between 43° and 45° of latitude and 13° and 15° of longitude (Figure 87).

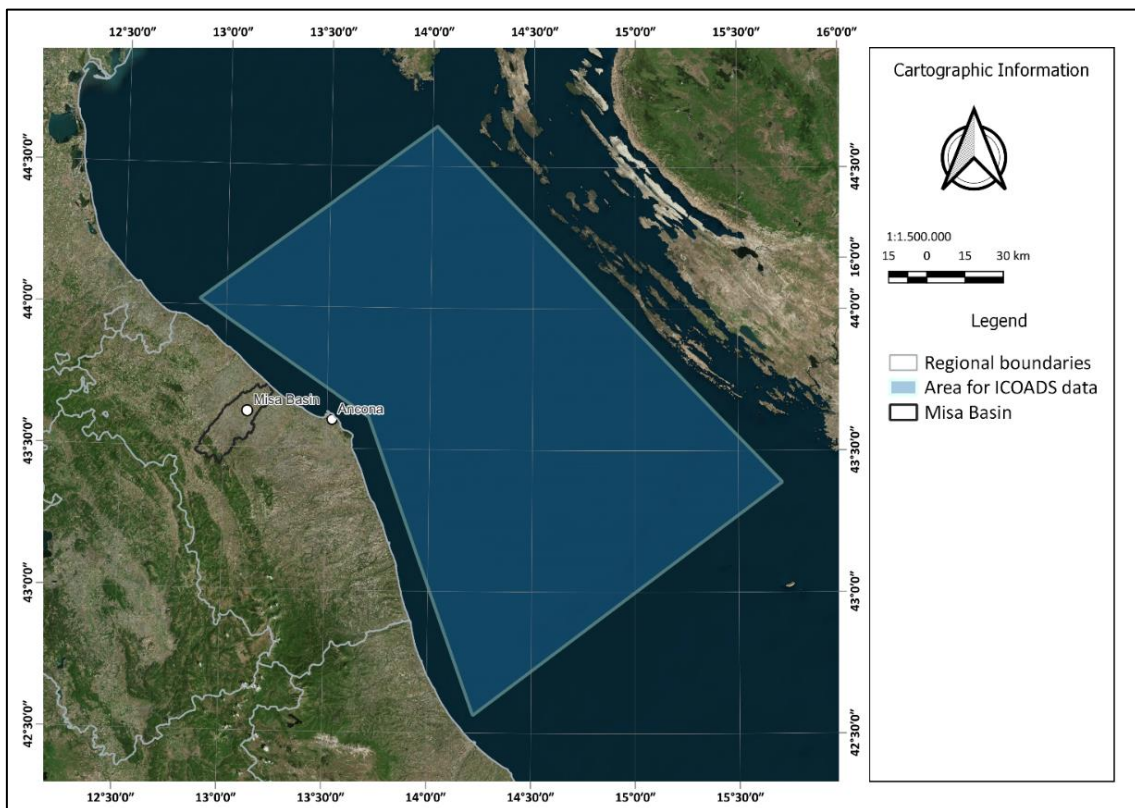


Figure 87: Locations of SST measurements.

The measurements were also filtered based on the acquisition method. In fact, the series only contains measurements made with sensors mounted on ocean-going vessels and floating buoys. Measurements obtained by remote sensing were discarded because the temperature obtained is “skin” type. This means that the measurement refers only to the first layer of the sea surface, which is most affected by external temperature and solar radiation. Therefore, the temperatures recorded will be incompatible with measurements obtained with instrumentation in direct contact with water. For this reason, they cannot be compared with each other. The temperature measured by sensors in direct contact with the water is defined as the "bulk" type (97). Considering the water-sensor system as a heat transfer system, the bulk temperature is the temperature of the mainstream of transferred heat (water in this case) in the heating unit.

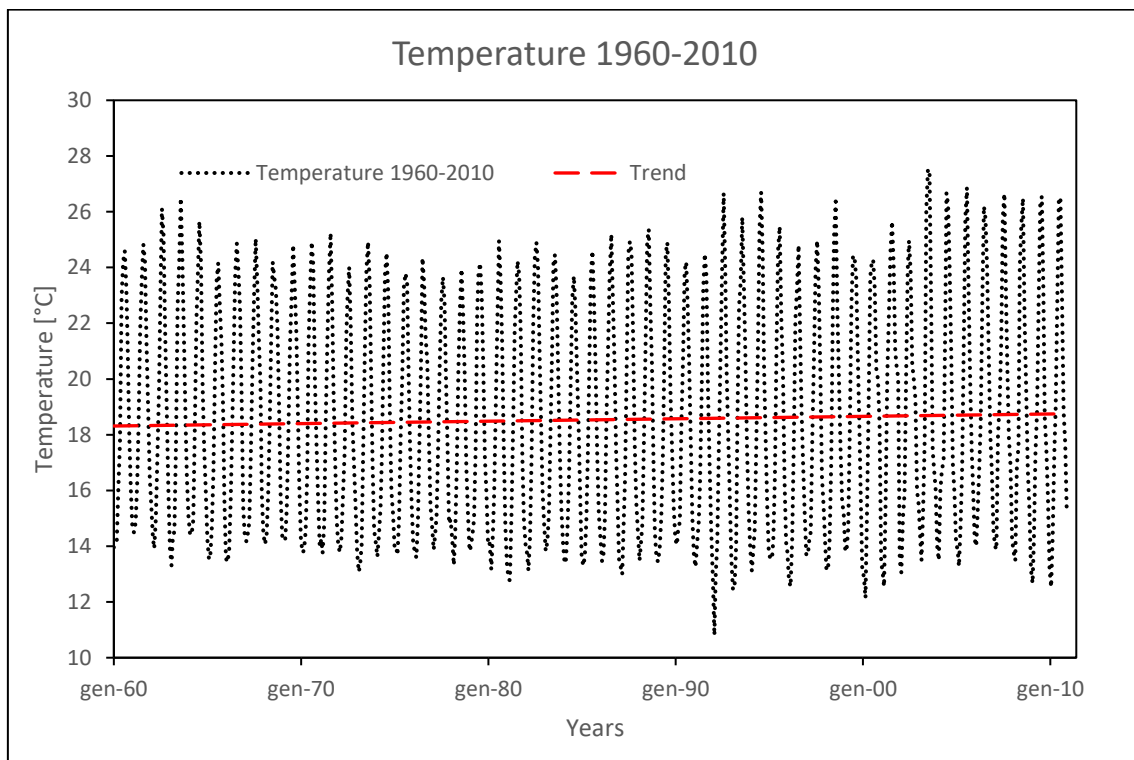


Figure 88: SST of Adriatic Sea between 1960 and 2010.

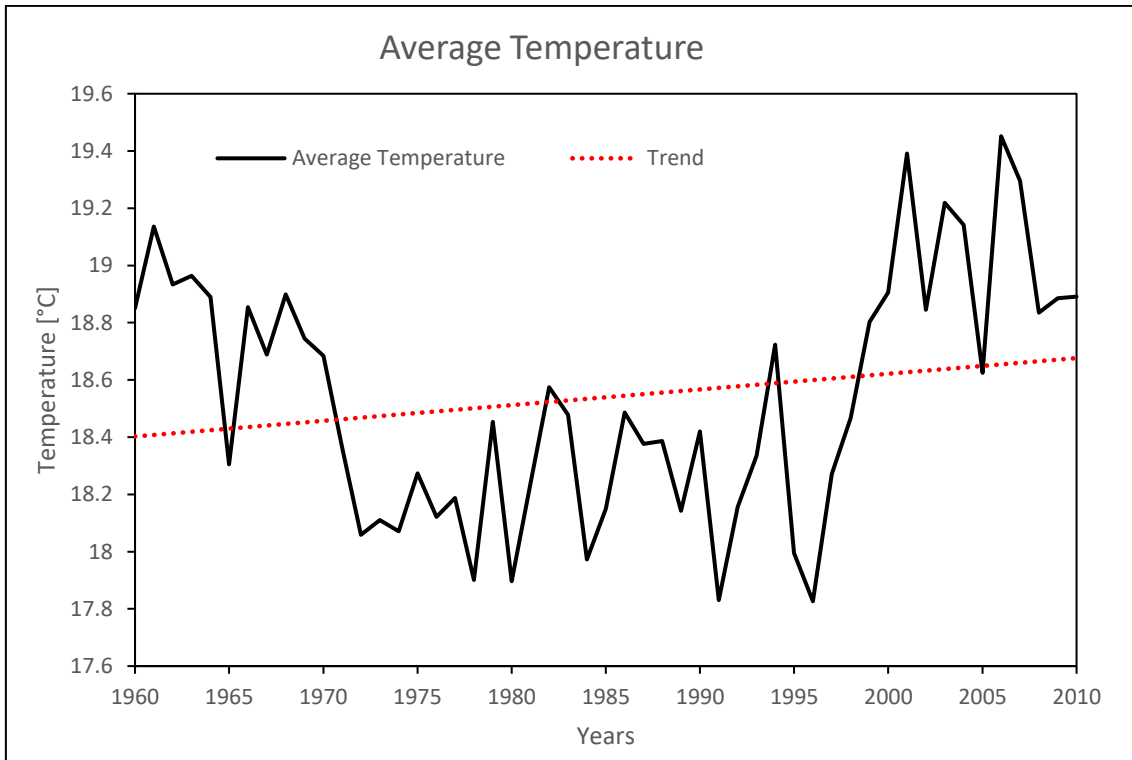


Figure 89: Average SST of Adriatic Sea between 1960 and 2010.

The graphs (Figures 88, 89) show the trend of the average monthly and yearly temperatures. Despite the drop suffered by temperatures between 1970 and 2000, the situation began to worsen dramatically between 2000 and 2010, where the maximum temperatures reached temperatures around 28°C. This sudden rise has led to a positive growth trend which stands at a value of about 0.5°C in 50 years. This increase is most noticeable when analyzing the average annual temperatures, where the growth is much more visible.

Finally, the year-by-year differences between the average annual temperature recorded and the general average of the entire series were evaluated (Figure 90). The bar graph shows positive and negative discrepancies between the two values (89).

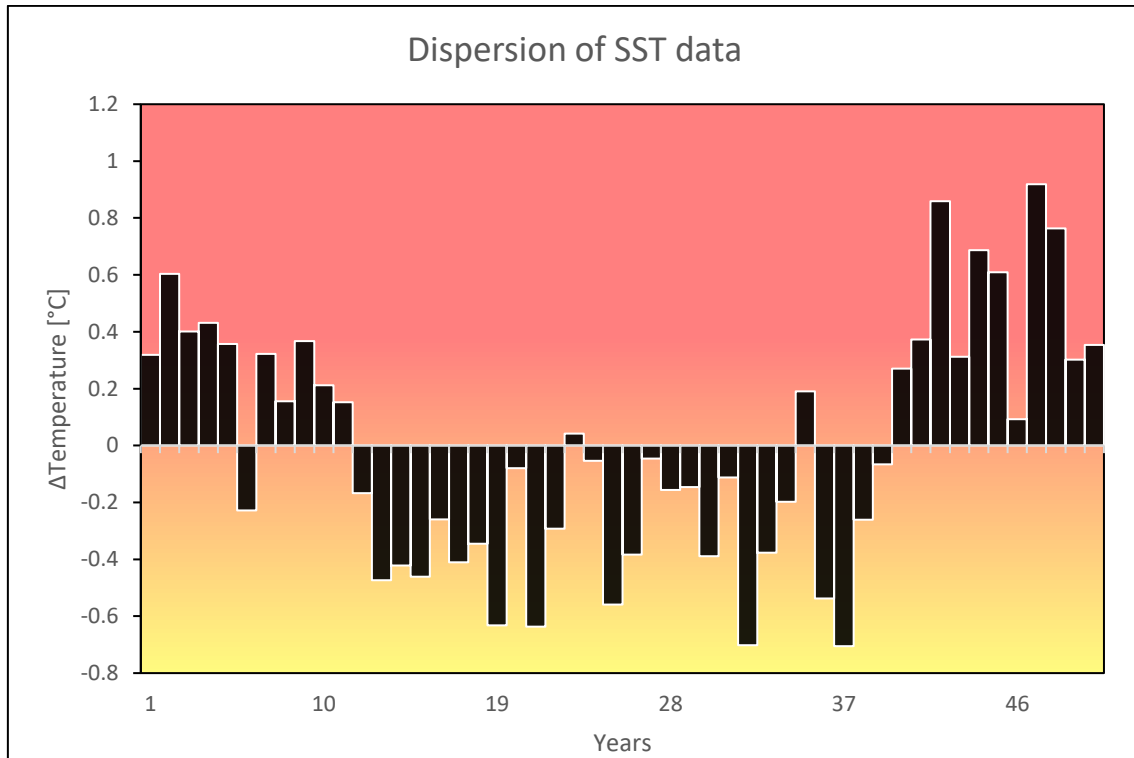


Figure 90: Dispersion of the SST temperature around the mean value.

The second series of data analyzed refers to the series of SST measurements provided by “Istituto Superiore per la Protezione e la Ricerca Ambientale (ISPRA)”, evaluated through the National Mareographic Network (RMN). It consists of 36 measurement stations located in the main Italian harbors. As for the previous series, the temperature is measured with a temperature transducer, but the substantial difference is the higher precision and continuity of the measurements, which are carried out in the same point every hour with an accuracy of 0.03°C. The station selected is the one located in the harbor of Ancona (Figure 87). The limitation of this data series is that it only covers periods starting from January 2010. In this case the series is only 12 years long.

Despite the short time window, it is possible to highlight a growing trend in average temperatures (Figure 91) and in annual maximum (Figure 92) and minimum temperatures (Figure 93). This value stands at about 0.2 °C in 10 years. The situation leads to an accentuation of the horizontal thermal gradient allowing the oceanic disturbances to reach the Italian coasts with greater energy and vigor.

Ancona Station ISPRA	2010	2011	2012	2013	2014	2015	2016	2017	2018	2019	2020	2021	2022
Average temperature [°C]	16.62	16.93	16.79	16.64	17.75	17.24	16.89	16.93	17.41	17.21	17.09	16.43	17.22
Max Value [°C]	28.20	27.90	27.80	27.50	26.80	29.00	26.00	28.30	29.10	28.40	28.10	27.30	28.40
Min Value [°C]	5.70	6.20	3.50	7.10	8.60	8.70	7.90	6.40	6.00	6.50	7.60	6.00	7.40

Table 19: Temperatures registered at the Ancona station.

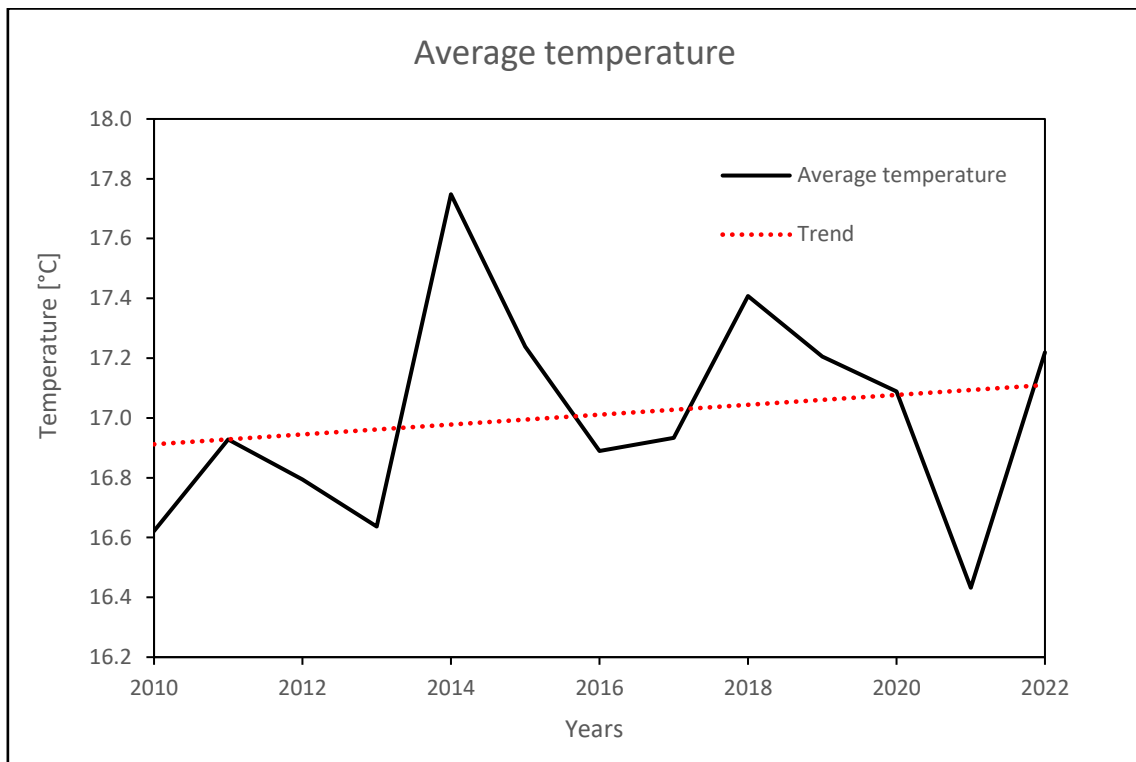


Figure 91: Average SST of Adriatic Sea between 2010 and 2022.



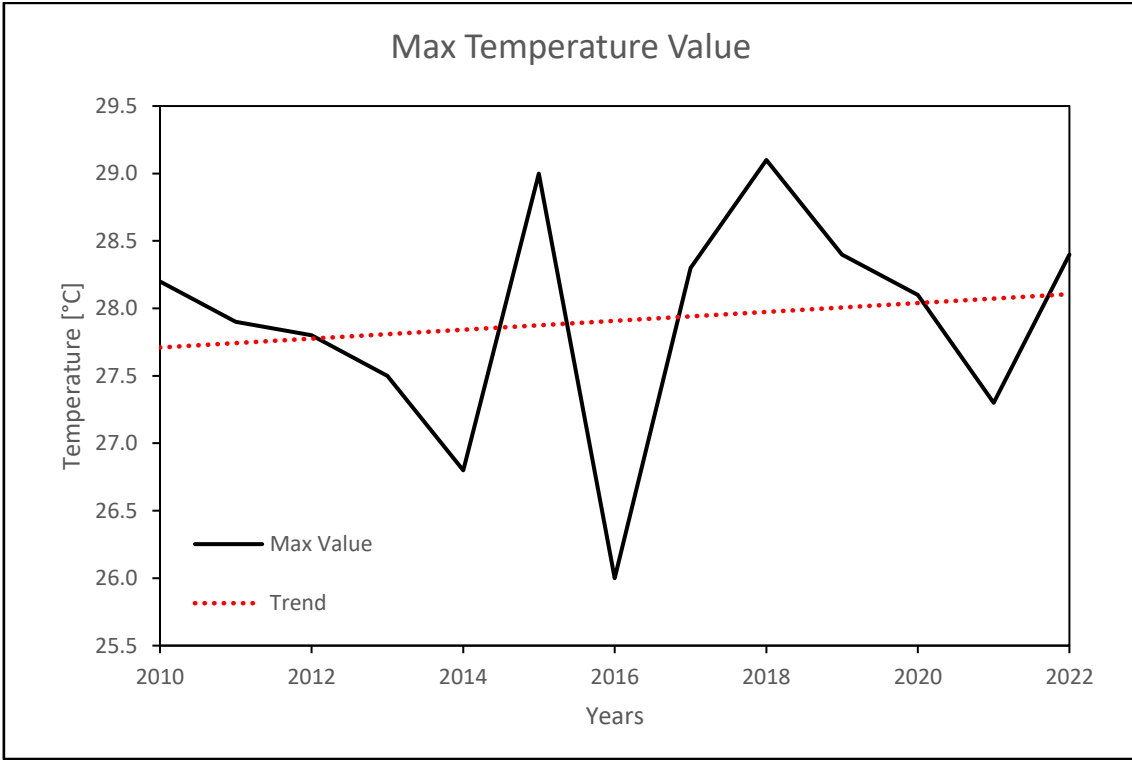


Figure 92: Max SST of Adriatic Sea between 2010 and 2022.

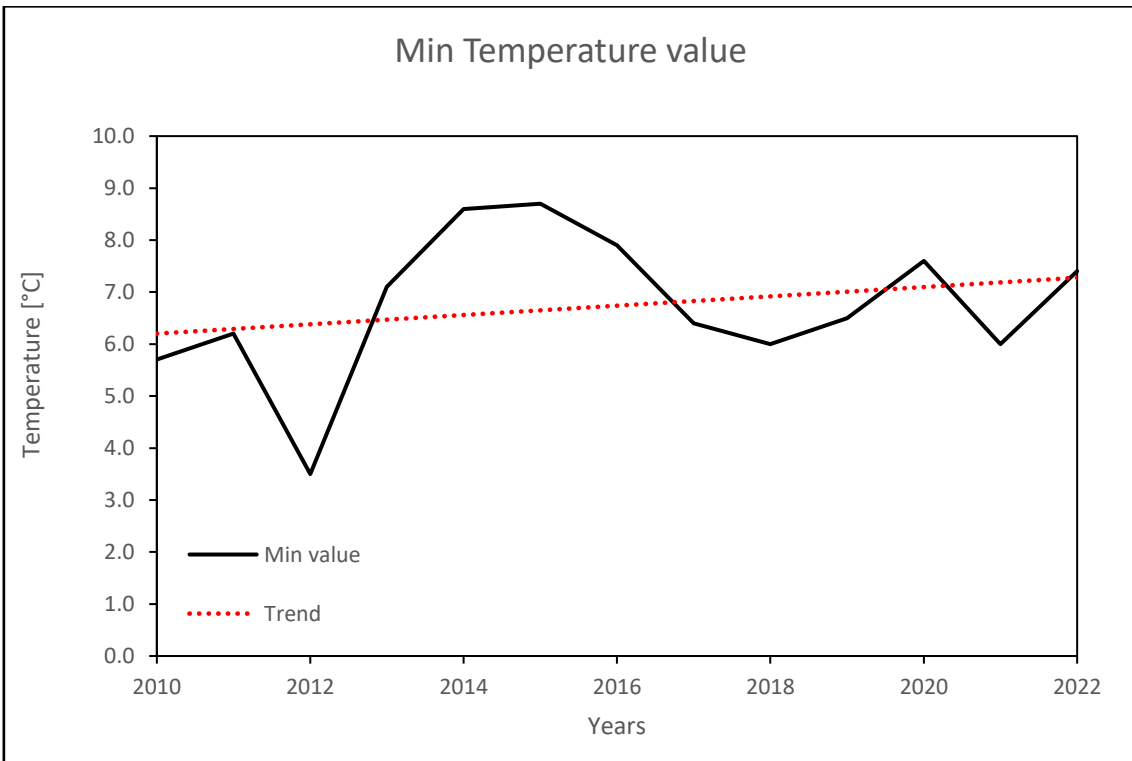


Figure 93: Min SST of Adriatic Sea between 2010 and 2022.

Higher water temperatures supply a greater quantity of energy in terms of heat and humidity, which increase the flow rate and the power of atmospheric events. Furthermore, the geomorphology (92) that characterizes the Misa basin plays a fundamental role in the generation of cyclonic eddies. In fact, when the warm air masses collide with the mountains, they rise and cool down. The presence of these cold air masses colliding with the warmer and more humid areas in the lower troposphere, typically occurring in autumn, leads to the generation of convective cells. As a result of the progressive rise in sea temperature, water bodies store more thermal energy, which enhances the feeding of these convective cells and results in stationary phenomena. In addition to that, positive wind shear, where air blows from the southeast onto the ground and from the southwest at altitude contribute to the formation of V-shaped storms (89,98).

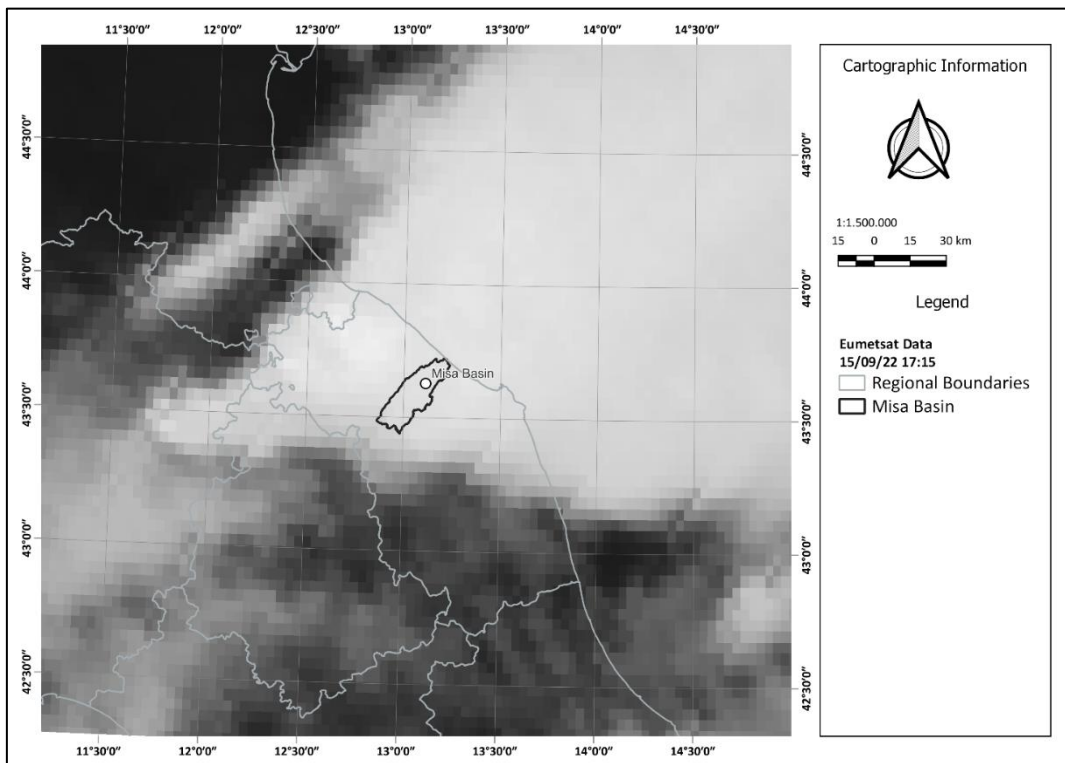


Figure 94: Eumetsat data about V-shaped storm of 15<sup>th</sup> September 2022 in Marche region.

They consist of many closely spaced cells in different evolutionary states. Viewed from a satellite, these storms appear V-shaped, with cells rapidly forming at the vertex (Figure 94), while older cells move eastward. The highest precipitation peaks are concentrated at the summit of these storms (91). The image illustrates the formation of the V-shaped storm, capturing both the vertex and the tail formation.

## 7. Conclusions

The analysis of the Misa basin yielded interesting results, both from the point of view of hydrogeological routing and thus sediment production and from the point of view of the geoclimatic situation. These two aspects are also extremely linked since erosion is a phenomenon that is extremely linked to rainfall. First of all, the SWAT software made it possible to evaluate the main hydrogeological components that characterized the Misa River. In particular the flood event of September 2022 was compared with that of May 2014, which was the last flood event up to that time. The results show that the nature of the 2022 event is totally different from that of the previous one, where 2022 event was strongly influenced by the climate change component. In fact, even if both the events led to the same inundated areas, they were different in terms of rain intensity and distribution. May 2014 was characterized by many days of heavy rainfalls, but rainfalls were regularly distributed over the year. On the other hand, 2022 was characterized by a tropical rainfall pattern, with dry spring and summer and rainfalls concentrated at the end of the year. In particular, the event of September 2022 was exceptional and with a return time of more than 1000 years in the Cantiano area and around 500 years for the municipalities of Colle and Arcevia. Despite the exceptional nature of the event, it can be seen from the rain gauge data that the annual cumulations are essentially the same for 2014 and 2022. This confirms that climate change produces a change in the annual rainfall pattern without noticeably altering the total amount of rainfall. Moreover, this extreme event was recognized to be caused by the formation of a V-shaped storm, which is characteristic of tropical climates. The increasing occurrence of these phenomena is related to the upward trend of sea surface temperature and to the geomorphology of the basins as, in this case, Misa basin is enclosed between the Apennines and the Adriatic sea. This setting favors the sudden rise and cooling of incoming air masses from the Atlantic Ocean, which generate supercells due to the clash with moist masses coming in from the sea. This should serve as a warning signal that should result in a conscious hydrogeological and spatial management of the basins. Another important consideration about the results obtained with SWAT is the validation of the data, which is closely related to the reliability of the software itself. The simulation of the hydraulic part was consistent with the situation obtained from the field data, particularly for the Bettolle station where the NSE indices were above or close to 0.5 for the 3 years considered. Despite the good

results, the validation of hydraulic results was complex because the flow rates evaluation from water height values gave numerous problems, starting from the absence of data for months at some stations, the presence of outliers, and the inaccurate definition of flow rates for dry periods. This has created significant discrepancies between observed and modeled values, particularly at the most upstream stations, where flow rates are low and where sensors are also not functioning for long periods. On the other hand, the geological part could not be validated due to the lack of data on erosion at the channel level. Nevertheless, it is noticeable that in the case of extreme events, sediment production increases exponentially. The September 2022 event produced sediment of more than 180000 tons, which is about twice the maximum volumes produced in the peak months during 2014 and 2017. This result demonstrates how extreme events can substantially change the sediment routing of a basin, and this fact can lead to even severe instability phenomena both for the slopes themselves and for all structures in the area. A final consideration in regard to the use of SWAT is its usability, particularly in regard to the factors that limit it. They are the availability of data for the basin being analyzed, as a lot of data are needed to get reliable results, and the difficulty of validating data about sediment production due to channel-level assessment, which can only be done with direct in situ monitoring. Taking into account all the analyses performed and the results obtained, important considerations can be made about the future evolution of climate and effects on the basins. If temperature growth trends continue at the same levels in the future, such events will occur with increasing frequency, and territorial preparedness has proven ineffective. The 13 casualties occurred in September 2022, still after a previous similar catastrophe, demonstrate the flaws in territorial warning systems and prevention. In this sense, physically based model models as SWAT can be a valuable tools for scenario-based simulations, serving as a starting point for future spatial planning.

## 8. Bibliography

1. Sediment Transport. (2008). In Springer eBooks (pp. 453–477). [https://doi.org/10.1007/978-0-387-68648-6\\_16](https://doi.org/10.1007/978-0-387-68648-6_16)
2. A Highly Eutrophic Lake | U.S. Geological Survey. (2016, September 22). <https://www.usgs.gov/media/images/highly-eutrophic-lake>
3. Scorpio, V., Cavalli, M., Steger, S., Crema, S., Marra, F., Zaramella, M., ... & Comiti, F. (2022). Storm characteristics dictate sediment dynamics and geomorphic changes in mountain channels: A case study in the Italian Alps. *Geomorphology*, *403*, 108173.
4. Busico, G., Colombani, N., Fronzi, D., Pellegrini, M., Tazioli, A., & Mastrocicco, M. (2020). Evaluating SWAT model performance, considering different soils data input, to quantify actual and future runoff susceptibility in a highly urbanized basin. *Journal of Environmental Management*, *266*, 110625.
5. Lenzi, M. A., D'Agostino, V., & Billi, P. (1999). Bedload transport in the instrumented catchment of the Rio Cordon: Part I: Analysis of bedload records, conditions and threshold of bedload entrainment. *Catena*, *36*(3), 171-190.
6. Turowski, J. M., Rickenmann, D., & Dadson, S. J. (2010). The partitioning of the total sediment load of a river into suspended load and bedload: a review of empirical data. *Sedimentology*, *57*(4), 1126-114
7. Carr, Meredith & Dahl, Travis. (2017). Review of Ice-Induced Scour and Impacts to Navigation and Structures. 10.21079/11681/22764.
8. Van Rijn, L. C. (1984). Sediment transport, part I: bed load transport. *Journal of hydraulic engineering*, *110*(10), 1431-1456.

9. Ouriemi, M., Aussillous, P., Medale, M., Peysson, Y., & Guazzelli, É. (2007). Determination of the critical Shields number for particle erosion in laminar flow. *Physics of Fluids*, 19(6), 061706.
10. Meyer-Peter, E., & Müller, R. (1948). Formulas for bed-load transport. In *IAHSR 2nd meeting, Stockholm, appendix 2*. IAHR.
11. Relazione Tecnica: Mitigazione del Rischio idraulico della città di Senigallia. Intervento 2: Escavo canale ed adeguamento della sezione idraulica del tratto terminale del canale della foce del fiume Misa e del ponte RFI. CUP: B13H19000070002. Ente attuatore: Consorzio di Bonifica delle Marche.
12. Smart, G. M., & Jaeggi, M. N. R. (1983). Sediment transport on steep slopes. *Mitteilungen der Versuchsanstalt für Wasserbau, Hydrologie und Glaziologie*, 64, 91-191.
13. Kuhnle, R. A. (2013). Suspended load. *Treatise on geomorphology*, 9, 124-136.
14. Jain, R. K., & Kothiyari, U. C. (2010). Influence of cohesion on suspended load transport of non-uniform sediments. *Journal of hydraulic research*, 48(1), 33-43.
15. Rijn, L. C. V. (1984). Sediment transport, part II: suspended load transport. *Journal of hydraulic engineering*, 110(11), 1613-1641.
16. Zanke, U. (1977). BERECHNUNG DER SINKGESCHWINDIGKEITEN VON SEDIMENTEN.
17. Richardson, J. T. (1954). Sedimentation and fluidization: Part I. *Trans. Inst. Chem. Engrs.*, 32, 35-52.

18. Castellort, F. X., Bladé, E., Balasch, J. C., & Ribé, M. (2020). The backwater effect as a tool to assess formative long-term flood regimes. *Quaternary international*, 538, 29-43.
19. Pickup, G., & Warner, R. F. (1976). Effects of hydrologic regime on magnitude and frequency of dominant discharge. *Journal of Hydrology*, 29(1-2), 51-75.
20. Crowder, D. W., & Knapp, H. V. (2005). Effective discharge recurrence intervals of Illinois streams. *Geomorphology*, 64(3-4), 167-184.
21. Exner, F. M. (1920), Zur physik der dünen, Akad. Wiss. Wien Math. Naturwiss. Klasse, 129(2a), 929–952.
22. Exner, F. M. (1925), Über die wechselwirkung zwischen wasser und geschiebe in flüssen, Akad. Wiss. Wien Math. Naturwiss. Klasse, 134(2a), 165–204.
23. Sleigh, Andrew & Goodwill, I. (2000). The St Venant Equations.
24. Natural Resources Conservation Service of United States Department of Agriculture. What is Soil?
25. Standards Association of Australia. AS 1289.C6.2 (1976) Determination of the Particle Size Distribution of a Soil: An Analysis by Sieving in Combination with Hydrometer Analysis.
26. Koponen, A., Kataja, M., & Timonen, J. (1997). Permeability and effective porosity of porous media. *Physical Review E*, 56(3), 3319.
27. Agriculture Victoria.gov. Soil
28. Morgan, R. P. C. (1978). Field studies of rainsplash erosion. *Earth Surface Processes*, 3(3), 295-299.

29. Ryzak, M., Bieganowski, A., & Polakowski, C. (2015). Effect of soil moisture content on the splash phenomenon reproducibility. *PLoS One*, *10*(3), e0119269.
30. Mouzai, L., & BouhadeF, M. (2011). Shear strength of compacted soil: effects on splash erosion by single water drops. *Earth Surface Processes and Landforms*, *36*(1), 87-96.
31. Qiang Dai, Estimation of rainfall erosivity based on WRF-derived raindrop size distributions, *Hydrology and Earth System Science*, 2020
32. Bazzoffi, P. (1985, March). Methods for net erosion measurement in watersheds as a tool for the validation of models in central Italy. In *Workshop on soil erosion and hillslope hydrology with emphasis on higher magnitude events, Leuven*.
33. Beyer Portner, N. (1998). *Erosion des bassins versants alpins suisses par ruissellement de surface* (No. THESIS). EPFL.
34. Li, D., Chen, X., Tao, T., Tan, W., & Ma, L. (2022). Quantifying the sheet-rill erosion process along a saturated soil slope. *Catena*, *219*, 106631.
35. Liu, G., Yang, M. Y., Warrington, D. N., Liu, P. L., & Tian, J. L. (2011). Using beryllium-7 to monitor the relative proportions of interrill and rill erosion from loessal soil slopes in a single rainfall event. *Earth Surface Processes and Landforms*, *36*(4), 439-448.
36. Natural Resources and Water (2006). What causes bank erosion?
37. Rinaldi, M., & Darby, S. E. (2007). 9 Modeling river-bank-erosion processes and mass failure mechanisms: progress towards fully coupled simulations. *Developments in Earth Surface Processes*, *11*, 213-239.



38. Fox, G. A., & Felice, R. G. (2014). Bank undercutting and tension failure by groundwater seepage: predicting failure mechanisms. *Earth Surface Processes and Landforms*, 39(6), 758-765.
39. Cruden, D. M., & Varnes, D. J. (1996). Landslide types and processes. Dalam: Turner, AK Landslides Investigation and Mitigation. Special Report.
40. Acharya, G., Cochrane, T. A., Davies, T., & Bowman, E. (2009). The influence of shallow landslides on sediment supply: A flume-based investigation using sandy soil. *Engineering Geology*, 109(3-4), 161-169.
41. Crosta, G. B., & Frattini, P. J. N. H. (2003). Distributed modeling of shallow landslides triggered by intense rainfall. *Natural Hazards and Earth System Sciences*, 3(1/2), 81-93.
42. Cevasco, A., Pepe, G., & Brandolini, P. (2014). The influences of geological and land use settings on shallow landslides triggered by an intense rainfall event in a coastal terraced environment. *Bulletin of Engineering Geology and the Environment*, 73, 859-875
43. Phillips, C., Hales, T., Smith, H., & Basher, L. (2021). Shallow landslides and vegetation at the catchment scale: A perspective. *Ecological Engineering*, 173, 106436.
44. Nettleton, I. M., Martin, S., Hencher, S., & Moore, R. (2005). Debris flow types and mechanisms. *Scottish road network landslides study*, 45-67.
45. Armanini, A., Dalri, C., & Larcher, M. (2006). Slit-check dams for controlling debris flow and mudflow. In *International Symposium Disaster Mitigation of Debris Flows, Slope Failures and Landslides*, Universal Academy Press, Inc (pp. 141-148).

46. Longoni, L., Ivanov, V. I., Brambilla, D., Radice, A., & Papini, M. (2016). Analysis of the temporal and spatial scales of soil erosion and transport in a mountain basin. *Italian Journal of Engineering Geology and Environment*, 16(2), 17-30.
47. Sarkar, T., & Tapas, P. (2021). Revisiting the methodological development in soil erosion research. *Ensm.*, 2, 145-165.
48. Myers, D. T., Rediske, R. R., & McNair, J. N. (2019). Measuring streambank erosion: A comparison of erosion pins, total station, and terrestrial laser scanner. *Water*, 11(9), 1846.
49. Kearney, S. P., Fonte, S. J., García, E., & Smukler, S. M. (2018). Improving the utility of erosion pins: absolute value of pin height change as an indicator of relative erosion. *Catena*, 163, 427-432.
50. Sirvent, J., Desir, G., Gutierrez, M., Sancho, C., & Benito, G. (1997). Erosion rates in badland areas recorded by collectors, erosion pins and profilometer techniques (Ebro Basin, NE-Spain). *Geomorphology*, 18(2), 61-75.
51. Benito, G., Gutie, M., & Sancho, C. (1992). Erosion rates in badland areas of the central Ebro Basin (NE-Spain). *Catena*, 19(3-4), 269-286.
52. Hancock, G. R., & Lowry, J. B. C. (2015). Hillslope erosion measurement—a simple approach to a complex process. *Hydrological Processes*, 29(22), 4809-4816.
53. Haigh, M. J. (1977). The use of erosion pins in the study of slope evolution. *British Geomorphological Research Group Technical Bulletin*, 18, 31-49.
54. Rueda, E. B., & Moreira, R. P. (1987). Evaluation of the USLE for the prediction of erosion in burnt forest areas in Galicia (NW Spain). *Catena*, 14(1-3), 189-199.

55. Hancock, G. R., Murphy, D., & Evans, K. G. (2010). Hillslope and catchment scale soil organic carbon concentration: An assessment of the role of geomorphology and soil erosion in an undisturbed environment. *Geoderma*, 155(1-2), 36-45.
56. Zhang, N., & Rutherford, I. D. (2020). The effect of instream logs on river-bank erosion: Field measurements of hydraulics and erosion rates. *Earth surface processes and landforms*, 45(7), 1677-1690.
57. Longoni, L., Papini, M., Brambilla, D., Barazzetti, L., Roncoroni, F., Scaioni, M., & Ivanov, V. I. (2016). Monitoring riverbank erosion in mountain catchments using terrestrial laser scanning. *Remote Sensing*, 8(3), 241.
58. Thoma, D. P., Gupta, S. C., Bauer, M. E., & Kirchoff, C. E. (2005). Airborne laser scanning for riverbank erosion assessment. *Remote sensing of Environment*, 95(4), 493-501.
59. Jugie, M., Gob, F., Vermoux, C., Brunstein, D., Tamisier, V., Le Coeur, C., & Grancher, D. (2018). Characterizing and quantifying the discontinuous bank erosion of a small low energy river using Structure-from-Motion Photogrammetry and erosion pins. *Journal of hydrology*, 563, 418-434.
60. Robert P. Stone, Universal Soil Loss Equation (USLE), *Kings Printer for Ontario*, 2016.
61. Wischmeier, W. H., & Smith, D. D. (1965). Predicting rainfall-erosion losses from cropland east of the Rocky Mountains.
62. Wischmeier, W. H., & Smith, D. D. (1978). *Predicting rainfall erosion losses: a guide to conservation planning* (No. 537). Department of Agriculture, Science and Education Administration.

63. Renard, K. G., Foster, G. R., Weesies, G. A., & Porter, J. P. (1991). RUSLE: Revised universal soil loss equation. *Journal of soil and Water Conservation*, 46(1), 30-33.
64. Renard, K. G., & Ferreira, V. A. (1993). RUSLE model description and database sensitivity. *Journal of environmental quality*, 22(3), 458-466.
65. Williams, J. R. (1974). SEDIMENT-YIELD PREDICTION WITH UNIVERSAL EQUATION USING RUNOFF ENERGY FACTOR<sup>1</sup>. *ARS-S.*, (40-49), 244.
66. Williams, J. R. (1975). Sediment routing for agricultural watersheds 1. *JAWRA Journal of the American Water Resources Association*, 11(5), 965-974.
67. Agricultural Research Service, USLE History, *National Soil Erosion Research Laboratory: West Lafayette, IN*, 2016
68. Gavrilovic, S. (1976). Bujicni tokovi i erozija (Torrents and erosion) Gradevinski kalendar. *Beograd, Serbia*.
69. Dragičević, N., Karleuša, B., & Ožanić, N. (2017). Erosion potential method (Gavrilović Method) sensitivity analysis. *Soil and Water Research*, 12(1), 51-59.
70. Neitsch, S. L., Arnold, J. G., Kiniry, J. R., & Williams, J. R. (2011). *Soil and water assessment tool theoretical documentation version 2009*. Texas Water Resources Institute.
71. Montrasio, L., & Valentino, R. (2008). A model for triggering mechanisms of shallow landslides. *Natural Hazards and Earth System Sciences*, 8(5), 1149-1159.
72. Takahashi, T. (2009). A review of Japanese debris flow research. *International Journal of Erosion Control Engineering*, 2(1), 1-14.

73. Regione Marche, Autorità di Bacino Regionale. Piano di Assetto Idrogeologico (PAI), Norme di Attuazione (NA).
74. Autorità di Bacino regionale delle Marche. Delibera n.67 del 25 marzo 2016.
75. ANSA.it, Marche. Firmato verbale consegna lavori vasche di espansione Senigallia.
76. Ingemi, D. (2022, September 16). L'alluvione nelle Marche è stata causata da un fiume atmosferico tropicale.
77. Irpi. (2022). 15 settembre 2022: le vittime dell'alluvione nelle Marche. *Polaris*.
78. Guglielmo, G., Verdicchio, D. (2022). Analisi statistica dell'evento pluviometrico del 15 settembre 2022 nella regione Marche.
79. Regione Marche, Centro Funzionale Meteorologia, Idrologia e sismologia. ALLEGATO 2\_A-rapporto finale Aspigo. Curve di Possibilità pluviometrica. Ancona Torrette, Osimo, Baraccola, Recanati
80. Leadbetter, M. R., Lindgren, G., & Rootzén, H. (2012). *Extremes and related properties of random sequences and processes*. Springer Science & Business Media.
81. Overeem, A., Buishand, A., & Holleman, I. (2008). Rainfall depth-duration-frequency curves and their uncertainties. *Journal of Hydrology*, 348(1-2), 124-134.
82. Catanzariti, F. (2021). Curve di Probabilità Pluviometrica: come ricavarle? GoMeeting Interactive Formation.

83. Tarboton, D. G. (2005). Terrain analysis using digital elevation models (TauDEM). *Utah State University, Logan, 3012*, 2018.
84. García-Ruiz, J. M. (2010). The effects of land uses on soil erosion in Spain: A review. *Catena*, *81*(1), 1-11.
85. FAO - Unesco Soil map of the world. 1: 5 000 000 - Volume V Europe. Prepared by the Food and Agriculture Organization of the United Nations. FAO/Unesco 1981, ISBN 92-3-101364-0
86. Obregón, M. Á., Rodrigues, G., Costa, M. J., Potes, M., & Silva, A. M. (2019). Validation of ESA Sentinel-2 L2A aerosol optical thickness and columnar water vapour during 2017–2018. *Remote Sensing*, *11*(14), 1649.
87. McCuen, R. H., Knight, Z., & Cutter, A. G. (2006). Evaluation of the Nash–Sutcliffe efficiency index. *Journal of hydrologic engineering*, *11*(6), 597-602.
88. Pörtner, H. O., Roberts, D. C., Tignor, M., Poloczanska, E., Mintenbeck, K., Alegría, A., ... & Rama, B. (2022). IPCC 2022: Climate Change 2022: impacts, adaptation and vulnerability: working group II contribution to the sixth assessment report of the intergovernmental panel on climate change.
89. Castorina, G., Semprebello, A., Insinga, V., Italiano, F., Caccamo, M. T., Magazù, S., ... & Rizza, U. (2023). Performance of the WRF Model for the Forecasting of the V-Shaped Storm Recorded on 11–12 November 2019 in the Eastern Sicily. *Atmosphere*, *14*(2), 390

90. UW-Madison Satellite Meteorology: Lesson 10 Background. (n.d.). <http://itg1.meteor.wisc.edu/wxwise/satmet/lesson10/background10.html>
91. McCann, D. W. (1983). The enhanced-V: A satellite observable severe storm signature. *Monthly Weather Review*, *111*(4), 887-894.
92. Zoccatelli, D., Borga, M., Viglione, A., Chirico, G. B., & Blöschl, G. (2011). Spatial moments of catchment rainfall: rainfall spatial organisation, basin morphology, and flood response. *Hydrology and Earth System Sciences*, *15*(12), 3767-3783.
93. Orlic, M., Gacic, M., & Laviolette, P. E. (1992). The currents and circulation of the Adriatic Sea. *Oceanologica acta*, *15*(2), 109-124.
94. Grbec, B., Matic, F., Paklar, G. B., Morović, M., Popović, R., & Vilibić, I. (2019). Long-term trends, variability and extremes of in situ sea surface temperature measured along the eastern Adriatic coast and its relationship to hemispheric processes. *Meteorology and Climatology of the Mediterranean and Black Seas*, 311-326.
95. Mar Adriatico: cent'anni di riscaldamento | Consiglio Nazionale delle Ricerche.
96. Talluri, M. (2019, April 30). Marco Talluri. <https://www.snpambiente.it/2019/04/30/le-temperature-dei-mari-italiani-dal-1900-ad-oggi/>
97. Schluessel, P., Emery, W. J., Grassl, H., & Mammen, T. (1990). On the bulk-skin temperature difference and its impact on satellite remote sensing of sea surface temperature. *Journal of Geophysical Research: Oceans*, *95*(C8), 13341-13356.

98. Cohuet, J. B., Romero, R., Homar, V., Ducrocq, V., & Ramis, C. (2011). Initiation of a severe thunderstorm over the Mediterranean Sea. *Atmospheric Research*, *100*(4), 603-620.



# 9. Appendix

## Appendix A: Legend of the geological map from CARG project for Figure 17

CARTOGRAFIA DI BASE	
	URBANIZZATO (agg. 2010)
	CURVE DI LIVELLO (equidistanza 100m)
	IDROGRAFIA PRINCIPALE
	LIMITE PROVINCIALE
	LIMITE REGIONALE
	LIMITE DI STATO
	STRADE PROVINCIALI
	STRADE STATALI
	FERROVIE
	AUTOSTRADE
	99 Lago
LITOLOGIA	
	1 Movimento franoso Olocene
	2 Depositi alluvionali terrazzati attuali e recenti. Olocene
	3 Depositi di spiaggia Olocene
	4 Depositi di versante Pleistocene medio-somitale - Olocene
	5 Travertini Pleistocene sup. - Olocene
	6 Depositi lacustri Pleistocene medio - Olocene
	7 Depositi alluvionali terrazzati antichi Pleistocene inf. - sup.
	8 Depositi morenici. Pleistocene sup.
	9 Depositi di glacis antichi. Pleistocene inf./medio - medio
	10 Elementi antropici
SUCCESIONE EPILOGURE	
	11 FORMAZIONE DI CASA MONTE SABATINO La Formazione presente in carta è il risultato di accorpamenti tra due litofacies rappresentati da poligoni di dimensioni esigue. Arenarie grigio-giallastre e conglomerati poligenici in potenti banchi a geometria lenticolare. Potenza circa 100m. Messiniano sup. (?) - Pliocene basale
	12 GRUPPO GESSOSO-SOLFIFERA Gessi microcristallini biancastri con intercalazioni pelitiche e gessi macrocristallini spesso geminati a ferro di lancia in strati o bancconi di 5-6 m alternati a potenti pacchi di peliti bituminose nere. Messiniano superiore
	13 ARGILLE DI CASA I GESSI Argille siltose grigio scure talvolta con macrofossili e lignite, generalmente a stratificazione indistinta con rari e sottili strati marnosi. Messiniano inf.
	14 FORMAZIONE DI AQUAVIVA Arenarie grigio-giallastre bioturbate e con strutture sedimentarie, in strati generalmente massivi e banchi. Sono presenti subordinati livelli conglomeratici e pelitici bituminosi. Abbondanti resti fossili concentrati in livelli di tritume conchigliare sparsi oltre a resti di frustoli carboniosi. Tortoniano-Messiniano inf.
	15 FORMAZIONE DI S. MARINO Calcarei organogeni grigi e calcareniti ricche in bioclasti. Calcarenite intensamente bioturbate a stratificazione concavo-convessa, talora parallela. Potenza variabile fino a 200m. Burdigaliano sup. - Langhiano inf.
	16 MEMBRO DI S. ALBERICO Biocalcarei ed arenarie ibride di colore grigio verdastre. Spessore di alcune decine di metri.
	31 FORMAZIONE DELLA LAGA MEMBRO EVAPORITICO Arenarie da medio-grossolane a fini, scarsamente cementate a stratificazione da molto spessa a media con a luoghi livelli pelitici. Localmente sono presenti sottili intercalazioni discontinue di gessi ricristallizzati. Messiniano p.p.
	32 FORMAZIONE DELLA LAGA MEMBRO PREEVAPORITICO Torbidi arenacee (talora conglomeratiche), arenaceo-pelittiche, pelitico-arenacee e pelitiche. Messiniano p.p.
	33 FORMAZIONE DI S. DONATO Depositi torbiditici caratterizzati da areniti alternati a marne, marne argillose e marne siltose di colore grigio azzurro. Messiniano p.p.
	34 ARENARIE DI SERRASPINOSA Arenarie medio-fini in strati spessi, alternate a marne siltose. Serravalliano p.p. - Messiniano p.p.
	35 GRUPPO GESSOSO-SOLFIFERO Presenti le facies primarie con marne tripolacee, "calcicare di base", gessi laminati, gessi nodulari biancastri e gessi massivi microcristallini. Le facies risedimentate sono rappresentate da marne e argille bituminose laminate con rare intercalazioni di gesso-areniti, gesso-silitti e diatomitici. Messiniano p.p.
	36 FORMAZIONE DI CAMERINO Torbidi pelitico-arenacee e pelitiche, arenaceo-pelittiche e arenaceo-conglomeratiche, con rapporti di sovrapposizione e laterali. Tortoniano p.p. - Messiniano p.p.
	37 MARNE A PTEROPODI Marne e calcari marnosi empelagici con abbondante fauna a foraminiferi planctonici. Tortoniano - Messiniano
	38 TRIPOLI E MARNE TRIPOLACEE Alternanza di sottili strati di areniti, silt, marne, marne siltose scure e marne diatomitiche e diatomiti candide finemente laminate (s.s. tripoli). Abbondanti resti fossili. Tortoniano - Messiniano
	39 FORMAZIONE MARNOSA ARENACEA MARCHIGIANA MEMBRO DI URBINO Alternanza arenaceo-pelittico in strati da sottili a molto spessi. Le arenarie da fini a grossolane spesso poco cementate, con gradazione scarsa o assente. Pelitici spesso siltose e marnose sottilmente laminate. Spessore massimo 350 m. Tortoniano - Messiniano inf.
	40 FORMAZIONE MARNOSA ARENACEA MARCHIGIANA MEMBRO DI S. ANGELO IN VADO Alternanza di arenarie massive gradate e in strati medio-spessi e peliti date da siltiti torbiditiche ed empelagiti siltoso-marnose. Lo spessore complessivo è di circa 650m. Tortoniano
	41 FORMAZIONE MARNOSA ARENACEA ROMAGNOLA MEMBRO DI ARENARIE DI CIVITELLA Torbidi pelitico-arenacee e rare empelagiti. Serravalliano medio- Tortoniano inf.
	42 FORMAZIONE MARNOSA ARENACEA ROMAGNOLA MEMBRO DI COLLINA Alternanza di peliti, arenarie, talora calcareniti (colombine) ed empelagiti con A/P < 1/3 generalmente = 1/5; le areniti sono organizzate in letti sottili e medi, raramente spessi. Serravalliano-Tortoniano
	43 FORMAZIONE MARNOSA ARENACEA ROMAGNOLA MEMBRO DI GALEATA Peliti ed arenarie (A/P medio da 1/4 a 1/5), arenarie gradate in strati da sottili a molto spessi, calcareniti "colombine" in strati da 40 a 120 cm di spessore ed empelagiti, talvolta areniti ibride in strati da 30 a 80 cm. Serravalliano-Tortoniano
	44 FORMAZIONE MARNOSA ARENACEA ROMAGNOLA MEMBRO DI CORNOLO Peliti ed arenarie (A/P medio 1/5). Arenarie gradate da medio a fini, in strati da sottili a spessi, talvolta molto spessi; rare areniti ibride ed empelagiti. Serravalliano-Tortoniano
	45 FORMAZIONE MARNOSA ARENACEA UMBRA MEMBRO DI VESINA Torbidi pelitico arenacee (A/P = 1/2- 1/5) silicoclastiche in strati spessi nella parte basale, medi verso alto. Massimo spessore affiorante circa 450m. Langhiano p.p.
	46 FORMAZIONE MARNOSA ARENACEA UMBRA MEMBRO DI MONTE CASALE Torbidi arenaceo pelitiche (A/P > 1) silicoclastiche con strati arenacei molto spessi frequentemente amalgamati e a grana grossolana. Il colore delle arenarie è marrone se alterate e grigio chiaro al taglio fresco. Spessore del membro circa 450 m. Langhiano p.p.
	47 FORMAZIONE MARNOSA ARENACEA UMBRA MEMBRO DI CASA SPERTAGLIA Torbidi arenaceo pelitiche (A/P = 1/3-1/4) silicoclastiche a grana media in strati da medi a spessi. La parte pelitica è costituita da marnosiltiti grige. Massimo spessore affiorante circa 300 m. Burdigaliano p.p. - Langhiano p.p.
SUCCESIONE CALCAREO E/O MARNOSA CRETACICO - MIOCENICA	

UNITÀ LIGURI

**17** **FORMAZIONE DI MONTE MORELLO**  
 Alternanze di calcari e calcari marnosi calcarenitiche torbiditiche e marne. I calcari hanno colore grigio chiaro e strati medio e spessi. Le marne e le marne calcaree hanno una stratificazione sottile e colori che variano dal nocciola al grigio scuro piuttosto fogliettate.  
 Spessore di circa 700m.  
 Eocene inf.-medio

**18** **FORMAZIONE DI SILLANO**  
 Alternanze di strati di vario spessore (da decimetrico a metrico) di peliti grigie e calcari grigio verdastri. Peliti avana o talvolta policrome specialmente nella parte basale dove prevalgono sui calcari, con marne calcaree rosate ed arenarie fini. La porzione carbonatica è rappresentata da calcareniti torbiditiche a grana fine, calcilutiti in strati da medi a spessi e calcari marnosi. Potenza variabile da pochi metri a 350 m.  
 Cretacico sup.- Eocene inf

**19** **ARGILLE VARICOLORI**  
 Argille e argilliti policrome associate a subordinati e discontinui livelli di calcareniti e calcilutiti di colore grigio-verdastre, siltiti di colore marrone scuro-rossastro e marne grigio-avana. Difficile valutare lo spessore a causa dell'assetto fortemente caotico della formazione.  
 Cretacico inf.- Eocene inf

SUCCESSIONE UMBRO-MARCHIGIANA-ROMAGNOLA

**20** **FEM- FORMAZIONE DI FERMO**  
 Arenarie e conglomerati, subordinatamente limi e limi sabbiosi con geometrie e rapporti reciproci piuttosto variabili. Sul terreno sono riscontrabili diverse litofacies non cartografabili alla scala del presente lavoro. Spessore massimo di 40m.  
 SICILIANO

**21** **ARGILLE AZZURRE**  
 Peliti, peliti siltose di colore grigio-azzurro in strati, da sottili a medi, poco evidenti e marcati da interstrati di arenarie giallastre e argille siltose. Sono ricche in foraminiferi e macrofossili. All'interno dell'unità si riscontrano corpi arenacei alla base mentre al tetto corpi pelitici. Lo spessore supera i 1000 m.  
 Pliocene Inferiore- Pleistocene Inferiore

**22** **MEMBRO DI M. CALVO IN FOGLIA**  
 Alternanza di arenarie e argille fossilifere in livelli continui o lenticolari. Spessore massimo 450m.  
 Pliocene inf. medio

**23** **MEMBRO DI OFFIDA**  
 Prevalenti peliti massive grigio azzurre intercalate a diversa altezza stratigrafica da corpi e/o orizzonti pelitico/arenacei e arenaceo/pelitici.  
 Zancleano p.p.- Santemiano

**24** **MEMBRO DEL M. DELL'ASCENSIONE**  
 Varie associazioni spesso in eteropia tra loro: da conglomeratica a pelitico arenacea.  
 Spessore fino a 1000m  
 Zancleano p.p.- Santemiano

**25** **MEMBRO DELLO SPUNGONE**  
 Prevalente associazione arenacea caratterizzata da una intensa bioturbazione e dalla presenza di orizzonti bioclastici, passante lateralmente ad un'associazione arenaceo pelitica. Spessore fino a 180 m.  
 Zancleano p.p.- Santemiano

**26** **MEMBRO DI BORELLO**  
 Prevalenti areniti giallo ocracee, poco cementate, a granulometria da grossolana a medio-fine con subordinati livelli pelitici. Gli strati sono medi e sottili con abbondanti bioclasti.  
 Pliocene inferiore-medio

**27** **tv - ORIZZONTE DEL TRAVE**  
 Calcareniti ed arenarie più o meno cementate  
 Messiniano sup. p.p. - Pliocene inf. p.p.(?)

**28** **ARENARIE DI M. TURRINO**  
 Porzioni in prevalenza arenacee ed altre arenaceo-pelitiche  
 Messiniano p.p.

**29** **FORMAZIONE A COLOMBACCI**  
 Argille e argille marnoso-siltose grigie e grigio-scure con intercalati sottili strati calcarei biancastri (colombacci) e arenitici.  
 Messiniano p.p.

**30** **FORMAZIONE DELLA LAGA**  
**MEMBRO POST EVAPORITICO**  
 Associazione torbiditica prevalentemente pelitica, con intercalati numerosi orizzonti delle associazioni pelitico-arenacea, arenaceo-pelitica, e arenacea, corrispondenti a litofacies.  
 Messiniano p.p.

**48** **SCHLIER**  
 Marne, marne argillose e marne calcaree grigiastre.  
 Burdigaliano-Messiniano

**49** **MARNE CON CERROGNA**  
 Marne, marne calcaree con intercalazioni di torbiditi carbonatiche, in strati da sottili a spessi, con frequenti fenomeni di slumping.  
 Burdigaliano-Tortoniano

**50** **BISCIARO**  
 Calcari e calcari marnosi con liste e noduli di selce nerastra nella parte inferiore, a cui si intercalano marne grigie e grigio verdastre; marne e marne a rgillose grigie. Potenza da 20m a circa 100m.  
 Aquitaniano p.p.-Burdigaliano p.p.

**51** **SCAGLIA CINEREA**  
 Marne calcaree, marne e marne argillose grigio-verdastre, con subordinati calcari marnosi grigiastri. Potenza massima 200m.  
 Bartoniano p.p. - Aquitaniano p.p.

**52** **SCAGLIA ROSSA, SCAGLIA BIANCA, SCAGLIA VARIEGATA**  
 Calcari e calcari marnosi, spesso con selce rossa o nerastra. Per una migliore lettura della cartografia si è ritenuto opportuno accorpere le tre formazioni.  
 Albiano sup. p.p.-Priabroniano p.p.

**53** **MARNE A FUCOIDI**  
 Marne e marne argillose e calcari marnosi con livelli bituminosi. La porzione superiore è caratterizzata da alternanze di calcari marnosi e marne calcaree biancastre. Quella inferiore è data da marne e marne argillose policrome con frequenti livelli di black shales, di cui quello basale.  
 Aptiano inf. p.p.-Albiano sup. p.p.

**54** **MAIOLICA**  
 Calcari micritici bianchi, a frattura concoide, con liste e noduli di selce grigia e nerastra; sottili livelli bituminosi più frequenti verso l'alto. Potenza 120m.  
 Tortoniano sup.-Aptiano inf. p.p.

**55** **CALCARI DIASPRINI UMBRO MARCHIGIANI**  
 Calcari selciferi, calcari micritici e diasprini in associazione variabile, a luoghi calcari detritici.  
 Bajociano sup.-Tortoniano inf.

**56** **CALCARI DETRITICI DEL MONTE VALVASSETO**  
 Calcari grigio-biancastri in strati di spessore variabile, con subordinati livelli marnosi.  
 Toarciano sup.-Caltoviano inf.

**57** **CALCARI E MARNE A POSIDONIA; ROSSO AMMONITICO (FORMAZIONE DEL BOSSO)**  
 Calcari marnosi ricchi in fossili. Per una migliore lettura della carta si è ritenuto opportuno accorpere le due formazioni.  
 Toarciano sup. p.p.-Bajociano inf.

**58** **ROSSO AMMONITICO**  
 Calcari marnosi, marne calcaree e marne argillose rosso vinaccia e verdastre, nodulari, in strati da sottili e medi. L'associazione paleontologica è caratterizzata da abbondanti ammoniti da lageridi, gasteropodi, radiolari e resti filamentosi. (riportato solo nella zona del Furlo)  
 Toarciano p.p.


**59** **MARNE DI MONTE SERRONE**  
 Alternanze di calcareniti, marne e calcari marnosi grigio-verdastri; nella porzione superiore prevalgono i litotipi detritici.  
 Pliensbachiano sup.-Toarciano p.p.

**60** **CORNIOLA**  
 Calcari micritici marnosi di colore grigio nocciola con liste e noduli di selce con sottili livelli marnoso-argillosi.  
 Sinemuriano inf. p.p.-Toarciano inf. p.p.

**61** **CALCARE MASSICCIO; GRUPPO DEL BUGARONE**  
 Calcari, calcari marnosi nodulari in strati da medi a massicci. Per una migliore lettura della cartografia si è ritenuto opportuno accorpere gli affioramenti del Bugarone al Calcare Massiccio ad esso confinante.  
 Hettangiano-Bajociano

**62** **CALCARE MASSICCIO**  
 Calcari biancastri in strati massicci, con intercalazioni di calcari micritici nocciola in strati medi-sottili.  
 Hettangiano-Carixiano p.p.

ELEMENTI TETTONICI

 Sovracorrimento

 Faglia diretta

 Faglia

 Faglia incerta